

THE SURFACE CHEMISTRY OF RUTILE  
IN TECHNOLOGICALLY RELEVANT ENVIRONMENTS

A Dissertation

Presented to the Faculty of the Graduate School

of Cornell University

In Partial Fulfillment of the Requirements for the Degree of

Doctor of Philosophy

By

Anqi Song

June 2016

© 2016 Anqi Song

THE SURFACE CHEMISTRY OF RUTILE  
IN TECHNOLOGICALLY RELEVANT ENVIRONMENTS

Anqi Song, PhD

Cornell University 2016

The surface science of titanium dioxide,  $\text{TiO}_2$ , has attracted great amount of attention due to its high profile applications. This dissertation shows the development of well-controlled rutile (110) surfaces that provide a platform for studying the chemical and photochemical reactivity of rutile in technologically relevant environments, including air and solutions.

Near-perfect rutile (110) surfaces characterized by atomically flat terraces and straight steps were produced using basic peroxide solutions. The reaction produced straight steps with a different orientation, different structure, and different reactivity from those prepared in ultrahigh vacuum. The morphology was explained by a site-specific model of rutile (110) etching based on metal oxo coordination chemistry. This work shows that one of the important roles of peroxo ligands in etching and growth reactions is to destabilize neighboring bonds and increase their lability. The peroxo ligands add a degree of reversibility to the growth reaction, leading to the formation of well-ordered crystals. In addition, this near-perfect rutile (110) surface is an ideal starting point for studying surface chemistry of rutile in technologically relevant environments.

Under ambient conditions atmospheric  $\text{CO}_2$  reacted with adsorbed  $\text{H}_2\text{O}$  and produced a self-assembled monolayer of  $\text{HCO}_3^-$  on rutile (110) surfaces. The monolayer was formed on the near-perfect rutile surfaces prepared by basic peroxide etching, indicating that surface defects, such as

Ti interstitials and O vacancies, were not required. DFT calculations suggested that the nanoscale water film adsorbed on the surface solvated the adsorbates and changed the reaction energetics. The  $\text{HCO}_3^-$  monolayer was very stable, even in vacuum, which was a result of the strong bidentate bonding of  $\text{HCO}_3^-$ . The formation of the strongly bound bicarbonate monolayer suggests that  $\text{HCO}_3^-$ , instead of  $\text{CO}_2$ , plays a key role in the photoreduction of  $\text{CO}_2$ .

A high-quality, self-assembled benzoate monolayer was prepared on the near-perfect rutile (110) surfaces using simple solution chemistry. The monolayer remained free of contamination in air for tens of minutes. Surface science techniques combined with computations revealed that the phenyl rings adopted an edge-to-face tetrameric geometry with their four nearest neighbors. Adjacent molecules tilted towards each other across Ti atom rows, leading to the formation of a paired structure as observed in scanning tunneling microscopy images. The stability of the monolayer is a result of the strong bidentate bonding to unsaturated Ti atoms and the  $\pi$ - $\pi$  interactions between the benzoate molecules.

## BIOGRAPHICAL SKETCH

Anqi Song was born on April 30, 1989 in Tai'an, China. She attended Tai'an Diyi Shiyan Primary School, Wangyue Middle School, and Taishan Middle School. When she grew up, she saw the pollution of a river in her hometown by chemicals from nearby industries. She then decided to study science, hoping that she could help solve environmental and energy problems in the future. She obtained her Bachelor's degree in Chemistry from Beijing Normal University. She studied petrol oil using AFM in her undergraduate research and started to be interested in surface science. She decided to attend Cornell University in 2011. She joined Professor Melissa A. Hines' group and studied the surface science of  $\text{TiO}_2$  in her graduate research. She passed her B exam in June 2016.

## ACKNOWLEDGEMENTS

First and foremost, I would like to express my sincere gratitude to my advisor Professor Melissa A. Hines for her continuous support of my PhD study and research. I not only learned a great amount of knowledge from her, but also was encouraged by her enthusiasm towards science. When she guided my research, she showed me the importance of independent thinking and problem-solving skills. She read and revised every sentence in this dissertation for many times. Without her guidance, I cannot complete my graduate research and this dissertation. In addition, I obtained a lot of training on presentation skills from her.

Besides Professor Hines, I would also like to thank Professor Roger F. Loring and Professor Jiwoong Park for being my thesis committee members.

My labmates, Dapeng, Erik, Will, Amnon, and Josh, have helped me a lot in the past five years. I enjoyed discussing about research and solving technological problems together with my labmates. I would particularly thank them for their great patience and support when I could not express my ideas clearly in English.

I am deeply thankful to my family and friends who always support me throughout the five years. I dedicate this dissertation to my beloved grandfather who passed away before my B exam.

Last but not least, I would like to thank the people in Chemistry Department who helped me in my courses, teaching, and life.

## TABLE OF CONTENTS

Biographical sketch.....	iii
Acknowledgements.....	iv
Table of contents.....	v
List of figures.....	ix
Chapter 1 Introduction.....	1
1.1 Applications of TiO <sub>2</sub> .....	1
1.2 Recent progress in the surface science of rutile (110).....	3
1.3 Achievements and overview of the dissertation.....	7
References.....	9
Chapter 2 Experimental.....	15
2.1 Scanning Tunneling Microscope.....	15
2.1.1 The Working Principle of the Scanning Tunneling Microscope.....	15
2.1.2 The Ultrahigh Vacuum System.....	15
2.1.3 Components of the System.....	16
2.2 Sputter Ion Gun.....	17
2.2.1 Sputter Gun Alignment and Calibration.....	17
2.2.2 Preparation of Sputtered and Annealed Rutile (110) Samples.....	18
2.3 Tip Preparation.....	19
2.3.1 Recrystallization of Tungsten Wire.....	20
2.3.2 Electrochemical Etching of Tungsten Wire.....	21
2.3.3 Electron-beam Heater for Tip Cleaning.....	22
2.3.4 Field-directed Sputter Sharpening of the Tip.....	22

2.4 X-ray Photoelectron Spectroscopy .....	23
2.4.1 The Principle of X-ray Photoelectron Spectroscopy .....	23
2.4.2 X-ray Source .....	24
2.4.3 XPS Analyzer.....	24
2.5 Sample Preparation .....	25
References .....	26
Chapter 3 Preparation of atomically flat rutile (110) using aqueous peroxide solutions and the structure-directing role of peroxide in TiO <sub>2</sub> polymorph control.....	
29	29
3.1 Introduction.....	29
3.2 Experimental .....	33
3.3 Results.....	34
3.3.1 Preparation of near-perfect surface .....	34
3.3.2 XPS analysis of chemical composition.....	35
3.3.3 Pits shape evolution reveal reactivity .....	38
3.3.4 Identification of active species.....	41
3.3.5 Kinetic Monte Carlo simulations .....	42
3.4 Discussion.....	47
3.4.1 Site-specific reactivity .....	47
3.4.2 The role of peroxo ligands .....	48
3.5 Conclusions.....	50
References.....	51
Chapter 4 Nanoscale solvation leads to spontaneous formation of a bicarbonate monolayer on rutile (110) under ambient conditions: implications for CO <sub>2</sub> photoreduction .....	
56	56

4.1	Abstract .....	56
4.2	Introduction .....	57
4.3	Experimental and Computational .....	60
4.3.1	Experimental Methods .....	60
4.3.2	Computational Methods .....	61
4.4	Results .....	61
4.5	Discussion .....	72
4.6	Conclusions .....	75
	References .....	75
Chapter 5	Solution-based preparation of benzoate monolayers on rutile (110) .....	82
5.1	Introduction .....	88
5.2	Experimental and Computational .....	84
5.2.1	Experimental methods .....	84
5.2.2	Quantification of monolayer coverage from XPS spectra .....	85
5.2.3	Computational methods .....	86
5.3	Results .....	88
5.3.1	STM .....	88
5.3.2	Infrared spectroscopy .....	91
5.3.3	XPS analysis .....	93
5.3.4	Monte Carlo Simulations .....	96
5.3.5	DFT calculations .....	100
5.4	Discussion .....	102
5.5	Conclusions .....	104

References..... 104

## LIST OF FIGURES

Figure 1.1 STM image of sputtered and annealed rutile (110) surface. ....	4
Figure 1.2 Molecular model of rutile (110) surface in UHV.....	4
Figure 2.1 Schematic of the single-tube scanner .....	17
Figure 2.2 STM image of a rutile (110) surface prepared by sputtering and annealing .....	19
Figure 2.3 Recrystallization apparatus.....	20
Figure 2.4 Schematic of energy diagram in XPS.....	24
Figure 3.1 (a) Molecular model of UHV-prepared rutile (110) surface. (b) STM image of UHV-prepared surface. (c) Molecular model of rutile (110) surface in aqueous solutions.....	31
Figure 3.2 STM image of a rutile (110) surface after immersion in a basic peroxide solution ....	35
Figure 3.3 XPS spectra of rutile (110) surface after reaction in basic peroxide solution as function of annealing temperature .....	38
Figure 3.4 Pits evolution on a rutile (110) surface etched by basic peroxide solution .....	40
Figure 3.5 STM images of a rutile (110) surface etched by a basic peroxide solution for 2 min.	41
Figure 3.6 Molecular model of rutile (110) surfaces with the possible structure of kink sites and step sites and the hypothesized bidentate bonding of peroxo ligands. ....	43
Figure 3.7 KMC simulations illustrating the kink site reactivity.....	44
Figure 3.8 KMC simulations illustrating the fast kink etching and slow kink etching regimes...	46
Figure 3.9 KMC simulations testing the relative reactivity of symmetric and asymmetric step sites .....	46
Figure 4.1 STM image and molecular model of aqueous etched rutile (110) surfaces.....	62
Figure 4.2 <i>S</i> - and <i>p</i> -polarized infrared spectra of aqueous etched rutile (110) surfaces.....	63

Figure 4.3 STM images of a sputtered and annealed rutile (110) sample that was then exposed to air. ....	66
Figure 4.4 STM images of a sputtered and annealed rutile (110) sample that was then immersed in H <sub>2</sub> O for 3 min.....	67
Figure 4.5 STM images of an aqueous etched rutile (110) sample that was then heated to 513 K .....	68
Figure 4.6 XPS spectra obtained from a chemically etched rutile (110) sample as a function of temperature. ....	69
Figure 4.7 Structure of adsorbed HCO <sub>3</sub> and H determined from DFT calculations .....	71
Figure 5.1 STM image of benzoate monolayer on the rutile (110) surface prepared from benzoic acid solution.....	88
Figure 5.2 High-resolution STM images of benzoate monolayers on rutile (110) surface .....	90
Figure 5.3 Experimental and calculated infrared spectra of benzoate monolayer taken with different light propagation directions and polarizations .....	93
Figure 5.4 High-resolution XPS of benzoate monolayers on rutile (110) as a function of annealing temperature.....	95
Figure 5.5 Intermolecular potential of benzene dimers as a function of center-to-center distances and the schematic illustration of four benzoate molecules in a tetramer configuration .....	98
Figure 5.6 Simulated benzoate monolayers from Monte Carlo simulations .....	99
Figure 5.7 Energies of different configurations obtained from DFT calculations as a function of tilting angle .....	100
Figure 5.8 Model of the most stable configuration of benzoate monolayer on rutile (110) surface from DFT calculations .....	101

## Chapter 1

### Introduction

The aim of this dissertation is to understand the chemical and photochemical reactivity of rutile  $\text{TiO}_2$  in technologically relevant environments using surface science techniques combined with computational methods.

#### 1.1 Applications of $\text{TiO}_2$

Titanium dioxide,  $\text{TiO}_2$ , is a photocatalyst that has attracted great amount of attention due to its potential applications. Because of its high refractive index,  $\text{TiO}_2$  has been traditionally used as a white pigment. In 1972 Fujishima and Honda<sup>1</sup> discovered the photolysis of water into  $\text{H}_2$  and  $\text{O}_2$  at  $\text{TiO}_2$  electrodes without external voltage. Inspired by their work, scientists have developed many new applications of  $\text{TiO}_2$ , such as dye-sensitized solar cells (DSSC),<sup>2</sup> wastewater purification methods, self-cleaning glass,<sup>3-4</sup> and antibacterial coatings.<sup>5</sup> When  $\text{TiO}_2$  is illuminated with above-bandgap radiation (387 nm for anatase  $\text{TiO}_2$  and 413 nm for rutile  $\text{TiO}_2$ ), electrons are excited from the valence band to the conduction band. The photoexcited electrons and holes can migrate to the  $\text{TiO}_2$  surface and participate in reduction and oxidation reactions, respectively. The holes have an oxidation potential of +2.53 V, even higher than  $\cdot\text{OH}$ ,  $\text{O}_3$ ,  $\text{H}_2\text{O}_2$ , and  $\text{O}_2$ .<sup>6</sup> The potential for the electrons is -0.52 V, which is sufficient to reduce water to  $\text{H}_2$ . Not all of the photo-induced charge participates in the redox reactions; most of the electrons and holes will recombine. Therefore, improving the light absorption region and suppressing carrier recombination may help increase the efficiency of  $\text{TiO}_2$  photoreactions.

Dye-sensitized solar cells improve the solar absorption of bare  $\text{TiO}_2$ . When the dye absorbs light, electrons in the highest occupied molecular orbital of the dye are excited into the lowest unoccupied molecular orbital.<sup>2</sup> The dyes are usually complex compounds that can harvest light

from UV to visible/IR region.<sup>2, 7-8</sup> The excited electrons are then injected into the conduction band of the TiO<sub>2</sub>, and the photogenerated holes oxidize the redox mediators (e.g., I<sup>-</sup> / I<sub>3</sub><sup>-</sup>). The electrons are then conducted through the nanocrystalline TiO<sub>2</sub> layer to an external circuit to the counter electrode where they reduce the redox mediators (I<sup>-</sup> / I<sub>3</sub><sup>-</sup>). In DSSCs, the details of the charge transfer process from the dye to the TiO<sub>2</sub> are not well understood. The thermal and photochemical stability of dye molecules is important to the long-term stability of DSSCs;<sup>9-11</sup> therefore, understanding the degradation mechanism of dye molecules on TiO<sub>2</sub> is also essential.

Another important application of TiO<sub>2</sub> is the photocatalytic degradation of organic molecules, which is harnessed in self-cleaning glass. Upon UV irradiation, electron-hole pairs are photogenerated in TiO<sub>2</sub> and diffuse to the surface. In a poorly understood process the photoexcited charge oxidizes almost all organic molecules.<sup>12</sup> For example, alcohols are oxidized to the corresponding aldehydes or ketones.<sup>13-15</sup> Dyes, such as methylene blue, are decomposed into CO<sub>2</sub>, NH<sub>4</sub><sup>+</sup>, NO<sub>3</sub><sup>-</sup>, and SO<sub>4</sub><sup>2-</sup>.<sup>16</sup> For this reason, the bleaching of methylene blue is often used to test the efficiency of TiO<sub>2</sub> nanocatalysts. Carboxylic acids are sequentially decomposed into CO<sub>2</sub> and other products.<sup>17-18</sup> One of the long-term goals of this research is to understand the atomic-scale reaction mechanisms and reactive sites on TiO<sub>2</sub> surfaces with the aim of designing new photocatalysts with improved efficiency.

The efficiency of these photocatalytic reactions on TiO<sub>2</sub> is thought to vary with the crystal phase, crystal facet, and surface site. There are three polymorphs of TiO<sub>2</sub> in nature: rutile, anatase, and brookite. Rutile is the thermodynamically stable and most abundant phase of TiO<sub>2</sub>, whereas anatase and brookite are metastable phases. Anatase is the main product of sol-gel syntheses of TiO<sub>2</sub>. Brookite is more difficult to grow and thus less investigated. Anatase was considered to be more reactive than rutile in early studies, such as in the oxidation of 2-

propanol.<sup>19</sup> Later studies claimed that, in some cases, rutile was more reactive than anatase.<sup>20-21</sup> The difference in rutile and anatase reactivity is hypothesized to be a result of both the band structure and the exposed surface structure. Even for the same crystalline phase, different facets of the crystal demonstrate different photocatalytic reactivity.<sup>22-24</sup> For example, researchers<sup>25</sup> suggested that anatase {101} facets were more reactive than {001} facets in the H<sub>2</sub> evolution reaction, presumably due to the difference in surface atomic configuration and coordination.<sup>21</sup> Even on the same facet, some sites may be more reactive than others. Surface scientists have shown that O vacancy sites in ultrahigh vacuum (UHV) are highly reactive for the splitting of water molecules on rutile (110) surfaces,<sup>26-27</sup> whereas flat, defect-free surfaces are thought to be unreactive. Given the important applications of TiO<sub>2</sub> and the factors influencing its reactivity, the goal of this research is to understand the surface structure and chemistry of TiO<sub>2</sub> at the atomic scale.

## **1.2 Recent progress in the surface science of rutile (110)**

Over the past two decades, surface scientists have made great progress in understanding the surface properties of TiO<sub>2</sub> in vacuum. Rutile (110) surfaces in UHV have been investigated extensively. In contrast, this dissertation will discuss the surprising structure and reactivity of rutile (110) surface in technologically relevant environments, such as air and water.

Rutile crystals are tetragonal. The Ti atoms in rutile crystals are six-fold coordinated, with four shorter equatorial bonds and two slightly longer axial bonds. The O atoms are three-fold coordinated. Prior to our research, flat and clean rutile (110) surfaces were prepared by sputtering and annealing in UHV. (For details, see Chapter 2.) A scanning tunneling microscope (STM) image of a sputtered and annealed rutile (110) surface is shown in Fig. 1.1. The molecular model of the rutile (110) surface is shown in Fig. 1.2. As can be seen from the STM image, the

surface is terminated by alternating bright and dark rows parallel to the [001] direction. The bright rows consist of rows of five-fold-coordinated Ti atoms, which will be referred to as  $Ti_{5c}$ . Each  $Ti_{5c}$  atom has one “dangling bond” perpendicular to the surface that can bind with other molecules, such as  $H_2O$ . The dark rows are composed of two-fold coordinated O atoms, usually called bridging O atoms. Each bridging O atom has one “dangling bond” that can bind, for example, to H.

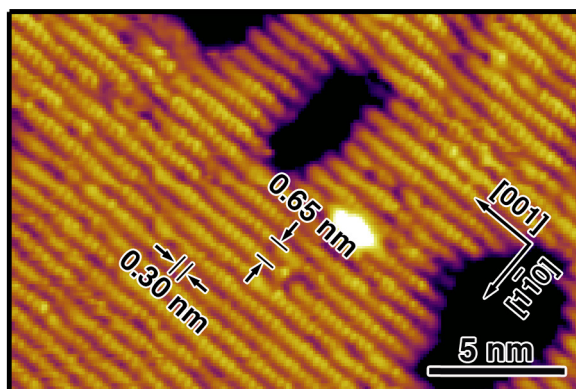


Figure 1.1 STM image of sputtered and annealed rutile (110) surface.

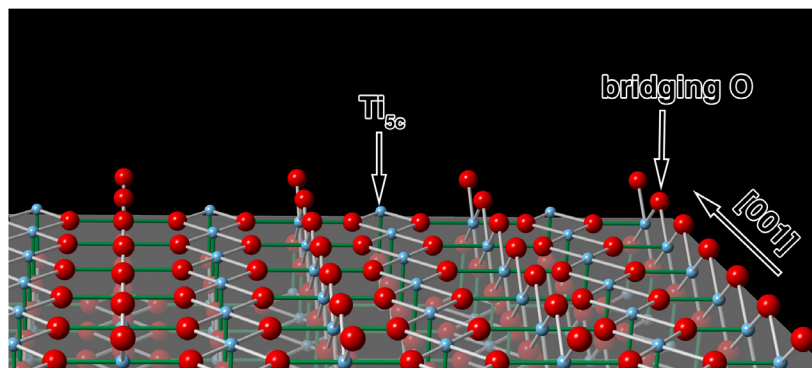


Figure 1.2 Molecular model of rutile (110) surface in UHV with Ti atoms in blue and O atoms in red. The green Ti-O bonds are slightly (~2%) longer than the grey ones.

After annealing at elevated temperatures, the clean rutile (110) surface forms three preferential steps aligned parallel to [001],  $[1\bar{1}1]$  and  $[1\bar{1}\bar{1}]$  orientations.<sup>28</sup> These

thermodynamically preferred steps have the lowest free energy. This dissertation will show that a completely different step structure is formed during aqueous etching reactions, emphasizing the importance of studying  $\text{TiO}_2$  surface chemistry in technologically relevant environments.

The sputtering and annealing cycles used to prepared clean surfaces in UHV generate defects in the bulk and on the surface of rutile. The most common and well-studied defects are  $\text{Ti}^{3+}$  ions and O vacancies. The  $\text{Ti}^{3+}$  species are detected using x-ray photoelectron spectroscopy (XPS) by their characteristic electron binding energy of 457.5 eV. Another important type of defect is the O vacancy, especially vacancies on bridging O rows. These defects appear as bright protrusions on dark rows in STM images.<sup>29</sup> Many reactions are O-vacancy-assisted in UHV, such as the dissociation of water molecules. The O vacancies are highly reactive in UHV; however, these vacancies are too reactive to survive in technologically relevant environments, such as in solutions and air, necessitating research in those environments. This dissertation demonstrates the preparation of near-perfect rutile (110) surfaces in solution.

The adsorption, desorption, and dissociation of many molecules, such as  $\text{N}_2$ ,  $\text{O}_2$ ,  $\text{CO}_2$ ,  $\text{H}_2\text{O}$ , acetic acid, trimethylacetic acid, and benzoic acid on rutile (110) surfaces in vacuum, have been studied by many scientists. Experimental and theoretical studies<sup>30-31</sup> have shown that UHV-dosed  $\text{N}_2$  molecules physisorb to  $\text{Ti}_{5c}$  sites at cryogenic temperatures. This reaction is irrelevant under most conditions as the  $\text{N}_2$  molecules fully desorb from the surface when the temperature is above 100 K.

Molecular oxygen is one of the most important oxidizing agents in the environment where  $\text{TiO}_2$  is used. In UHV, molecular  $\text{O}_2$  adsorbs on rutile (110) surfaces both physically and dissociatively.<sup>32-33</sup> When heated above 350 K, Ti interstitials start to diffuse to the surface and react with O adatoms produced by  $\text{O}_2$  dissociation, forming small  $\text{TiO}_x$  islands on terraces.<sup>32</sup> The

non-dissociated O<sub>2</sub> molecules desorb above 410 K.

The adsorption of CO<sub>2</sub> on rutile (110) has been studied in UHV. Temperature programmed desorption (TPD) and STM experiments show that CO<sub>2</sub> molecules bind to two different sites at cryogenic temperatures: O vacancies and Ti<sub>5c</sub> sites.<sup>34</sup> The CO<sub>2</sub> molecules are more strongly bound to O vacancy sites, desorbing above 166 K, and less strongly bound to Ti<sub>5c</sub> sites, desorbing above 137 K. Thus CO<sub>2</sub> molecules do not stably adsorb to rutile (110) surfaces at room temperature.

The adsorption and dissociation of H<sub>2</sub>O on rutile surfaces have been extensively investigated due to the importance of water splitting under UV irradiation. Physisorbed H<sub>2</sub>O molecules on Ti<sub>5c</sub> sites and bridging O sites desorb at ~265 K and ~175 K, respectively.<sup>35-36</sup> Besides the physical adsorption, H<sub>2</sub>O molecules dissociate at O vacancy sites, forming OH groups that “heal” the O vacancies, with the remaining H atoms binding to nearby bridging O atoms. Both bridging OH groups and bridging O vacancies appear as bright features on dark rows in STM.<sup>27</sup> The bridging OH groups can diffuse along and across atom rows.<sup>37-38</sup>

The adsorption of carboxylic acids has also been investigated. STM images were obtained on surfaces dosed with different carboxylic acids.<sup>39-41</sup> These carboxylic acids adsorb dissociatively through acid hydrogen cleavage.<sup>36</sup> The resulting carboxylates are chemically bound to two Ti<sub>5c</sub> sites through bidentate Ti<sub>5c</sub>-O bonds, leading to the formation of monolayers. Well-ordered bright protrusions with a characteristic spacing twice that of the Ti atoms appear along the [001] direction, consistent with the expected bidentate bonding. In contrast to other carboxylic acids, benzoate molecules sometimes appear to pair. This phenomenon was previously described as dimerization; however, we show the strong  $\pi$ - $\pi$  interactions lead to a more complicated geometry.

Only two carboxylic acids have been shown to be photoreactive in UHV environment: acetic

acid and trimethylacetic acid. Research on trimethylacetic acid adsorption<sup>42</sup> showed that UV irradiation in the presence of oxygen led to a decrease of the C 1s peak in XPS. Henderson and co-workers<sup>43-44</sup> suggested that photo-induced holes promoted the formation of *tert*-butyl radicals ((CH<sub>3</sub>)<sub>3</sub>C•) from trimethyl acetate ((CH<sub>3</sub>)<sub>3</sub>CCOO<sup>-</sup>) through C-C bond cleavage. Isobutene and isobutane were the final products of the reaction. They hypothesized that O<sub>2</sub> accelerated the reaction by depleting excess surface Ti<sup>3+</sup> ions that came from the reduction of Ti<sup>4+</sup> by photo-induced electrons. The photostability of benzoic acid on rutile was also investigated by Friend's group.<sup>45</sup> According to them, benzoic acid was not degraded when exposed to O<sub>2</sub> under UV illumination. In contrast, the photodegradation of benzoic acid on rutile surface in the presence of 1 atm O<sub>2</sub> has been observed by XPS, STM, and infrared spectra in this research. Studies of this photocatalytic reaction are ongoing and will not be discussed in this dissertation.

### **1.3 Achievements and overview of the dissertation**

This dissertation aims at understanding and controlling the surface chemical and photochemical reactivity of rutile in technologically relevant environments using STM and other surface science techniques. This dissertation will primarily discuss the solution-based preparation of nearly perfect rutile (110) surface, the formation of self-assembled bicarbonate monolayers under ambient conditions, and the solution-based preparation of self-assembled benzoate monolayers. The implications of these findings will also be discussed.

Near-perfect rutile (110) surfaces characterized by atomically flat terraces and straight steps were produced using simple basic peroxide solutions.<sup>46</sup> The reaction produced straight steps with a different orientation, different structure, and different reactivity from those produced in UHV. The morphological evolution during etching revealed the site-specific reactivity of surface sites. This study demonstrated that the role of peroxo ligands in etching and growth is to destabilize

neighboring bonds and increase their lability. Importantly, this explains the structure-directing role of peroxy ligands in crystal synthesis: the ligands add a degree of reversibility to the growth reaction, leading to the formation of well-ordered crystals. In addition, this near-perfect rutile (110) surface is an ideal starting point for the study of the chemistry of rutile in technologically relevant environments.

Under ambient conditions atmospheric  $\text{CO}_2$  reacted with adsorbed  $\text{H}_2\text{O}$  and produced a self-assembled monolayer of  $\text{HCO}_3^-$  and  $\text{H}^+$  on rutile (110) surfaces.<sup>47</sup> The monolayer was formed on the near-perfect rutile surfaces prepared by basic peroxide etching, indicating that surface defects, such as Ti interstitials and O vacancies, were not required in producing the monolayer. DFT calculations suggested that the nanoscale water film adsorbed on the surface solvates the adsorbates and changes the reaction energetics. The monolayer was very stable, even in vacuum, which was a result of the strong bidentate bonding of  $\text{HCO}_3^-$ . The formation of near-ideal bicarbonate monolayer has important implications for understanding the photocatalytic reduction of  $\text{CO}_2$ , which is a potential way to design a sustainable cycle of consuming/recycling carbon-based fuels.<sup>48</sup> Previous researchers proposed that  $\text{CO}_2$  adsorbed on  $\text{TiO}_2$  surface was first reduced by the photogenerated electrons and transformed into a bent form of  $\text{CO}_2^-$ . This dissertation shows that  $\text{CO}_2$  is unlikely to play a key role in the  $\text{CO}_2$  photoreduction reaction since the surface is covered by a monolayer of strongly bound  $\text{HCO}_3^-$  molecules.

A self-assembled benzoate monolayer was prepared on near-perfect rutile (110) surfaces using simple solution chemistry.<sup>49</sup> Benzoic acid is a small-molecule analogue of dyes used in DCCSs. Benzoic acid molecules adsorb on the surface dissociatively, producing a half monolayer of protons and a monolayer of bidentate benzoates strongly bound to the  $\text{Ti}_{5c}$  sites. Surfaces terminated with a benzoate monolayer remained free of contamination in air for tens of

minutes. Surface science techniques combined with computations revealed that the phenyl rings adopted an edge-to-face tetrameric geometry with their four nearest neighbors, as a result of the  $\pi$ - $\pi$  intermolecular interactions mainly composed of quadrupole-quadrupole interactions and dispersion forces. Adjacent molecules tilted towards each other across Ti atom rows, leading to the appearance of a paired structure in STM images. The energy gained from tilting further stabilized the monolayer. This research showed that a simple model containing the surface geometry and intermolecular interactions of a small-molecule analogue of the monolayer head groups could predict the surface configuration, providing a potential way to understand and design new monolayers.

### References

1. A. Fujishima, "Electrochemical Photolysis of Water at a Semiconductor Electrode," *Nature* **238**, 37 (1972).
2. B. O'Regan and M. Grätzel, "A Low-Cost, High-Efficiency Solar Cell Based on Dye-Sensitized Colloidal TiO<sub>2</sub> Films," *Nature* **353**, 737 (1991).
3. Y. Paz, Z. Luo, L. Rabenberg, and A. Heller, "Photooxidative Self-Cleaning Transparent Titanium Dioxide Films on Glass," *J. Mater. Res.* **10**, 2842 (1995).
4. V. Romeas, P. Pichat, C. Guillard, T. Chopin, and C. Lehaut, "Testing the Efficacy and the Potential Effect on Indoor Air Quality of a Transparent Self-Cleaning TiO<sub>2</sub>-Coated Glass through the Degradation of a Fluoranthene Layer," *Ind. Eng. Chem. Res.* **38**, 3878 (1999).
5. K. Sunada, Y. Kikuchi, K. Hashimoto, and A. Fujishima, "Bactericidal and Detoxification Effects of TiO<sub>2</sub> Thin Film Photocatalysts," *Environ. Sci. Technol.* **32**, 726 (1998).
6. A. Fujishima, T. N. Rao, and D. A. Tryk, "Titanium Dioxide Photocatalysis," *J. Photochem. Photobiol. C: Photochem. Rev.* **1**, 1 (2000).

7. V. Sugathan, E. John, and K. Sudhakar, "Recent Improvements in Dye Sensitized Solar Cells: A Review," *Renew. Sust. Energ. Rev.* **52**, 54 (2015).
8. B. E. Hardin, H. J. Snaith, and M. D. McGehee, "The Renaissance of Dye-Sensitized Solar Cells," *Nature Photonics* **6**, 162 (2012).
9. H. G. Agrell, J. Lindgren, and A. Hagfeldt, "Degradation Mechanisms in a Dye-Sensitized Solar Cell Studied by UV-Vis and IR Spectroscopy," *Solar Energy* **75**, 169 (2003).
10. F. Nour-Mohhamadi, S. D. Nguyen, G. Boschloo, A. Hagfeldt, and T. Lund, "Determination of the Light-Induced Degradation Rate of the Solar Cell Sensitizer N719 on TiO<sub>2</sub> Nanocrystalline Particles," *J. Phys. Chem. B* **109**, 22413 (2005).
11. A. Quan "Degradation of the Solar Cell Dye Sensitizer N719 Preliminary Building of Dye-Sensitized Solar Cell," Master Thesis, Roskilde University (2006).
12. J. Schneider, M. Matsuoka, M. Takeuchi, J. Zhang, Y. Horiuchi, M. Anpo, and D. W. Bahnemann, "Understanding TiO<sub>2</sub> Photocatalysis: Mechanisms and Materials," *Chem. Rev.* **114**, 9919 (2014).
13. K. Ikeda, H. Sakai, R. Baba, K. Hashimoto, and A. Fujishima, "Photocatalytic Reactions Involving Radical Chain Reactions Using Microelectrodes," *J. Phys. Chem. B* **101**, 2617 (1997).
14. X. Lang, W. Ma, C. Chen, H. Ji, and J. Zhao, "Selective Aerobic Oxidation Mediated by TiO<sub>2</sub> Photocatalysis," *Acc. Chem. Res.* **47**, 355 (2013).
15. J. Muir, Y. Choi, and H. Idriss, "Computational Study of Ethanol Adsorption and Reaction over Rutile TiO<sub>2</sub> (110) Surfaces," *Phys. Chem. Chem. Phys.* **14**, 11910 (2012).
16. A. Houas, H. Lachheb, M. Ksibi, E. Elaloui, C. Guillard, and J.-M. Herrmann, "Photocatalytic Degradation Pathway of Methylene Blue in Water," *Appl. Catal., B* **31**, 145 (2001).

17. S. Horikoshi, F. Hojo, H. Hidaka, and N. Serpone, "Environmental Remediation by an Integrated Microwave/UV Illumination Technique. 8. Fate of Carboxylic Acids, Aldehydes, Alkoxy carbonyl and Phenolic Substrates in a Microwave Radiation Field in the Presence of TiO<sub>2</sub> Particles under UV Irradiation," *Environ. Sci. Technol.* **38**, 2198 (2004).
18. B. Wen, Y. Li, C. Chen, W. Ma, and J. Zhao, "An Unexplored O<sub>2</sub>-Involved Pathway for the Decarboxylation of Saturated Carboxylic Acids by TiO<sub>2</sub> Photocatalysis: An Isotopic Probe Study," *Chem. Eur. J.* **16**, 11859 (2010).
19. T. Ohno, K. Sarukawa, and M. Matsumura, "Photocatalytic Activities of Pure Rutile Particles Isolated from TiO<sub>2</sub> Powder by Dissolving the Anatase Component in HF Solution," *J. Phys. Chem. B* **105**, 2417 (2001).
20. N. Masahashi, Y. Mizukoshi, S. Semboshi, and N. Ohtsu, "Enhanced Photocatalytic Activity of Rutile TiO<sub>2</sub> Prepared by Anodic Oxidation in a High Concentration Sulfuric Acid Electrolyte," *Appl. Catal., B* **90**, 255 (2009).
21. J. Yan, G. Wu, N. Guan, L. Li, Z. Li, and X. Cao, "Understanding the Effect of Surface/Bulk Defects on the Photocatalytic Activity of TiO<sub>2</sub>: Anatase Versus Rutile," *Phys. Chem. Chem. Phys.* **15**, 10978 (2013).
22. X. Han, Q. Kuang, M. Jin, Z. Xie, and L. Zheng, "Synthesis of Titania Nanosheets with a High Percentage of Exposed (001) Facets and Related Photocatalytic Properties," *J. Am. Chem. Soc.* **131**, 3152 (2009).
23. J. Pan, G. Liu, G. Q. M. Lu, and H. M. Cheng, "On the True Photoreactivity Order of {001}, {010}, and {101} Facets of Anatase TiO<sub>2</sub> Crystals," *Angew. Chem. Int. Ed.* **50**, 2133 (2011).

24. H. G. Yang, C. H. Sun, S. Z. Qiao, J. Zou, G. Liu, S. C. Smith, H. M. Cheng, and G. Q. Lu, "Anatase TiO<sub>2</sub> Single Crystals with a Large Percentage of Reactive Facets," *Nature* **453**, 638 (2008).
25. T. R. Gordon, M. Cargnello, T. Paik, F. Mangolini, R. T. Weber, P. Fornasiero, and C. B. Murray, "Nonaqueous Synthesis of TiO<sub>2</sub> Nanocrystals Using TiF<sub>4</sub> to Engineer Morphology, Oxygen Vacancy Concentration, and Photocatalytic Activity," *J. Am. Chem. Soc.* **134**, 6751 (2012).
26. O. Bikondoa, C. L. Pang, R. Ithnin, C. A. Muryn, H. Onishi, and G. Thornton, "Direct Visualization of Defect-Mediated Dissociation of Water on TiO<sub>2</sub> (110)," *Nat. Mater.* **5**, 189 (2006).
27. R. Schaub, P. Thostrup, N. Lopez, E. Lægsgaard, I. Stensgaard, J. K. Nørskov, and F. Besenbacher, "Oxygen Vacancies as Active Sites for Water Dissociation on Rutile TiO<sub>2</sub> (110)," *Phys. Rev. Lett.* **87**, 266104 (2001).
28. U. Diebold, "The Surface Science of Titanium Dioxide," *Surf. Sci. Rep.* **48**, 53 (2003).
29. U. Diebold, J. F. Anderson, K.-O. Ng, and D. Vanderbilt, "Evidence for the Tunneling Site on Transition-Metal Oxides: TiO<sub>2</sub> (110)," *Phys. Rev. Lett.* **77**, 1322 (1996).
30. F. Rittner, B. Boddenberg, M. Bojan, and W. Steele, "Adsorption of Nitrogen on Rutile (110): Monte Carlo Computer Simulations," *Langmuir* **15**, 1456 (1999).
31. Z. Dohnálek, J. Kim, O. Bondarchuk, J. M. White, and B. D. Kay, "Physisorption of N<sub>2</sub>, O<sub>2</sub>, and CO on Fully Oxidized TiO<sub>2</sub> (110)," *J. Phys. Chem. B* **110**, 6229 (2006).
32. M. A. Henderson and I. Lyubinetsky, "Molecular-Level Insights into Photocatalysis from Scanning Probe Microscopy Studies on TiO<sub>2</sub> (110)," *Chem. Rev.* **113**, 4428 (2013).

33. E. Lira, J. Ø. Hansen, P. Huo, R. Bechstein, P. Galliker, E. Lægsgaard, B. Hammer, S. Wendt, and F. Besenbacher, "Dissociative and Molecular Oxygen Chemisorption Channels on Reduced Rutile TiO<sub>2</sub> (110): An STM and TPD Study," *Surf. Sci.* **604**, 1945 (2010).
34. D. Acharya, N. Camillone III, and P. Sutter, "CO<sub>2</sub> Adsorption, Diffusion, and Electron-Induced Chemistry on Rutile TiO<sub>2</sub> (110): A Low-Temperature Scanning Tunneling Microscopy Study," *J. Phys. Chem. C* **115**, 12095 (2011).
35. M. A. Henderson, "Evidence for Bicarbonate Formation on Vacuum Annealed TiO<sub>2</sub> (110) Resulting from a Precursor-Mediated Interaction between CO<sub>2</sub> and H<sub>2</sub>O," *Surf. Sci.* **400**, 203 (1998).
36. C. L. Pang, R. Lindsay, and G. Thornton, "Chemical Reactions on Rutile TiO<sub>2</sub> (110)," *Chem. Soc. Rev.* **37**, 2328 (2008).
37. S. Wendt, J. Matthiesen, R. Schaub, E. K. Vestergaard, E. Lægsgaard, F. Besenbacher, and B. Hammer, "Formation and Splitting of Paired Hydroxyl Groups on Reduced TiO<sub>2</sub> (110)," *Phys. Rev. Lett.* **96**, 066107 (2006).
38. Z. Zhang, O. Bondarchuk, B. D. Kay, J. White, and Z. Dohnalek, "Imaging Water Dissociation on TiO<sub>2</sub> (110): Evidence for Inequivalent Geminate OH Groups," *J. Phys. Chem. B* **110**, 21840 (2006).
39. D. C. Grinter, T. Woolcot, C.-L. Pang, and G. Thornton, "Ordered Carboxylates on TiO<sub>2</sub> (110) Formed at Aqueous Interfaces," *J. Phys. Chem. Lett.* **5**, 4265 (2014).
40. I. Lyubinetsky, Z. Yu, and M. A. Henderson, "Direct Observation of Adsorption Evolution and Bonding Configuration of TMAA on TiO<sub>2</sub> (110)," *J. Phys. Chem. C* **111**, 4342 (2007).
41. Q. Guo, I. Cocks, and E. Williams, "The Orientation of Acetate on a TiO<sub>2</sub> (110) Surface," *J. Chem. Phys.* **106**, 2924 (1997).

42. H. Idriss, P. Legare, and G. Maire, "Dark and Photoreactions of Acetates on TiO<sub>2</sub> (110) Single Crystal Surface," *Surf. Sci.* **515**, 413 (2002).
43. J. M. White and M. A. Henderson, "Trimethyl Acetate on TiO<sub>2</sub> (110): Preparation and Anaerobic Photolysis," *J. Phys. Chem. B* **109**, 12417 (2005).
44. M. A. Henderson, J. White, H. Uetsuka, and H. Onishi, "Selectivity Changes During Organic Photooxidation on TiO<sub>2</sub>: Role of O<sub>2</sub> Pressure and Organic Coverage," *J. Catal.* **238**, 153 (2006).
45. E. C. Landis, S. C. Jensen, K. R. Phillips, and C. M. Friend, "Photostability and Thermal Decomposition of Benzoic Acid on TiO<sub>2</sub>," *J. Phys. Chem. C* **116**, 21508 (2012).
46. A. Song, D. Jing, and M. A. Hines, "Rutile Surface Reactivity Provides Insight into the Structure-Directing Role of Peroxide in TiO<sub>2</sub> Polymorph Control," *J. Phys. Chem. C* **118**, 27343 (2014).
47. A. Song, E. S. Skibinski, W. J. I. DeBenedetti, A. G. Ortoll-Bloch, and M. A. Hines, "Nanoscale Solvation Leads to Spontaneous Formation of a Bicarbonate Monolayer on Rutile (110) under Ambient Conditions: Implications for CO<sub>2</sub> Photoreduction," *J. Phys. Chem. C* **120**, 9326 (2016).

## **Chapter 2**

### **Experimental**

#### **2.1 Scanning Tunneling Microscope**

##### **2.1.1 The Working Principle of the Scanning Tunneling Microscope**

Scanning tunneling microscopy (STM) is a surface imaging technique that provides information on both morphology and electronic structure, potentially with atomic resolution. Since its invention by Gerd Binnig and Heinrich Rohrer in 1981,<sup>1</sup> STM has evolved into an essential tool for surface characterization and nanotechnology. STM uses electron tunneling between the tip and the sample to image. When the sample is brought close to the tip, the wavefunctions of the sample overlap with those of the tip. When an appropriate bias is applied between the sample and tip, a tunneling current is produced. Both the sample and the tip must be made of conductive or semiconductive materials. There are two scanning modes: constant current mode and constant height mode. Constant current mode was used for all of the images in this dissertation. In constant current mode, the vertical position of the tip is adjusted by a feedback loop to keep the tunneling current constant as the position of the tip is rastered across the surface. The tunneling current is dependent on the tip-surface distance, the local density of states in the tip and sample, and the voltage difference between the sample and the tip. Therefore, STM images reflect both the morphology and electronic structure of the sample surface.

##### **2.1.2 The Ultrahigh Vacuum System**

A commercial Omicron STM (VT STM XA / QPlus) was used for all experiments in this dissertation. The STM was housed in an ultrahigh vacuum (UHV) chamber with a base pressure of  $10^{-10}$  mBar. The UHV chamber was evacuated by a turbomolecular pump (HiPace 300,

Pfeiffer Vacuum) and an ion pump (Gamma Vacuum). After exposure to atmosphere, the system was baked at 150°C for ~ 24 hr to reach a base pressure of  $10^{-10}$  mBar. Samples and STM tips were transferred through a loadlock. In addition to the turbomolecular pump and the ion pump, the chamber was also equipped with a titanium sublimation pump (TSP) with 3 filaments. A TSP is inefficient in removing some gases, such as inert gases and methane, but has a high pumping speed for other gases, such as hydrogen and nitrogen. The TSP was used in combination with the ion pump.

### **2.1.3 Components of the System**

In the Omicron STM, the sample is held stationary while the tip is rastered across the sample by a single-tube scanner,<sup>2</sup> as shown in Fig. 2.1. The scanner is fabricated from a single piezoelectric tube with four segmented external electrodes and an internal electrode. To achieve lateral motions, mirror symmetric driving voltages<sup>3</sup> are applied to one pair of the opposing external electrodes, making one side of the tube expand and the opposite side of the tube contract. The tube is made to bend perpendicular to the tube axis, producing the lateral motions. To produce vertical motions, a voltage is applied to the internal electrode, making the piezoelectric tube extend or contract. The maximum scan range is  $12 \times 12 \mu\text{m}^2$  in the  $x$ - $y$  direction and  $1.5 \mu\text{m}$  in the  $z$  direction. The microscope is vibration isolated by a spring suspension system to obtain stable tunneling conditions. The  $z$ -resolution is 0.01 nm, which is limited by the resolution of the electronics. Samples were mounted on a  $15 \times 18 \text{mm}^2$  stainless steel or tantalum sample plate.

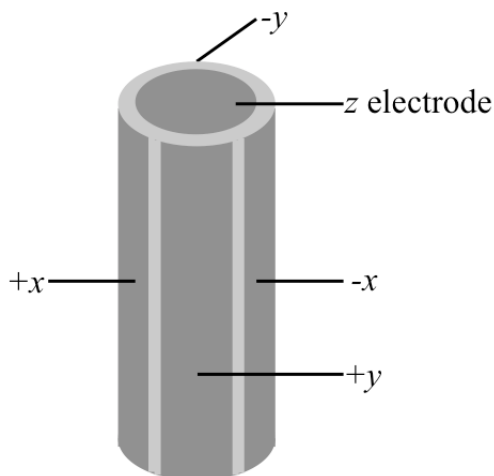


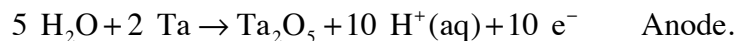
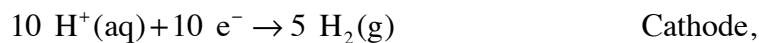
Figure 2.1 Schematic of the single-tube scanner

## 2.2 Sputter Ion Gun

Energetic ions generated by a PHI Model 04-161 sputter ion gun were used to sputter samples and sharpen tungsten STM tips. Argon ions were generated by backfilling the chamber with  $5 \times 10^{-5}$  mBar Ar gas, then bombarding the gas with 180 V electrons generated by a hot tungsten filament. An electron emission current of 20 mA was used. The  $\text{Ar}^+$  ions were then accelerated by a variable voltage, ranging from 0.5 kV to 2 kV. This voltage determined the kinetic energy of the  $\text{Ar}^+$  ions. The minimum beam size of  $\text{Ar}^+$  ions was 2 mm.

### 2.2.1 Sputter Gun Alignment and Calibration

The sputter gun needed to be aligned before sputtering samples and tips. This was performed visually using a  $15 \times 15 \text{ mm}^2$  tantalum sheet coated with a 100-nm-thick, electrochemically grown tantalum oxide film ( $\text{Ta}_2\text{O}_5$ ). The  $\text{Ta}_2\text{O}_5$  film was grown electrochemically by immersing two Ta sheets in 5–10%  $\text{KH}_2\text{PO}_4$  solution and applying a 25 V DC voltage across the sheets for a 3–5 seconds. The electrochemical reactions<sup>4</sup> are



The Ta<sub>2</sub>O<sub>5</sub> layer exhibited a uniform bluish purple color. The bluish purple Ta sheet was then rinsed copiously with deionized water and dried in air. The sheet was spot welded on a sample plate or a tip carrier and loaded into the UHV chamber. The Ta sheet was sputtered for 20 min using 1.5 keV, 3.5 μA Ar<sup>+</sup> ions. The Ar<sup>+</sup> beam sputtered away the Ta<sub>2</sub>O<sub>5</sub> film and revealed the silvery color of the underneath Ta metal sheet so that the position and size of the beam could be detected.

### **2.2.2 Preparation of Sputtered and Annealed Rutile (110) Samples**

Many investigators have used sputtering and annealing in UHV to produce clean rutile (110) surfaces.<sup>5-9</sup> This process is known to generate defects, such as O vacancies and Ti<sup>3+</sup> interstitials in the bulk crystal and on the surface.<sup>10</sup> Numerous sputtering and annealing cycles are typically used to generate clean, flat (1 × 1) rutile (110) surfaces. Many procedures have been reported. In general the crystals are sputtered by 1–2 μA of 1–2 keV Ar<sup>+</sup> ions for 10–30 min at room temperature while rastering the beam across the surface. Reported sputtering conditions vary widely. Annealing is performed after the sputtering process. Reported annealing temperatures also vary in a wide range, from 750 K to 1100 K, and the duration of annealing is 10–20 min. If the annealing temperature is too high, the rutile (110) surfaces will undergo a (1 × 2) reconstruction above 1150 K.<sup>5</sup>

For example, in one work rutile samples were cleaned with 2 μA of Ar<sup>+</sup> at 1–2 keV for 20–30 min followed by annealing to 850–1000K.<sup>6</sup> In another work samples were sputtered with 1 keV Ar<sup>+</sup> ions at room temperature and then annealed to 750–1100 K.<sup>7</sup> Another group sputtered a 10 × 10 mm<sup>2</sup> rutile (110) sample with 1 keV Ar<sup>+</sup> ions for 10 min followed by 20 min annealing at 700°C.<sup>8</sup> In some cases rutile crystals were annealed in O<sub>2</sub> to oxidize Ti<sup>3+</sup>. For example, in one work<sup>9</sup> the sample was sputtered by 1 μA of 1.5 keV Ar<sup>+</sup> ions for 10 min with a raster size of 6 ×

12 mm and annealed in  $2 \times 10^{-9}$  Bar of  $O_2$  at 900 K for 10 min. The sample was cooled down in  $O_2$ . The  $O_2$  annealing process induced a kind of “rosette restructuring” on the rutile (110) surface.<sup>11</sup> To prevent this, annealing in UHV was used in this work.

In this work, rutile (110) crystals were sputter cleaned using  $0.5 \mu A$  of 1.5 keV  $Ar^+$  ions generated with a 20 mA emission current and  $8 \times 10^{-6}$  mBar of Ar in the chamber. The energetic  $Ar^+$  ions were manually rastered across the surface. The 2 mm diameter  $Ar^+$  beam was used to bombard a  $3 \times 3$  raster pattern. Each spot was sputtered for 1 min, yielding a total sputtering time of 9 min. After sputtering the crystal was annealed at 900–1000 K for 15 min to produce an atomically flat, clean unreconstructed rutile (110) surface, as demonstrated by the STM image in Fig. 2.2.

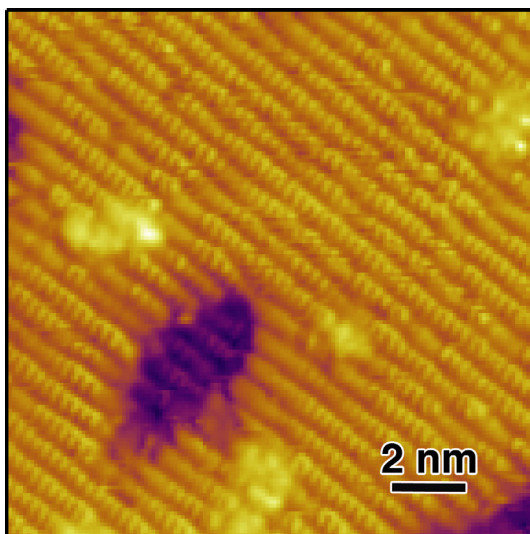


Figure 2.2 STM image of a rutile (110) surface prepared by sputtering and annealing. The surface was sputtered by  $0.5 \mu A$  of 1.5 keV  $Ar^+$  ions for 9 min and annealed at 900–1000 K for 15 min.

### 2.3 Tip Preparation

An atomically sharp tip is necessary to obtain atomically resolved images. The tips were

fabricated from recrystallized tungsten wire as described in Section 2.3.1, that was electrochemically etched, as described in Section 2.3.2 and sputter sharpened as described in Section 2.3.4. In some cases, the tip was heated by electron bombardment before sputtering as described in Section 2.3.3.

### 2.3.1 Recrystallization of Tungsten Wire

Polycrystalline tungsten wire was used to make STM tips because of its high melting point (3422°C), high mechanical strength, and simplicity of fabrication;<sup>12</sup> however, tips fabricated from cold-drawn polycrystalline tungsten suffer from apex instabilities. To prevent these instabilities, the W wire was first recrystallized following the procedure of Greiner and Kruse.<sup>13</sup>

A 12 cm sample of 0.125-mm-diameter, 99.95% W wire (Goodfellow Cambridge Ltd.) was mounted in the apparatus shown in Fig. 2.3 and evacuated to  $10^{-6}$  mBar. A DC voltage was applied using a TDK-Lambda Genesys<sup>TM</sup> 750W power supply. The current through the wire was gradually increased to 3.05 A over a period of 2 min. The wire was annealed at this current for 30 min. Attempts to measure the annealing temperature with an optical pyrometer were unsuccessful. After annealing, the terminal 1.5 cm of the wire was discarded. The annealed wire was noticeably brittle and broke easily when handled.

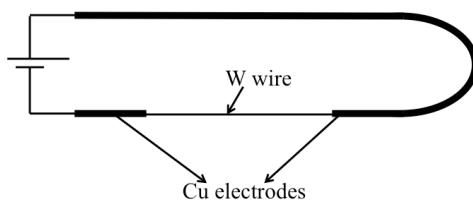
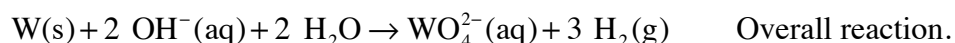
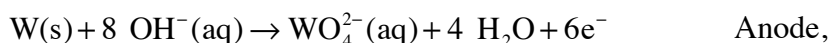
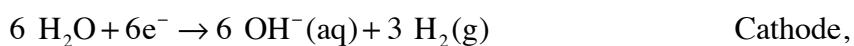


Figure 2.3 Recrystallization apparatus

### 2.3.2 Electrochemical Etching of Tungsten Wire

To obtain sharp STM tips, the recrystallized W wire was electrochemically etched in a 2 M KOH solution with a Pt cathode. A positive voltage was applied between the W wire and the Pt electrode, driving the electrochemical etching reactions<sup>14</sup>



At the W anode, the W was oxidized to soluble tungsten anions.

The shape of the tip was affected by the length of the wire immersed in the electrolyte solution. The etching reaction was fastest at the solution/air interface, leading to the formation of a thin neck at the interface. As the neck became narrower, gravity helped the part of wire in solution to drop off, producing a sharp tip at the end of the wire above the interface. If the length of immersed wire was too long, the sudden release of stored elastic energy due to the drop-off of the bottom wire would make the tip recoil, causing tip bending. If the length of immersion was too short, the tip would be etched away completely without the bottom part dropping. The choice of how long the wire was immersed in solution is empirical. Based upon many attempts, the length of the wire sticking out of the tip collet was chosen to be 0.065" and about 0.032" of the wire was immersed in the KOH solution.

In this work, recrystallized, 0.125 mm diameter W wire was used to make tips. The recrystallized wire was carefully inserted into the tip collet, leaving 0.065" exposed. Before etching, 0.032" of the wire was immersed in a 2 M KOH electrolyte solution in the center of a circular platinum counter electrode. A 6 V potential was used for etching.

In our design the etching reaction could be stopped immediately after the wire in the solution dropped. After the bottom wire dropped, a sharp tip was produced, and the area of the tip in the solution suddenly decreased, causing a dramatic decrease of the etching current. The sudden decrease of the etching current could be detected by monitoring the current differential signal. When the differential of the etching current was larger than 87 mV, the power was shut off automatically, and the etching reaction stopped. In this way, the residual wire in the solution would not continue to be etched, and the tip would not become blunt.

### **2.3.3 Electron-beam Heater for Tip Cleaning**

An electron-beam heater inside the UHV chamber was used to heat and clean the STM tip after the electrochemical etching.<sup>15</sup> Electrons were emitted from a hot thoriated tungsten filament in the electron-beam heater and accelerated to the tip apex. Electrons bombarded the tip, heating it up. In this work, an accelerating voltage of 1000 V was used. The tip was bombarded by electrons with an emission current of 1.20 mA for 5 sec.

### **2.3.4 Field-directed Sputter Sharpening of the Tip**

The last step of fabricating a sharp and stable tip was to sputter the tip with Ar<sup>+</sup> using the biased-probe, field-directed sputter sharpening technique developed by S. W. Schmucker *et al.*<sup>16</sup> Traditional sputter erosion, which uses a beam of inert gas ions directed along the tip axis, has been used to sharpen tungsten tips.<sup>17</sup> The drawback of this method is that thermal or radiation-induced diffusion prevents tips from becoming atomically sharp. To prevent this, a positive bias was applied to the tip during ion bombardment, creating a nonuniform electric field enhanced at the tip apex. Due to the spatially localized electric field at the tip apex, the Ar<sup>+</sup> flux was reduced at the apex, thereby preventing diffusion-driven blunting of the tip.

In this work, a 150 V positive potential was applied between the tip and ground. The tip was sputtered by 1.5 keV Ar<sup>+</sup> ions directed along the tip axis. The Ar<sup>+</sup> ions were ionized by electrons (emission current of 20 mA) in 5 × 10<sup>-5</sup> mBar Ar. The tip was sputtered for 40 min at the current of 3 μA. To prevent the metal on the tip collet from being sputtered and transferred to the insulating rings on the tip holder, the tip collet was protected with an alumina-based ceramic adhesive (Ceramabond 552).

## 2.4 X-ray Photoelectron Spectroscopy

### 2.4.1 The Principle of X-ray Photoelectron Spectroscopy

X-ray photoelectron spectroscopy (XPS) is a surface-sensitive, quantitative technique that is sensitive to elemental composition and oxidation state within a few nanometers of the surface. XPS is widely used by surface scientists due to its powerful surface and chemical sensitivity. The instrument consists of two parts: the x-ray source and the analyzer. The incident x-rays from the source eject electrons from the sample, and the ejected electrons are analyzed by the analyzer. Based on the work of Rutherford in 1914<sup>18</sup> as shown in Fig. 2.4, this process is quantified by the equation

$$E_B = h\nu - E_k - \phi_S - (\phi_A - \phi_S) = h\nu - E_k - \phi_A,$$

where  $E_B$  is the electron binding energy,  $h\nu$  is the energy of the x-ray photons,  $E_k$  is the kinetic energy of the photoelectrons,  $\phi_A$  is the work function of the analyzer, and  $\phi_S$  is the work function of the sample.<sup>19</sup>  $\phi_A$  is an adjustable instrumental correction factor. A commercial Omicron DAR 400 X-ray source and a Sphera II Energy Analyzer were used for the all the XPS spectra in this dissertation.

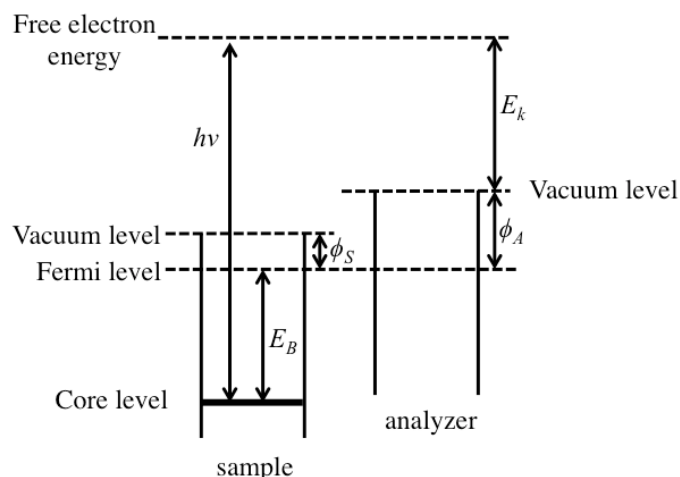


Figure 2.4 Schematic energy diagram for XPS

## 2.4.2 X-ray Source

The Omicron DAR 400 is a commercial x-ray source designed for XPS. Electrons were emitted from a hot thoriated tungsten filament, focused to a beam, then directed at a water-cooled Al or Mg anode, generating x-rays of a particular wavelength. Flowing water cooled the anode to minimize anode heating and evaporation. The generated x-rays passed through a thin aluminum window, which acted as a barrier to electrons and desorbing material.

The x-ray source was equipped with two anodes: a Mg anode with a  $K\alpha$  energy of 1253.6 eV and an Al anode with a  $K\alpha$  energy of 1486.6 eV. These anodes generate x-rays when electrons from the  $2p$  orbital of the L shell transfer to the K shell.<sup>20</sup>

## 2.4.3 XPS Analyzer

The Sphera II hemispherical energy analyzer used in this work was composed of an electrostatic lens, an in-lens aperture, a hemispherical analyzer, and a detector. Electrons emitted from the sample were collected and focused by the electrostatic lens. Then one of five in-lens apertures was selected to define a sample analysis area. The hemispherical analyzer dispersed electrons according to their energy across the exit plane and focused them in the angular

dimension, from the entrance to the exit plane. Electrons were accelerated by a positive voltage in the detector and hit the wall of the detector many times, leading to charge multiplication.

## 2.5 Sample Preparation

To get reproducible clean and smooth rutile (110) surfaces, the samples needed to be processed to remove morphological and chemical imperfections. Single side polished rutile (110) crystals (MTI Corporation) were used in the experiments. Rutile crystals were annealed at 900–1000 K for 10–15 min in UHV to introduce conductivity for STM imaging. The samples were then cleaned and etched in aqueous solutions using the following procedure. All labware, which was either glass or Teflon, was cleaned in a basic peroxide solution for 20 min, known as “standard clean 1” (SC1), which consisted of  $\text{NH}_4\text{OH}$  (BDH, 28–30%, A.C.S. grade),  $\text{H}_2\text{O}_2$  (J. T. Baker, 30%, CMOS grade) and ultrapure  $\text{H}_2\text{O}$  in a 1:1:5 by volume at 80°C. The labware was then rinsed in ultrapure water. After the labware was cleaned, rutile samples were cleaned and etched using either basic peroxide solutions or acidic peroxide solutions at 80°C. The basic peroxide solution consists of  $\text{NH}_4\text{OH}$ ,  $\text{H}_2\text{O}_2$ , and ultrapure  $\text{H}_2\text{O}$  in a 1:1:2 ratio by volume. The composition of the acidic peroxide solution was  $\text{HCl}$  (J. T. Baker, 36.5–38.0%, A.C.S. grade),  $\text{H}_2\text{O}_2$ , and ultrapure  $\text{H}_2\text{O}$  in a 1:1:2 ratio by volume. The etching solution was changed every 10 min and the total etching time varied depending on the experiment. After etching the rutile samples were thoroughly rinsed with ultrapure water and dried in air before being loaded into the UHV chamber.

Alternatively, rutile samples were cleaned by sputtering and annealing in UHV as discussed in Section 2.2.

## References

1. G. Binnig and H. Rohrer, "Scanning Tunneling Microscopy—from Birth to Adolescence," *Rev. Mod. Phys.* **59**, 615 (1987).
2. G. Binnig and D. Smith, "Single-Tube Three-Dimensional Scanner for Scanning Tunneling Microscopy," *Rev. Sci. Instrum.* **57**, 1688 (1986).
3. J. A. Stroscio and W. J. Kaiser, "Scanning Tunneling Microscopy," Academic Press, 1993; pp 56.
4. E. Gaul, "Coloring Titanium and Related Metals by Electrochemical Oxidation," *J. Chem. Educ.* **70**, 176 (1993).
5. C. Sánchez-Sánchez, M. Garnier, P. Aebi, M. Blanco-Rey, P. de Andres, J. Martín-Gago, and M. López, "Valence Band Electronic Structure Characterization of the Rutile TiO<sub>2</sub> (110)-(1× 2) Reconstructed Surface," *Surf. Sci.* **608**, 92 (2013).
6. E. C. Landis, S. C. Jensen, K. R. Phillips, and C. M. Friend, "Photostability and Thermal Decomposition of Benzoic Acid on TiO<sub>2</sub>," *J. Phys. Chem. C* **116**, 21508 (2012).
7. U. Diebold, J. Lehman, T. Mahmoud, M. Kuhn, G. Leonardelli, W. Hebenstreit, M. Schmid, and P. Varga, "Intrinsic Defects on a TiO<sub>2</sub> (110)(1× 1) Surface and Their Reaction with Oxygen: A Scanning Tunneling Microscopy Study," *Surf. Sci.* **411**, 137 (1998).
8. A. Thomas, W. Flavell, A. Mallick, A. Kumarasinghe, D. Tsoutsou, N. Khan, C. Chatwin, S. Rayner, G. Smith, and R. Stockbauer, "Comparison of the Electronic Structure of Anatase and Rutile TiO<sub>2</sub> Single-Crystal Surfaces Using Resonant Photoemission and X-Ray Absorption Spectroscopy," *Phys. Rev. B* **75**, 035105 (2007).
9. U. Diebold and T. Madey, "TiO<sub>2</sub> by XPS," *Surf. Sci. Spectra* **4**, 227 (1996).

10. M. A. Henderson, "A Surface Perspective on Self-Diffusion in Rutile TiO<sub>2</sub>," *Surf. Sci.* **419**, 174 (1999).
11. M. Li, W. Hebenstreit, and U. Diebold, "Oxygen-Induced Restructuring of the Rutile TiO<sub>2</sub> (110) (1× 1) Surface," *Surf. Sci.* **414**, L951 (1998).
12. Z. Yu, C. M. Wang, Y. Du, S. Thevuthasan, and I. Lyubinetsky, "Reproducible Tip Fabrication and Cleaning for UHV STM," *Ultramicroscopy* **108**, 873 (2008).
13. M. Greiner and P. Kruse, "Recrystallization of Tungsten Wire for Fabrication of Sharp and Stable Nanoprobe and Field-Emitter Tips," *Rev. Sci. Instrum.* **78**, 026104 (2007).
14. J. Ibe, P. Bey Jr, S. Brandow, R. Brizzolara, N. Burnham, D. DiLella, K. Lee, C. Marrian, and R. Colton, "On the Electrochemical Etching of Tips for Scanning Tunneling Microscopy," *J. Vac. Sci. Technol. A* **8**, 3570 (1990).
15. A.-S. Lucier. "Preparation and Characterization of Tungsten Tips Suitable for Molecular Electronics Studies," McGill University, 2004.
16. S. W. Schmucker, N. Kumar, J. R. Abelson, S. R. Daly, G. S. Girolami, M. R. Bischof, D. L. Jaeger, R. F. Reidy, B. P. Gorman, and J. Alexander, "Field-Directed Sputter Sharpening for Tailored Probe Materials and Atomic-Scale Lithography," *Nat. Commun.* **3**, 935 (2012).
17. S. Morishita, and F. Okuyama, "Sharpening of Monocrystalline Molybdenum Tips by Means of Inert-Gas Ion Sputtering," *J. Vac. Sci. Technol. A* **9**, 167 (1991).
18. E. Rutherford, "XXXVII. The Connexion between the B and  $\Gamma$  Ray Spectra," *The London, Edinburgh, and Dublin Philosophical Magazine and Journal of Science* **28**, 305 (1914).
19. S. Hofmann, "Auger-and X-Ray Photoelectron Spectroscopy in Materials Science: A User-Oriented Guide," Springer: Heidelberg, 2012; pp 528.

20. D. Briggs and M. P. Seah, "Practical Surface Analysis by Auger and X-Ray Photoelectron Spectroscopy," John Wiley, 1983.

## Chapter 3

### Preparation of Atomically Flat Rutile (110) Using Aqueous Peroxide Solutions and the Structure-Directing Role of Peroxide in TiO<sub>2</sub> Polymorph Control

#### 3.1 Introduction

Titanium dioxide, TiO<sub>2</sub>, is a semiconductor that has attracted significant amount of attention due to its high-profile applications, including the photoelectrolysis of water,<sup>1</sup> the photocatalytic decomposition of organic molecules,<sup>2-3</sup> and dye-sensitized solar cells.<sup>4-5</sup> Therefore, TiO<sub>2</sub> is a material that has great potential due to its cost effectiveness, high efficiency, and long-term chemical stability for sustainable energy and environmental remediation applications.

Chemically controlling TiO<sub>2</sub> morphology and studying its surface structure and reactivity is of significant importance. Previous studies have demonstrated that the reactivity of TiO<sub>2</sub> is sensitive to the crystal polymorph and the surface structure. There are three polymorphs of TiO<sub>2</sub> in nature: anatase, rutile, and brookite. Rutile is the thermodynamically stable and most abundant phase of TiO<sub>2</sub>, whereas anatase and brookite are metastable phases. These three polymorphs have different reactivity. Anatase and brookite are considered to have higher photoreactivity than rutile.<sup>6-7</sup> Even for the same crystalline phase, different facets exhibit different photocatalytic reactivity.<sup>8-9</sup> These findings imply that the surface structure influences the catalytic and photocatalytic reactivity of TiO<sub>2</sub>; therefore, many investigators have been working on synthesizing TiO<sub>2</sub> nanoparticles with different phases and shapes<sup>10-12</sup> to achieve enhanced photoreactivity. Most of these process optimizations have been empirical. Little is known about the surface reactions that underlie TiO<sub>2</sub> applications; however, many hypotheses have been advanced. This chapter demonstrates the chemical control of the rutile (110) surface and its site-specific reactivity in aqueous solutions.

The structure and reactivity of the rutile (110) surface prepared by sputtering and annealing in ultrahigh vacuum (UHV) has been studied by many surface scientists.<sup>13</sup> The structure of bare stoichiometric rutile (110) in UHV is determined by autocompensation,<sup>14</sup> as sketched in Fig. 3.1(a). In scanning tunneling microscope (STM) images, as shown in Fig. 3.1(b), the UHV-prepared rutile (110) surface is terminated by alternating bright rows and dark rows. The bright rows consist of five-fold coordinated Ti atoms, which will be referred to as  $\text{Ti}_{5c}$ .<sup>14</sup> Each  $\text{Ti}_{5c}$  atom has one “dangling bond” perpendicular to the surface that can bind with other molecules, such as  $\text{H}_2\text{O}$ . The dark rows are composed of two-fold coordinated O atoms, usually called bridging O atoms. Each bridging O atom has one “dangling bond” that can bind, for example, to H. Annealing rutile (110) generates relatively straight steps preferentially parallel to the [001] and  $\langle 1\bar{1}1 \rangle$  orientations.<sup>15</sup> The process of sputtering and annealing leads to the formation of defects, such as  $\text{Ti}^{3+}$  and O vacancies. Many researchers have studied the reactivity of these sites on UHV-prepared rutile (110) surfaces. For example, O vacancies are the active sites for water dissociation, whereas water does not dissociate on defect-free rutile surfaces.<sup>16</sup> The reactivity of UHV-prepared rutile surface is dominated by the defect sites generated during sputtering and annealing.

In contrast, the “dangling bonds” on the rutile surface will be completely saturated in technologically relevant environments as shown in Fig. 3.1(c). For example, when immersed in water, the  $\text{Ti}_{5c}$  sites are thought to be bound to O from either water molecules or OH, and the bridging O sites may be bound to protons, according to the solution pH. The net charge of the surface is zero in a solution of pH 5.8.<sup>17</sup> When the pH is higher or lower than 5.8, the surface is negatively charged or positively charged, respectively. The net charge of the surface is determined by the deprotonation reaction of water molecules on Ti sites ( $pK_a \sim 9$ ) and the

protonation of bridging O sites ( $pK_a \sim -1$ ).<sup>18</sup> Little is known about the step structure and surface reactivity of rutile in aqueous solutions or air. One goal of this research was to prepare rutile surfaces and study their structure and reactivity in technologically relevant conditions.

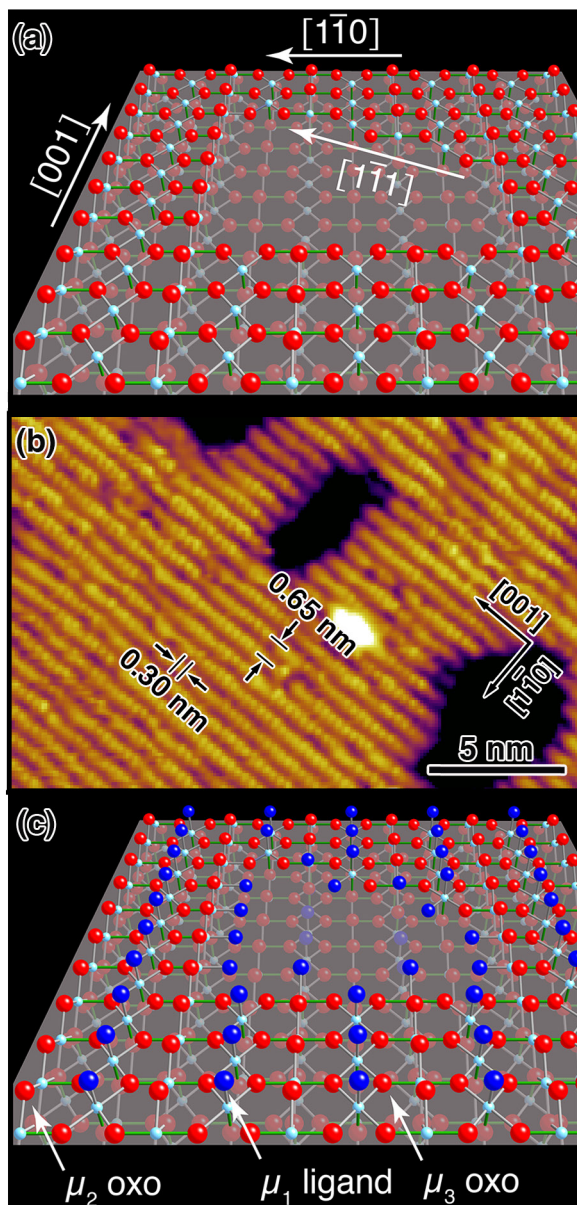


Figure 3.1 (a) Molecular model of UHV-prepared rutile (110) surface showing the  $Ti_{5c}$  rows and bridging O rows parallel to the [001] direction.

The preferential steps are parallel to the [001] and  $\langle 1\bar{1}1 \rangle$  directions. (b) STM image of UHV-prepared surface. The bright rows are Ti atom rows parallel to the [001] direction. (c) Molecular model of rutile (110) surface in aqueous solutions, with Ti in light blue, O in  $\mu_2$  and  $\mu_3$  oxo bridges in red, and O in aquo ligands in blue (protons not shown because of pH-dependent deprotonation). The green Ti-O bonds are  $\sim 2\%$  longer than the grey bonds.

This chapter will show that atomically flat rutile (110) surfaces were prepared using aqueous basic peroxide solutions. The surface was characterized by flat terraces and straight steps, whose orientation, structure, and reactivity were different from those prepared in UHV. The morphology was explained by the site-specific (anisotropic) etching reaction of the surface. Surface science techniques combined with kinetic Monte Carlo simulations revealed the relative reactivity of surface sites.

The peroxo ligand,  $O_2^{2-}$ , plays an important role in this etching reaction and the growth reactions of  $TiO_2$  nanocatalysts. The peroxo ligand is a promising structure-directing agent in the syntheses of nanoscale  $TiO_2$ .<sup>19</sup> Aqueous Ti chemistry is controlled by extremely fast condensation reactions. Compared to the extremely water-sensitive titanium inorganic salts, titanium peroxo complexes are stable and water-soluble,<sup>20</sup> making them good precursors of growth reactions. The peroxo-containing precursors are thought to retard hydrolysis reactions and lower condensation rates, thus producing well-controlled nanocrystals.<sup>19, 21</sup> The use of peroxo-containing precursors also excludes the presence of organic ligands and foreign ions, such as  $Cl^-$ , which cannot be easily eliminated by sequential thermal treatments.<sup>19, 22</sup> This research shows that  $O_2^{2-}$  has another important role: neighboring bonds are destabilized by the

peroxo ligands and become more labile. This destabilization introduces a degree of reversibility to the growth reaction, promoting the synthesis of well-ordered crystals. In the etching reaction, the destabilization caused by peroxo ligands leads to the cleavage of neighboring bonds and removal of Ti atoms.

### 3.2 Experimental

Polished  $5 \times 10$  mm rutile (110) samples (MTI Corporation) were used. Before the experiment, samples were annealed at 930 K for 8 min to introduce sufficient conductivity for STM analysis. Samples were then immersed in a basic peroxide solution at 80°C. The composition of the basic peroxide solution was  $\text{NH}_4\text{OH}$  (30%, EMD, ACS grade),  $\text{H}_2\text{O}_2$  (30%, J. T. Baker, CMOS grade) and ultrapure water in a ratio of 1:1:2 by volume. The basic peroxide solution was refreshed every 10 min to prevent the degradation of  $\text{H}_2\text{O}_2$ . The *pH* of fresh basic peroxide solution was 10.7, as measured by a *pH* meter (Orion, 290A) at 20°C. As a comparison the sample was also etched by a 1:3 mixture of  $\text{H}_2\text{O}_2/\text{H}_2\text{O}$  with a *pH* of 10.9 that was adjusted by dropwise addition of concentrated NaOH solutions (50%, J. T. Baker, electronics grade). The *pH* of the basic peroxide solution decreased to 9.6 after heating at 80°C for 11 min.

After being removed from the basic peroxide solution, the sample was rinsed with ultrapure water and introduced into a UHV chamber with a base pressure of  $2 \times 10^{-10}$  mBar. The surface was imaged with an Omicron STM (VT STM XA / QPlus, see Section 2.1.2) before and after heating to  $\sim 500$  K for 30 min. This mild heating did not introduce morphological changes. The tunneling condition was +1.8 V and 1 nA.

The surface was also characterized with an Omicron x-ray photoelectron spectrometer. X-rays of 1253.4 eV from an unmonochromated Mg source were used in this work. Photoelectrons emitted at 70° from the surface normal were analyzed by a hemisphere analyzer (Omicron

Sphera). XPS spectra were always obtained room temperature. Either a Shirley or Tougaard background was subtracted from all the spectra.

### 3.3 Results

#### 3.3.1 Preparation of near-perfect surface

An atomically flat and clean rutile (110) surface was produced after 20 min reaction in the basic peroxide solution at 80°C as shown by the STM image in Fig. 3.2. There were very few pits on the surface. Wide terraces were separated by steps of 3.25 Å height, the single step height, as shown in the inset of Fig. 3.2. The steps were composed of straight segments along perpendicular directions, the [001] and  $[1\bar{1}0]$  orientations. In contrast, the steps on annealed surfaces in UHV adopt thermodynamically preferred configurations, parallel to the [001] and  $\langle 1\bar{1}1 \rangle$  directions. This difference in step structure emphasizes the importance of studying rutile surface structure and chemistry in technologically relevant environments.

The surface morphology characterized by flat terraces and straight steps implies a highly anisotropic etching reaction. Straight steps can only be produced if the kink sites were removed much faster than the step steps. The flat terraces with few pits indicated that the terrace sites were much less reactive than kink sites and step sites. What is the structure of kink sites and step sites? What is the anisotropic etching reaction?

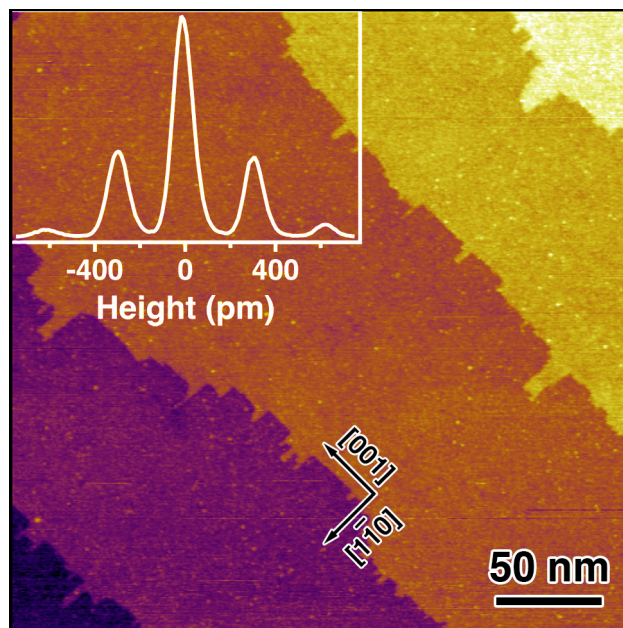


Figure 3.2 STM image of a rutile (110) surface after immersion in a basic peroxide solution for 20 min at 80°C. The inset is the histogram of the surface height, showing the production of atomically high steps.

### 3.3.2 XPS analysis of chemical composition

XPS analysis confirmed that the surface after basic peroxide etching was nearly contamination free with only Ti, O and a small amount of C as shown in Fig. 3.3(a). No N was detected.

The high-resolution Ti  $2p$  spectra in Fig. 3.3(b) showed that the surface was nearly ideal, without reduced Ti defects. The Ti  $2p$  spectra consisted of two transitions. The transition at 459.2 eV was assigned to Ti  $2p_{3/2}$ , and the transition at 464.9 eV was assigned to Ti  $2p_{1/2}$ .<sup>23</sup> No shoulders corresponding to Ti<sup>3+</sup> defects were observed at ~2 eV lower binding energy than Ti<sup>4+</sup>. Sputtered and annealed rutile samples always have Ti<sup>3+</sup> defects, in part because the Ar<sup>+</sup> bombardment preferentially sputters O atoms from the sample, reducing Ti<sup>4+</sup> to Ti<sup>3+</sup>. The fact that surfaces had no surface Ti<sup>3+</sup> after basic peroxide etching was expected, as peroxide is a

powerful oxidant.

Figure 3.3(c) showed that the predominant transition of O 1s spectra at 530.5 eV was assigned to lattice O in TiO<sub>2</sub>. In addition, a smaller transition with a binding energy ~2 eV higher than the lattice O transition was observed. The temperature-dependent spectra show that the smaller transition disappeared with heating above 593 K. This transition was not from water, as water molecules on rutile surfaces have a binding energy around 534 eV.<sup>24</sup> The absence of water was consistent with previous results showing the rapid desorption of water molecules at room temperature in vacuum.<sup>24-25</sup> Instead, the O 1s transition around 532.5 eV was from carbonate-containing molecules adsorbed on the surface, which will be discussed in details in Chapter 4.<sup>26</sup>

The high-resolution C 1s spectra indicated that the surface was covered with carbonate-containing species. The C 1s spectra consisted of two transitions. The transition at ~289.2 eV was assigned to the carbonate-containing molecules, whose desorption from the surface resulted in the decreased intensity with heating. The transition at ~285.2 eV was from adventitious carbon. The details of the carbonate-containing molecules will be discussed in Chapter 4.<sup>26</sup>

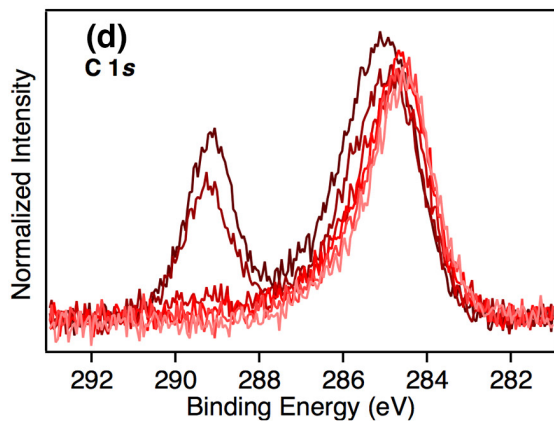
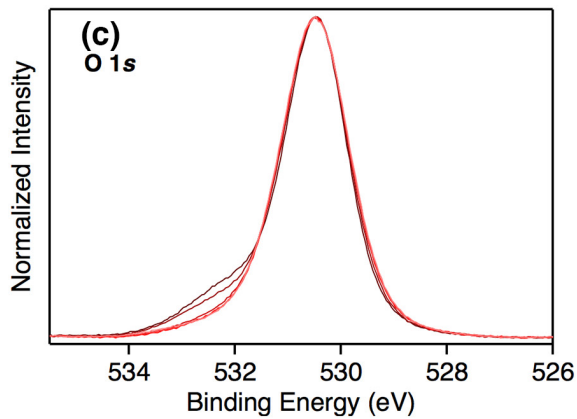
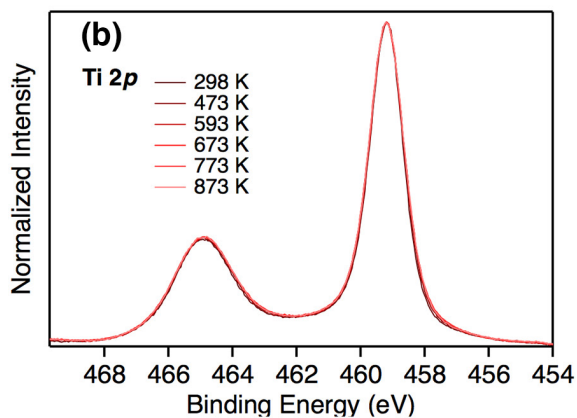
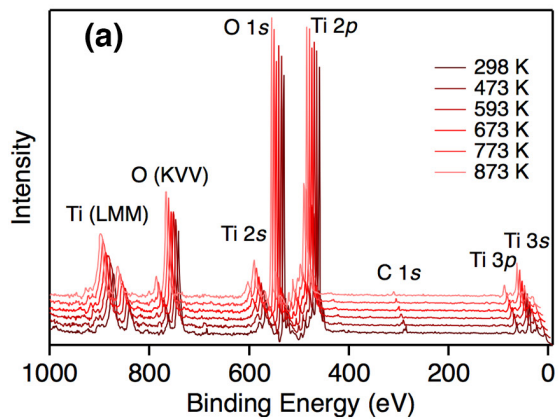


Figure 3.3 XPS spectra of rutile (110) surface after reaction in basic peroxide solution as a function of annealing temperature. (a) XPS survey spectra, (b) high-resolution spectra of the Ti 2*p* region, (c) high-resolution spectra of the O 1*s* region, and (d) high-resolution spectra of the C 1*s* region

### 3.3.3 Pits shape evolution reveals reactivity

To figure out the structure and relative reactivity of kink and step sites, the morphological evolution of an initially pitted surface was studied by STM. Thermal annealing of the rutile (110) surface generated a low density of initially irregular pits as shown in Fig. 3.4(a). The annealing process is known to produce a significant concentration of O vacancies, which cannot be observed in the low magnification image.<sup>14</sup>

Morphological changes of the surface were observed as shown in Fig. 3.4 and Fig. 3.5 after the initial surface with irregular pits was immersed in basic peroxide solutions at 80°C for different periods of time. After 2 min of reaction, the initially irregular pits grew larger in area, and adopted a rectangular habit as shown in Fig. 3.5(a). The edges of the pits were straight and perpendicular to one another. The orientations of the straight steps were determined from the high-resolution STM image in Fig. 3.5(b), which was taken in the rectangular region indicated by the box in Fig. 3.5(a). The bright rows in Fig. 3.5(b) were rows of Ti atoms that were parallel to the [001] direction. This image shows that the longer sides of the rectangular etch pits were parallel to the  $[1\bar{1}0]$  direction, and the shorter sides were parallel to the [001] direction. After 5 min of reaction, the etch pits still had a rectangular shape. After 15 min of reaction, an atomically flat surface was produced. Almost all of the pits were etched away, and only a few pits remained on the surface. No new pits were observed. The terraces were flat and separated by atomically

high steps. The steps were relatively straight and aligned with the  $[1\bar{1}0]$  direction, with some small segments along the  $[001]$  direction. This morphology indicated that the reaction was anisotropic.

The anisotropy of etch pits provided insights into the relative reactivity of surface sites. The straight steps indicated that kink sites were much more reactive than the step sites. In addition, previous studies showed that in an etching reaction concave structures, such as hollows or pits, will limit on slow etching planes or steps, whereas fast etching planes or steps will bound on convex structures, such as, spheres or islands.<sup>27-28</sup> The rectangular habit of etch pits implied that steps parallel to the  $[1\bar{1}0]$  direction were less reactive than steps parallel to the  $[001]$  direction in the basic peroxide solution.

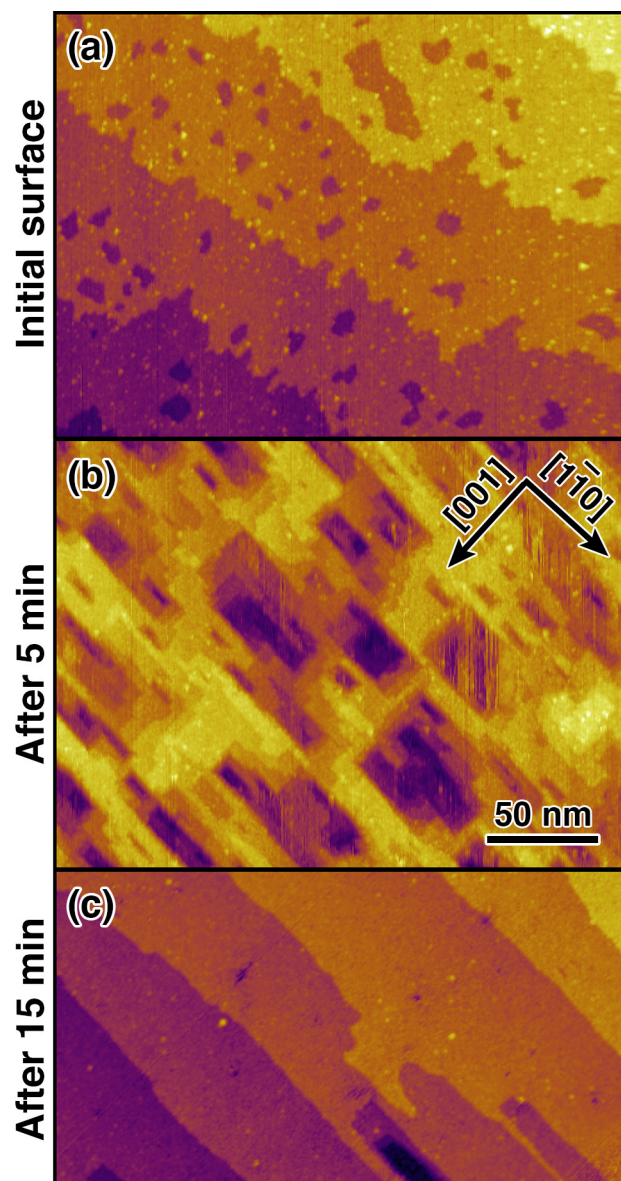


Figure 3.4 Pits evolution on a rutile (110) surface etched by basic peroxide solution. The three images were taken on the same sample. (a) The initial annealed surface with irregular pits, (b) after 5 min of reaction, and (c) after 15 min of reaction.

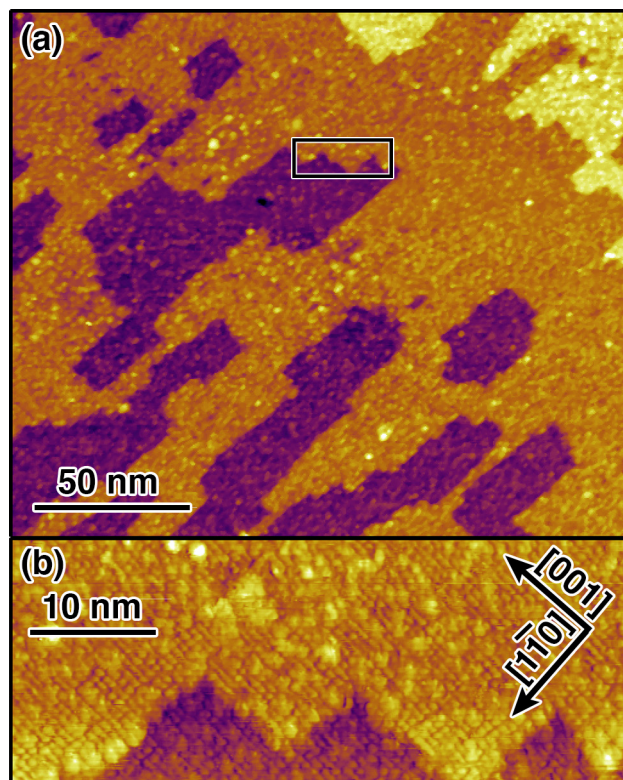


Figure 3.5 STM images of a rutile (110) surface etched by an 80°C basic peroxide solution for 2 min. (a) Large-scale STM image and (b) high resolution image of the region indicated by the black box in (a).

### 3.3.4 Identification of active species

Experiments were designed to identify the reactive species of the reaction. A 1:3  $\text{H}_2\text{O}_2/\text{H}_2\text{O}$  solution at  $p\text{H}\sim 10.9$  was prepared by dropwise addition of concentrated NaOH solutions. When this basic peroxide solution without  $\text{NH}_4^+$  was used in the etching reaction at 80°C, the etching rates and morphological changes of the rutile (110) surface were similar to the surface etched by a  $\text{NH}_4\text{OH}/\text{H}_2\text{O}_2/\text{H}_2\text{O}$  solution. In addition, no morphological changes were observed when the initially pitted surfaces were immersed in 1:3 mixtures of  $\text{NH}_4\text{OH}/\text{H}_2\text{O}$  or  $\text{HCl}/\text{H}_2\text{O}$  solutions at 80°C for 30 min or longer. These experiments suggest that  $\text{NH}_4^+$  is not the active species in the reaction.

These results indicated that  $\text{H}_2\text{O}_2$  was the reactive species in the etching reaction. This is consistent with previous studies, which showed that Ti or titanate acid could be dissolved by basic peroxide solutions, generating titanium peroxo complexes.<sup>20, 29</sup> The titanium peroxo complexes are relatively stable in aqueous solutions.<sup>20</sup>

### 3.3.5 Kinetic Monte Carlo simulations

To find out the structures and relative reactivity of reactive sites on the rutile (110) surface, kinetic Monte Carlo simulations were performed. The simulation assumed that individual Ti atoms could be randomly removed from the surface at a rate determined by the bonding of the atom. The rates were adjustable parameters. Each Ti atom was six-fold coordinated in a slightly distorted octahedral geometry. It was assumed that the steps did not reconstruct. The model adopted the solid-on-solid approximation, which forbids the formation of vacancies beneath occupied sites.<sup>30</sup> Diffusion of Ti atoms and desorption of Ti onto the surface were not allowed.

The chemistry of metal oxo complexes, which are small molecule analogues of  $\text{TiO}_2$ , provides insights into possible reactive sites on rutile.<sup>31</sup> In the rutile crystal Ti atoms are connected to one another through  $\mu_2$  or  $\mu_3$  oxo bridges. The surface  $\text{Ti}_{5c}$  sites are saturated by  $\mu_1$  ligands, such as  $\text{H}_2\text{O}$  or  $\text{OH}^-$  when immersed in aqueous solutions as shown in Fig. 3.1(c). The  $\mu_1$  ligands are expected to have the highest reactivity. The exchange rate of terminal  $\text{H}_2\text{O}$  or  $\text{OH}^-$  was estimated to be as high as 3400/s.<sup>32</sup> The  $\mu_2$  oxo sites, whose exchange rate is around 100/s,<sup>32</sup> are much less reactive than the  $\mu_1$  ligands. The  $\mu_3$  oxo sites with three Ti-O bonds are thought to be the least reactive sites. The reactivity of these ligands can be profoundly influenced by subtle changes of neighboring ligands and coordination geometry. For example, the deprotonation of  $\text{H}_2\text{O}$  ligands will result in significant increase in the reactivity of neighboring ligands.<sup>33</sup>

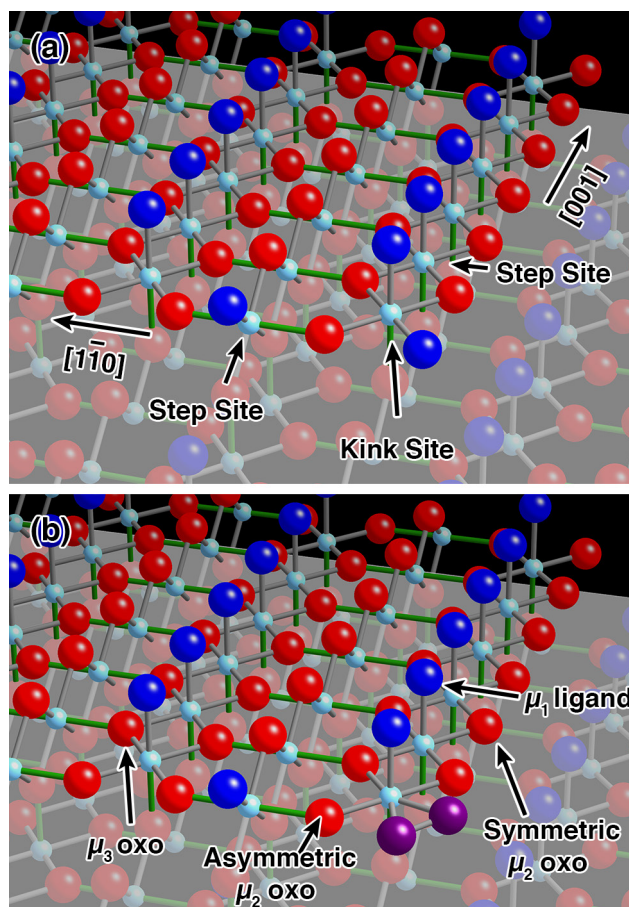


Figure 3.6 Molecular model of rutile (110) surfaces with Ti in light blue, O in  $\mu_2$  and  $\mu_3$  oxo bridges in red, and O in  $\mu_1$  ligands in blue. (a) shows the possible structure of kink sites and step sites. (b) shows the hypothesized bidentate bonding of peroxo ligands (purple).

The simplest candidate for a reactive site is the site with a single  $\mu_1$  ligand, such as  $Ti_{5c}$  sites on the terrace. If these sites were reactive, then the sites on terraces would be removed, producing new pits during etching. This is not consistent with the observed morphology characterized by flat terraces after etching, so the sites with only one  $\mu_1$  ligand were not reactive.

Another candidate reactive site is the site with two  $\mu_1$  ligands. Since some of these sites always exist on edges of islands as shown in Fig. 3.6, they could be the kink sites. The etching reactions were simulated on three initial surfaces as shown in Fig. 3.7. When the reaction only

attacked the sites with two  $\mu_1$  ligands, the initially rough steps were etched to straight steps parallel to the  $[001]$  and  $[1\bar{1}0]$  directions, respectively. Meanwhile, the initially circular pits were etched into squares. The square pits and straight steps did not continue to etch after formation. The square pits and straight steps did not continue to etch after formation. The straight steps were one of the characteristics of the experimental morphological evolution. This indicates that sites with two (or more)  $\mu_1$  ligands are candidate kink sites, but other reactive sites also needed to be included to match experiment.

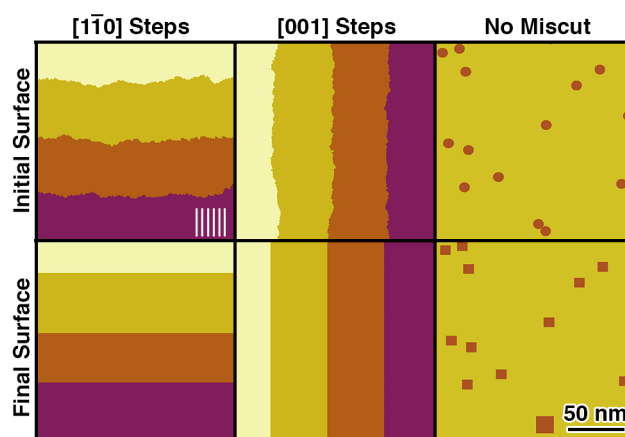


Figure 3.7 KMC simulations illustrating the kink site reactivity on three different initial surfaces. The only reactive sites in these simulations were the sites with two  $\mu_1$  ligands. The white bars indicate the direction of  $Ti_{5c}$  rows parallel to the  $[001]$  direction. The pits grow to squares, and the steps are etched to straight steps. The square pits and straight steps do not continue to etch.

A question then arises: why are some sites with  $\mu_1$  ligands reactive, but some others not? Inspired by the chemistry of metal oxo complexes, the reactivity of surface sites might be distinguished by their oxo bridges. The sites with two  $\mu_1$  ligands are reactive kink sites, while the sites with one  $\mu_1$  ligand and five  $\mu_3$  oxo bridges are unreactive terrace sites. The sites with a single  $\mu_1$  ligand and one or more  $\mu_2$  oxo bridges is, thus, possibly intermediate in reactivity

between the kink sites and terrace sites. These sites are candidate step sites. Two possible configurations of the step sites are demonstrated in Fig. 3.6.

Supposing that the Ti sites with one  $\mu_1$  ligand and (at least) one  $\mu_2$  ligand were the step sites, Fig. 3.8 compared the morphological evolution of two regimes: the fast kink etching regime and the slow kink etching regime. In the fast kink etching regime, the kink sites were etched much faster than the step sites ( $k_{\text{kink}} = 10^3 k_{\text{step}}$ ). The initially rough steps were etched into relatively straight steps and the initially circular pits were etched into squares. The straight steps of square pits were parallel to the [001] and  $[1\bar{1}0]$  directions. In the slow kink etching regime where  $k_{\text{kink}} = 10 k_{\text{step}}$ , the steps were rough, and the pits grew into a roughly circular habit. In both regimes, steps and pits never stopped etching. The straight and self-propagating steps in the fast kink regime were consistent with the experimental morphological evolution; however, the experimental etch pits adopted a rectangular habit, indicating that the straight steps parallel to two different orientations have different reactivity.

The rectangular etch pits with shorter sides parallel to the [001] direction indicate that the reactivity of steps parallel to the [001] direction is higher. This suggests that there were two types of step sites: sites with symmetric  $\mu_2$  oxo bridges and sites with asymmetric  $\mu_2$  oxo bridges as shown in Fig. 3.6. In rutile crystals there are two types of Ti-O bonds: equatorial Ti-O bonds (grey bonds in Fig. 3.6) and axial Ti-O bonds (green bonds) which are slightly longer. The symmetric oxo bridges contain two equatorial Ti bonds, while the asymmetric oxo bridges contain one equatorial Ti bond and one axial Ti bond. These two types of oxo bridges have very different geometries: the angle of symmetric oxo bridges is  $98.9^\circ$  while the angle of asymmetric oxo bridges is  $130.5^\circ$ .

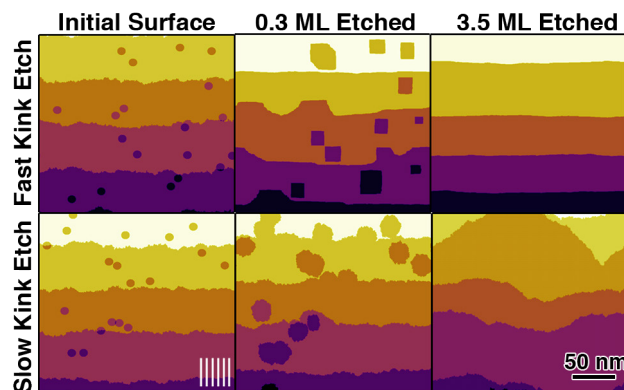


Figure 3.8 KMC simulations illustrating the fast kink etching ( $k_{\text{kink}} = 10^3 k_{\text{step}}$ ) and slow kink etching ( $k_{\text{kink}} = 10 k_{\text{step}}$ ) regimes. The white bars indicate the orientation of Ti atom rows parallel to the [001] direction. Simulations of surfaces with steps parallel to the [001] directions were also performed, and the same results were obtained.

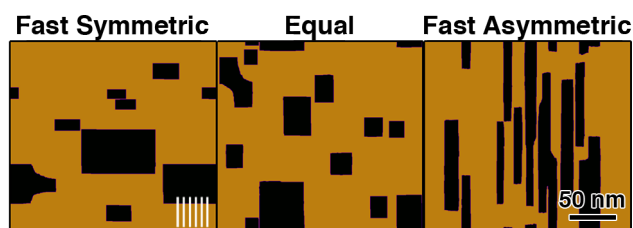


Figure 3.9 KMC simulations testing the relative reactivity of symmetric and asymmetric step sites. The kink sites were  $10^4$  times more reactive than step sites. In the fast symmetric step etching regime,  $k_{\text{sym step}} = 100 k_{\text{asym step}}$ . In the fast asymmetric step etching regime,  $k_{\text{asym step}} = 100 k_{\text{sym step}}$ . The white bars indicated the direction of  $\text{Ti}_{5c}$  atom rows parallel to the [001] direction.

Figure 3.9 tested the relative reactivity of the two types of step sites within the fast kink etching regime ( $k_{\text{kink}} = 10^4 k_{\text{step}}$ ). In the fast symmetric etching regime where the sites containing

symmetric  $\mu_2$  oxo bridges are etched faster ( $k_{\text{sym step}} = 100 k_{\text{asym step}}$ ), the etch pits adopted a rectangular habit with the longer side perpendicular to the [001] direction. In contrast, in the fast asymmetric etching regime ( $k_{\text{asym step}} = 100 k_{\text{sym step}}$ ) the pits were etched into rectangular habit with the longer side parallel to the [001] direction. The sites with one  $\mu_1$  ligand and (at least) one symmetric  $\mu_2$  oxo bridge, thus, were more reactive.

### 3.4 Discussion

#### 3.4.1 Site-specific reactivity

Near-ideal rutile (110) surfaces were prepared by simple basic peroxide solutions. The surface was characterized by atomically flat terraces and straight steps parallel to the [001] and  $[1\bar{1}0]$  directions. The steps have a different orientation, different structure, and different reactivity from the thermodynamically stable steps prepared by annealing at high temperature. This difference showed the importance of studying surface structure and chemistry in technologically relevant environments.

The morphology of basic peroxide etched surfaces was dominated by a highly site-specific etching reaction. This site-specific model was proposed based on the chemistry of metal oxo complexes. The most reactive sites are the sites with two  $\mu_1$  ligands. Although these sites are called “kink sites”, they are actually distinguished by the ligand count instead of their locations on the surface. The sites with one  $\mu_1$  ligand and (at least) one  $\mu_2$  oxo bridge are also reactive sites, but with a much smaller reactivity. Similarly, while these sites are called “step sites”, they are distinguished by the ligand count rather than location. The step sites with symmetric  $\mu_2$  oxo bridges are more reactive than those with asymmetric  $\mu_2$  oxo bridges. The least reactive sites are the terrace sites with one single  $\mu_1$  ligand, whose reactivity is at least six orders of magnitude lower than the kink sites according to the kinetic Monte Carlo simulations.

The structure of the rutile lattice itself determines the relatively high reactivity of step sites with symmetric  $\mu_2$  oxo bridges. In rutile, two neighboring  $\text{Ti}^{4+}$  ions can be connected by two oxo bridges through four equatorial Ti-O bonds, forming a rhombic  $\text{Ti}_2\text{O}_2$  motif. The distance between the two O atoms is 0.253 nm, producing strong repulsion between the O atoms. This repulsion locally destabilizes the lattice,<sup>34</sup> but in bulk rutile the repulsion is counter-balanced by other attractive interactions on both sides of the  $\text{Ti}_2\text{O}_2$  rhombus. For the rhombus on a step edge, the repulsion could not be counter-balanced because half of the interactions are removed, thus resulting in the increased reactivity of sites with symmetric oxo bridges.

A question may be asked: for the kink sites and step sites, does the relative orientation of the oxo ligands have an influence on the reactivity? For example, is there a difference in reactivity between the sites with two  $\mu_1$  ligands in a *cis* configuration and those in a *trans* configuration? In the simulations, the rutile geometry dictates that most of reactive sites are in the *cis* configuration. There was no evidence of different *cis/trans* reactivity in this system.

### 3.4.2 The role of peroxo ligands

It is important to understand what reaction occurs on rutile (110) surfaces; however, the low density of reactive sites, less than 0.1% of a monolayer for kink sites and 1% of a monolayer for step sites, and the instability of reaction intermediates make it impossible to study the etching reaction spectroscopically. Instead, the chemistry of metal oxo and peroxo complexes and the site-specific reactivity can help understand the reaction mechanisms.

Titanium (IV) ions are very unstable in aqueous solution and go through rapid condensation reactions, leading to the formation of polynuclear precipitates. Thus  $[\text{Ti}(\text{H}_2\text{O})_6]^{4+}$  ions are not observed in aqueous solutions. The hydrolysis of Ti (IV) ions occurs at low *pH*. The hydrolysis produces  $[\text{TiO}(\text{H}_2\text{O})_4]^{2+}$  or  $[\text{Ti}(\text{OH})(\text{H}_2\text{O})_5]^{3+}$  mononuclear species, which are stable only in

strongly acidic solutions.<sup>32, 35-36</sup> At higher  $pH$  values olation and oxolation reactions between compounds occur rapidly and simultaneously, producing amorphous  $TiO_2$ .<sup>37</sup>

Condensation and hydrolysis reactions of metal ions in aqueous solutions can be explained by the partial charge model.<sup>35, 37</sup> The partial charge model assumes that condensation continues until the mean electronegativity of products equal to the mean electronegativity of water (2.49). On the way from  $[Ti(H_2O)_6]^{4+}$  to  $[TiO(H_2O)_4]^{2+}$  and eventually to  $TiO_2$ , the mean electronegativity changes from 2.84 to 2.69 and eventually to 2.52, favoring the condensation reaction. This process can also be understood in terms of Ti partial charge  $\delta(Ti)$ . The partial charge of Ti changes from 0.97 in  $[Ti(H_2O)_6]^{4+}$  to 0.88 in  $[TiO(H_2O)_4]^{2+}$ , and eventually to 0.77 in  $TiO_2$ . The decrease of partial charge at Ti centers favors the nucleophilic olation and oxolation reactions.

When peroxo ligands,  $O_2^{2-}$ , are added into aqueous  $Ti^{4+}$  solutions, titanium peroxo complexes are produced.<sup>38</sup> The peroxo ligands substitute monodentate  $H_2O$  or  $OH$  ligands, binding to the  $Ti^{4+}$  centers in a side-on, bidentate geometry.<sup>38-40</sup> Some mononuclear species, such as  $[Ti(O_2)(OH)(H_2O)_4]^+$ , are stable in strong acidic solutions. As  $pH$  increases, these complexes slowly condense to form polynuclear species  $(Ti_2O_5)_q(OH)_y^{(2q-y)+}$  connected by multiple oxo and peroxo bridges.<sup>38</sup> The stability of Ti-peroxo bonds can be explained by the partial charge reduction at Ti centers and the bidentate bonding.<sup>38</sup>

In the basic peroxide etching reaction,  $H_2O_2$  works as a source of peroxo ligands and the base catalyzes the peroxo addition.<sup>19</sup> The addition of peroxo ligands to Ti centers decreases the partial charge at Ti, thus leading to the lability of neighboring Ti-O bonds and promoting their hydrolysis. In addition, peroxo ligands can directly attack  $\mu_2$  oxo bridges. Complexes containing two Ti centers connected by two  $\mu_2$  oxo bridges are the small molecule analogues of  $TiO_2$ . Studies of these compounds show that peroxo ligands either replace one of the oxo bridges or

bind to both Ti centers in a bidentate way by cleaving both  $\mu_2$  oxo bridges.<sup>41-42</sup>

The high reactivity of sites with two  $\mu_1$  ligands can also be explained. First, base catalyzed condensation is faster at sites with a higher partial charge. The sites with two  $\mu_1$  ligands have a high partial charge compared to other surface sites. Second, the sites with two  $\mu_1$  ligands have fewer oxo bridges to cleave.

The higher reactivity of sites with one  $\mu_1$  ligand and one  $\mu_2$  oxo bridge versus sites with one  $\mu_1$  ligand and five  $\mu_3$  oxo bridges is attributed to  $\mu_2$  bridges hydrolyzing much more rapidly than  $\mu_3$  bridges.<sup>43</sup> Nevertheless, the  $\mu_3$  oxo bridges must be cleaved eventually. Otherwise, the kink sites and step sites could never leave the surface. The cleavage of  $\mu_3$  oxo bridges is achieved by prior reaction of  $\mu_2$  oxo bridges. Replacement of  $\mu_2$  oxo bridges with peroxo ligands or hydroxo ligands increases the lability of neighboring  $\mu_3$  oxo bridges, thus accelerating the cleavage of  $\mu_3$  oxo bridges.<sup>43</sup> Therefore, in the etching reaction one of the roles of the peroxo ligands is to increase the lability of other Ti-O bonds, leading to the removal of Ti sites.

The role of peroxo ligands in etching reactions also helps to explain the importance of peroxo ligands in the  $\text{TiO}_2$  growth. The enhanced lability adds a degree of reversibility to growth, leading to the formation of well-ordered crystals.

### 3.5 Conclusions

Simple basic peroxide solutions produced near-perfect rutile (110) surfaces characterized by atomically flat terraces and straight steps. The etch pits adopted a rectangular habit during etching. The straight steps and edges of pits were parallel to the [001] and  $[1\bar{1}0]$  directions. The solution prepared surfaces had a different orientation, different structure, and different reactivity from those prepared in UHV. The morphological evolution could be explained by the site-specific reactivity of surface sites. The sites with 2  $\mu_1$  ligands were much more reactive than

those with one  $\mu_1$  ligand and (at least) one  $\mu_2$  oxo bridge, leading to the formation of straight steps. The difference in reactivities of symmetric  $\mu_2$  oxo bridges and asymmetric  $\mu_2$  oxo bridges results in the generation of rectangular pits.

The role of peroxo ligands in etching is to destabilize neighboring bonds and increase the lability of these bonds. In growth reactions, peroxo ligands not only block condensation, but also add a degree of reversibility to the growth, leading to the formation of well-ordered crystals.

### References

1. A. Fujishima, K. Kohayakawa, and K. Honda, "Hydrogen Production under Sunlight with an Electrochemical Photocell," *J. Electrochem. Soc.* **122**, 1487 (1975).
2. S. N. Frank and A. J. Bard, "Heterogeneous Photocatalytic Oxidation of Cyanide and Sulfite in Aqueous Solutions at Semiconductor Powders," *J. Phys. Chem.* **81**, 1484 (1977).
3. A. Fujishima, T. N. Rao, and D. A. Tryk, "Titanium Dioxide Photocatalysis," *J. Photochem. Photobiol. C: Photochem. Rev.* **1**, 1 (2000).
4. B. O'Regan and M. Grätzel, "A Low-Cost, High-Efficiency Solar Cell Based on Dye-Sensitized Colloidal TiO<sub>2</sub> Films," *Nature* **353**, 737 (1991).
5. B. E. Hardin, H. J. Snaith, and M. D. McGehee, "The Renaissance of Dye-Sensitized Solar Cells," *Nature Photonics* **6**, 162 (2012).
6. L. Liu, H. Zhao, J. M. Andino, and Y. Li, "Photocatalytic CO<sub>2</sub> Reduction with H<sub>2</sub>O on TiO<sub>2</sub> Nanocrystals: Comparison of Anatase, Rutile, and Brookite Polymorphs and Exploration of Surface Chemistry," *ACS Catal.* **2**, 1817 (2012).
7. T. Ohno, K. Sarukawa, and M. Matsumura, "Photocatalytic Activities of Pure Rutile Particles Isolated from TiO<sub>2</sub> Powder by Dissolving the Anatase Component in HF Solution," *J. Phys. Chem. B* **105**, 2417 (2001).

8. J. Lowekamp, G. Rohrer, P. M. Hotsenpiller, J. Bolt, and W. Farneth, "Anisotropic Photochemical Reactivity of Bulk TiO<sub>2</sub> Crystals," *J. Phys. Chem. B* **102**, 7323 (1998).
9. T. Ohno, K. Sarukawa, and M. Matsumura, "Crystal Faces of Rutile and Anatase TiO<sub>2</sub> Particles and Their Roles in Photocatalytic Reactions," *New J. Chem.* **26**, 1167 (2002).
10. Q. Xiang, J. Yu, and M. Jaroniec, "Synergetic Effect of MoS<sub>2</sub> and Graphene as Cocatalysts for Enhanced Photocatalytic H<sub>2</sub> Production Activity of TiO<sub>2</sub> Nanoparticles," *J. Am. Chem. Soc.* **134**, 6575 (2012).
11. M. Fernández-García, C. Belver, J. C. Hanson, X. Wang, and J. A. Rodriguez, "Anatase-TiO<sub>2</sub> Nanomaterials: Analysis of Key Parameters Controlling Crystallization," *J. Am. Chem. Soc.* **129**, 13604 (2007).
12. L. Sang, Y. Zhao, and C. Burda, "TiO<sub>2</sub> Nanoparticles as Functional Building Blocks," *Chem. Rev.* **114**, 9283 (2014).
13. U. Diebold and T. Madey, "TiO<sub>2</sub> by XPS," *Surf. Sci. Spectra* **4**, 227 (1996).
14. U. Diebold, "The Surface Science of Titanium Dioxide," *Surf. Sci. Rep.* **48**, 53 (2003).
15. U. Diebold, J. Lehman, T. Mahmoud, M. Kuhn, G. Leonardelli, W. Hebenstreit, M. Schmid, and P. Varga, "Intrinsic Defects on a TiO<sub>2</sub> (110) (1× 1) Surface and Their Reaction with Oxygen: A Scanning Tunneling Microscopy Study," *Surf. Sci.* **411**, 137 (1998).
16. R. Schaub, P. Thostrup, N. Lopez, E. Lægsgaard, I. Stensgaard, J. K. Nørskov, and F. Besenbacher, "Oxygen Vacancies as Active Sites for Water Dissociation on Rutile TiO<sub>2</sub> (110)," *Phys. Rev. Lett.* **87**, 266104 (2001).
17. D. A. Sverjensky, "Zero-Point-of-Charge Prediction from Crystal Chemistry and Solvation Theory," *Geochim. Cosmochim. Acta* **58**, 3123 (1994).

18. J. Cheng and M. Sprik, "Acidity of the Aqueous Rutile TiO<sub>2</sub> (110) Surface from Density Functional Theory Based Molecular Dynamics," *J. Chem. Theory Comput.* **6**, 880 (2010).
19. J.-Y. Piquemal, E. Briot, and J.-M. Brégeault, "Preparation of Materials in the Presence of Hydrogen Peroxide: From Discrete or "Zero-Dimensional" Objects to Bulk Materials," *Dalton Trans.* **42**, 29 (2013).
20. M. Kakihana, M. Kobayashi, K. Tomita, and V. Petrykin, "Application of Water-Soluble Titanium Complexes as Precursors for Synthesis of Titanium-Containing Oxides Via Aqueous Solution Processes," *Bull. Chem. Soc. Jpn.* **83**, 1285 (2010).
21. K. Tomita, V. Petrykin, M. Kobayashi, M. Shiro, M. Yoshimura, and M. Kakihana, "A Water-Soluble Titanium Complex for the Selective Synthesis of Nanocrystalline Brookite, Rutile, and Anatase by a Hydrothermal Method," *Angew. Chem. Int. Ed.* **45**, 2378 (2006).
22. N. Murakami, Y. Kurihara, T. Tsubota, and T. Ohno, "Shape-Controlled Anatase Titanium (IV) Oxide Particles Prepared by Hydrothermal Treatment of Peroxo Titanic Acid in the Presence of Polyvinyl Alcohol," *J. Phys. Chem. C* **113**, 3062 (2009).
23. J. Mayer, U. Diebold, T. Madey, and E. Garfunkel, "Titanium and Reduced Titania Overlayers on Titanium Dioxide (110)," *J. Electron. Spectrosc. Relat. Phenom.* **73**, 1 (1995).
24. G. Ketteler, S. Yamamoto, H. Bluhm, K. Andersson, D. E. Starr, D. F. Ogletree, H. Ogasawara, A. Nilsson, and M. Salmeron, "The Nature of Water Nucleation Sites on TiO<sub>2</sub> (110) Surfaces Revealed by Ambient Pressure X-Ray Photoelectron Spectroscopy," *J. Phys. Chem. C* **111**, 8278 (2007).
25. S. Yamamoto, H. Bluhm, K. Andersson, G. Ketteler, H. Ogasawara, M. Salmeron, and A. Nilsson, "In Situ X-Ray Photoelectron Spectroscopy Studies of Water on Metals and Oxides at Ambient Conditions," *J. Phys.: Condens. Matter* **20**, 184025 (2008).

26. A. Song, E. S. Skibinski, W. J. DeBenedetti, A. G. Ortoll-Bloch, and M. A. Hines, "Nanoscale Solvation Leads to Spontaneous Formation of a Bicarbonate Monolayer on Rutile (110) under Ambient Conditions: Implications for CO<sub>2</sub> Photoreduction," *J. Phys. Chem. C* **120**, 9326 (2016).
27. B. W. Batterman, "Hillocks, Pits, and Etch Rate in Germanium Crystals," *J. Appl. Phys.* **28**, 1236 (1957).
28. R. Jaccodine, "Use of Modified Free Energy Theorems to Predict Equilibrium Growing and Etching Shapes," *J. Appl. Phys.* **33**, 2643 (1962).
29. Y. Gao, Y. Masuda, Z. Peng, T. Yonezawa, and K. Koumoto, "Room Temperature Deposition of a TiO<sub>2</sub> Thin Film from Aqueous Peroxotitanate Solution," *J. Mater. Chem.* **13**, 608 (2003).
30. J. D. Weeks and G. H. Gilmer, "Dynamics of Crystal Growth," *Adv. Chem. Phys.* **40**, 157 (1979).
31. D. T. Richens, "Ligand Substitution Reactions at Inorganic Centers," *Chem. Rev.* **105**, 1961 (2005).
32. P. Comba and A. Merbach, "The Titanyl Question Revisited," *Inorg. Chem.* **26**, 1315 (1987).
33. M. Hartmann, T. Clark, and R. van Eldik, "Water Exchange Reactions and Hydrolysis of Hydrated Titanium (III) Ions. A Density Functional Theory Study," *J. Phys. Chem. A* **103**, 9899 (1999).
34. A. Fahmi, C. Minot, B. Silvi, and M. Causa, "Theoretical Analysis of the Structures of Titanium Dioxide Crystals," *Phys. Rev. B* **47**, 11717 (1993).

35. M. Henry, J. P. Jolivet, and J. Livage, "Aqueous Chemistry of Metal Cations: Hydrolysis, Condensation and Complexation," In *Chemistry, Spectroscopy and Applications of Sol-Gel Glasses*, Springer Berlin Heidelberg, 1992; pp 153.
36. M. Graetzel and F. P. Rotzinger, "Raman Spectroscopic Evidence for the Existence of Titanyl ( $\text{TiO}_2^+$ ) in Acidic Aqueous Solutions," *Inorg. Chem.* **24**, 2320 (1985).
37. J. Livage, M. Henry, and C. Sanchez, "Sol-Gel Chemistry of Transition Metal Oxides," *Prog. Solid State Chem.* **18**, 259 (1988).
38. G. Schwarzenbach, J. Muehlebach, and K. Mueller, "Peroxo Complexes of Titanium," *Inorg. Chem.* **9**, 2381 (1970).
39. V. Sergienko, "Structural Characteristics of Peroxo Complexes of Group IV and V Transition Metals. Review," *Crystallogr. Rep.* **49**, 907 (2004).
40. R. Guillard, J. M. Latour, C. Lecomte, J. C. Marchon, J. Protas, and D. Ripoll, "Peroxtitanium (IV) Porphyrins. Synthesis, Stereochemistry, and Properties," *Inorg. Chem.* **17**, 1228 (1978).
41. S. Kondo, K. Saruhashi, K. Seki, K. Matsubara, K. Miyaji, T. Kubo, K. Matsumoto, and T. Katsuki, "A  $\mu$ -Oxo- $\mu$ - $\eta^2$ : $\eta^2$ -Peroxo Titanium Complex as a Reservoir of Active Species in Asymmetric Epoxidation Using Hydrogen Peroxide," *Angew. Chem. Int. Ed.* **47**, 10195 (2008).
42. G.-C. Wang, H. H. Sung, I. D. Williams, and W.-H. Leung, "Tetravalent Titanium, Zirconium, and Cerium Oxo and Peroxo Complexes Containing an Imidodiphosphate Ligand," *Inorg. Chem.* **51**, 3640 (2012).
43. G. E. Brown, V. E. Henrich, W. H. Casey, D. L. Clark, C. Eggleston, A. Felmy, D. W. Goodman, M. Grätzel, G. Maciel, and M. I. McCarthy, "Metal Oxide Surfaces and Their Interactions with Aqueous Solutions and Microbial Organisms," *Chem. Rev.* **99**, 77 (1999).

## Chapter 4

### **Nanoscale Solvation Leads to Spontaneous Formation of a Bicarbonate Monolayer on Rutile (110) under Ambient Conditions: Implications for CO<sub>2</sub> Photoreduction\***

Anqi Song, Erik S. Skibinski, William J. I. DeBenedetti, Amnon G. Ortoll-Bloch, and Melissa A. Hines

#### **4.1 Abstract**

The chemical state of a catalyst *in operando* is particularly important for catalysts that target minority species, such as atmospheric CO<sub>2</sub> which has a concentration of only 400 ppm. A reaction can be promoted by the selective binding of reactants or hindered by molecules that block active sites. We show that adsorbed CO<sub>2</sub>, a very weakly bonded species on TiO<sub>2</sub>, is unlikely to play the key role in CO<sub>2</sub> photoreduction under ambient conditions, at least on rutile (110), as the vast majority of unsaturated Ti sites are terminated by a different, much more strongly bound carbonaceous species: adsorbed bicarbonate (HCO<sub>3</sub>). Using a combination of scanning tunneling microscopy (STM) and surface spectroscopies, we show that atmospheric CO<sub>2</sub> readily and stably displaces adsorbed H<sub>2</sub>O on rutile (110), creating a self-assembled monolayer of HCO<sub>3</sub> and H that is stable at room temperature even in vacuum. This reaction occurs on near-ideal, stoichiometric rutile (110) and does not require surface defects, such as O vacancies, Ti interstitials, or steps. This reaction is promoted both by the strong bidentate bonding of HCO<sub>3</sub> as well as the nanoscale H<sub>2</sub>O film that spontaneously forms on TiO<sub>2</sub> under ambient conditions. DFT calculations show that the nanoscale water layer adsorbed to rutile

\*Reprinted from A. Song, E. S. Skibinski, W. J. DeBenedetti, A. G. Ortoll-Bloch, and M. A. Hines, "Nanoscale Solvation Leads to Spontaneous Formation of a Bicarbonate Monolayer on Rutile (110) under Ambient Conditions: Implications for CO<sub>2</sub> Photoreduction," *J. Phys. Chem. C* **120**, 9326-9333 (2016) with permission from The Journal of Physical Chemistry C. Copyright 2016 American Chemical Society.

(110) solvates the products and changes the reaction energetics significantly. The chemical state of the catalyst *in operando* will also be affected by the half-monolayer of adsorbed H produced by the reactive dissociation of H<sub>2</sub>O.

## 4.2 Introduction

The chemical state of a catalyst under operating conditions affects its reactivity. A reaction can be promoted by the selective binding of reactants or hindered by molecules that block active sites. As a result, the reactivity of a catalyst under operating conditions, where multiple species compete for reactive sites, may be very different than predicted from studies of isolated reactants on catalysts in vacuum. In the ultimate limit, dilute species in air or solution spontaneously form complete monolayers — monolayers that can dramatically alter the chemical reactivity of the clean surface. Here, we show that under ambient conditions the prototypical TiO<sub>2</sub> surface, rutile (110), is terminated by a stable monolayer of bicarbonate, HCO<sub>3</sub>, that blocks unsaturated Ti atoms by binding to the surface with two Ti–O bonds.

This chemical state of a catalyst *in operando* is particularly important for catalysts that target minority species, such as atmospheric CO<sub>2</sub> which has a concentration of only 400 ppm. The combination of decreasing fossil fuel supplies and increasing anthropogenic CO<sub>2</sub> has generated intense interest in the photoreduction of CO<sub>2</sub> to C<sub>1</sub> products, such as methanol, methane, or formic acid, or higher,<sup>1</sup> particularly if this goal can be accomplished using an inexpensive, earth-abundant catalyst, such as TiO<sub>2</sub>. Pioneering experiments by Inoue *et al.*<sup>2</sup> demonstrated the feasibility of this goal using aqueous solutions of semiconducting nanoparticles; however, the low efficiencies of early experiments<sup>2</sup> and more recent ones<sup>1</sup> have precluded practical adoption. The advent of computational materials design has increased the impetus for rational catalyst improvement using techniques such as bandgap engineering, phase or morphology control,

doping, or co-catalysts; however, rational catalyst design requires a knowledge of the reaction mechanism *in operando* — a missing piece in current understanding.

The first step in CO<sub>2</sub> photoreduction on TiO<sub>2</sub> is often postulated to be the photogeneration of an electron-hole pair in the bulk nanocrystal followed by electron transfer to adsorbed CO<sub>2</sub> to form CO<sub>2</sub><sup>-</sup>.<sup>3-6</sup> This mechanism is motivated in part by molecular orbital considerations.<sup>7,8</sup> Electron transfer drives CO<sub>2</sub> from a linear to a bent geometry, which lowers the energy of the HOMO and activates the molecule towards further reaction. As a result, CO<sub>2</sub> photoreduction is thought to proceed through a bent CO<sub>2</sub><sup>-</sup> species.<sup>9</sup> Consistent with this, the reaction can be induced by direct injection of an electron from a scanning tunneling microscope (STM) tip into an adsorbed CO<sub>2</sub> molecule at cryogenic temperatures.<sup>10-12</sup>

The postulated mechanism suffers from a number of issues on TiO<sub>2</sub>. Perhaps most importantly, the residence time of adsorbed CO<sub>2</sub> on clean TiO<sub>2</sub> is very short at room temperature, as CO<sub>2</sub> desorbs almost immediately at temperatures above 150 K.<sup>13,14</sup> Second, recent *ab initio* calculations<sup>15</sup> have found no tendency for excited stoichiometric TiO<sub>2</sub> to transfer an electron to adsorbed CO<sub>2</sub>. Third, although surface defect sites, particularly reduced Ti sites adjacent to O vacancies, have been hypothesized to play a role in photoreduction, at least *in vacuo*, such sites rapidly oxidize under ambient conditions.<sup>16</sup>

We show that adsorbed CO<sub>2</sub> is unlikely to play the key role in CO<sub>2</sub> photoreduction under ambient conditions, at least on rutile (110), as the reaction sites are terminated by a different, much more strongly bound carbonaceous species, adsorbed bicarbonate (HCO<sub>3</sub>). Using a combination of STM and surface spectroscopies, we show that atmospheric CO<sub>2</sub> readily and stably displaces adsorbed H<sub>2</sub>O on rutile (110), creating a self-assembled monolayer of HCO<sub>3</sub> and H that is stable at room temperature even under ultrahigh vacuum (UHV) conditions. This

reaction occurs on near-ideal, stoichiometric rutile (110) and does not require surface defects, such as O vacancies, Ti interstitials, or steps.

This reaction is promoted both by the strong bidentate bonding of  $\text{HCO}_3^-$  as well as the nanoscale  $\text{H}_2\text{O}$  film that spontaneously forms on  $\text{TiO}_2$  under ambient conditions. DFT calculations show the formation of a bicarbonate monolayer from the reaction of  $\text{CO}_2$  and adsorbed  $\text{H}_2\text{O}$  on rutile (110) is endoergic. The addition of a nanoscale water layer, which solvates the products, changes the reaction energetics significantly, converting the previously endoergic reaction to an exoergic reaction. As a result, under ambient conditions rutile (110) is terminated by a bicarbonate monolayer that underlies the nanoscale  $\text{H}_2\text{O}$  film.

This presence of a stable bicarbonate monolayer on rutile (110), which is not observed in UHV experiments,<sup>14,17</sup> has important implications for  $\text{TiO}_2$  reactivity and photoreactivity in general, not just for  $\text{CO}_2$  photoreduction. For example, the long-standing debate regarding the availability of adsorbed H on the surface of  $\text{TiO}_2$  has focused on the  $\text{H}_2\text{O}$  dissociation reaction, which experiments<sup>18-20</sup> and most recent calculations<sup>21,22</sup> find to be disfavored at room temperature (in the absence of defects). In contrast, we show that  $\text{CO}_2$  promotes the reactive dissociation of  $\text{H}_2\text{O}$  under ambient conditions, producing a bicarbonate monolayer and a half-monolayer of adsorbed H.

These results demonstrate the critical need for studies on well-controlled photocatalyst surfaces in ambient and solution environments, where competition for reactive sites plays an important role. A materials-by-design approach to catalyst discovery requires understanding the state of the catalyst *under operating conditions*.

## 4.3 Experimental and Computational

### 4.3.1 Experimental Methods

Prior to use, rutile (110) samples for STM analysis (MTI Corp.) were thermally reduced in UHV (~5 min at 700 °C) to induce conductivity, whereas opposing faces of samples for infrared spectroscopy (Princeton Corp.) were beveled at 45° for analysis in the multiple-internal-reflection geometry. Immediately before use, all glassware was cleaned<sup>in</sup> a 1:1:5 solution by volume of 28% NH<sub>4</sub>OH (aq, BDH, ACS grade):30% H<sub>2</sub>O<sub>2</sub> (aq, J.T. Baker, CMOS grade):ultrapure H<sub>2</sub>O (Milli-Q) at 80°C for 10 min, then rinsed with ultrapure H<sub>2</sub>O.

Rutile (110) samples were etched to remove contamination and produce an atomically smooth surface.<sup>23</sup> The samples were first immersed in a 1:1:2 by volume NH<sub>4</sub>OH:H<sub>2</sub>O<sub>2</sub>:H<sub>2</sub>O solution at 80°C for 10 min, then in a 1:1:2 by volume of 37% HCl(aq, BDH, ACS grade):H<sub>2</sub>O<sub>2</sub>:H<sub>2</sub>O. Some samples were subsequently cleaned in UHV by repeated sputtering with a 1.5 keV, 0.45 μA beam of Ar<sup>+</sup> ions for 20 min followed by a 5 min anneal at 700°C. The hydrophobic benzoate monolayers used as a reference for infrared spectroscopy were prepared by immersing etched samples in a boiling 16 mM aq solution of benzoic acid (Sigma Aldrich, >99%).

After preparation, samples were transferred to a UHV chamber in an oil-free load lock or to a dry-air-purged infrared spectrometer. All heat treatments were performed in UHV for 30 min. STM images were obtained in UHV on a room-temperature sample using recrystallized tungsten tips<sup>24</sup> prepared by field-directed sputter sharpening.<sup>25</sup> Photoelectrons were excited by unmonochromated Mg Kα x-rays and detected at 45° from the surface normal. Small energy corrections (~0.05 eV) were applied to offset mild band bending,<sup>18</sup> using published reference energies.<sup>26</sup> Infrared spectra were collected in the multiple-internal-reflection geometry using a mercury-cadmium-telluride detector and ZnSe grid polarizer.

### 4.3.2 Computational Methods.

Reactions were modeled with  $2 \times 1$  periodically repeating slabs consisting of 5 TiO<sub>2</sub> trilayers separated by a 12.5 Å vacuum spacing with autocompensated surfaces.<sup>27</sup> During optimization, the positions of the bottommost TiO<sub>2</sub> layer and its terminating bridging O rows were held fixed. Calculations were performed using density functional theory (DFT) within the generalized gradient approximation<sup>28</sup> (GGA) with the Perdew, Burke, and Ernzerhof (PBE) exchange-correlation functional,<sup>29</sup> as implemented in the Vienna *ab initio* simulation package (VASP).<sup>30-33</sup> The functional was corrected for long-range dispersion interactions using the zero damping DFT-D3 method.<sup>34</sup> Electron-ion interactions were described using the projector augmented wave (PAW) method.<sup>35,36</sup> Electronic states were expanded in plane waves with a kinetic energy cutoff of 400 eV and a  $6 \times 6 \times 1$  Monkhorst-Pack grid of  $k$  points. Brillouin-zone integration was performed using Gaussian smearing. Solvation effects were studied using a combination of explicit H<sub>2</sub>O molecules and implicit solvation as implemented in VASPsol.<sup>37</sup> STM images were modeled within the Tersoff-Hamann approximation<sup>38</sup> as isosurfaces of constant local density of states at an energy equal to the tip-surface bias measured with respect to the surface Fermi energy.

## 4.4 Results

Three different approaches were used to prepare clean, well-controlled rutile (110) surfaces under ambient conditions. In the first two, the rutile surface was cleaned by sputtering and annealing in UHV, a process that creates a low density of O vacancy and concomitant Ti<sup>3+</sup> defects. These surfaces were then exposed to ambient laboratory air for ~5 min and optionally dipped in ultrapure H<sub>2</sub>O for 3 min. For brevity, we refer to these preparations as “sputtered + air” and “sputtered + H<sub>2</sub>O,” respectively, even though both preparations involved air exposure. In the

third, the rutile surface was chemically cleaned using basic then acidic peroxide solutions. This process slightly etches the surface,<sup>23</sup> producing atomically flat terraces as exemplified by Fig. 1(a). After cleaning, these samples were exposed to air for ~5 min before introduction to UHV for analysis. We refer to this preparation as “aqueous etch.”

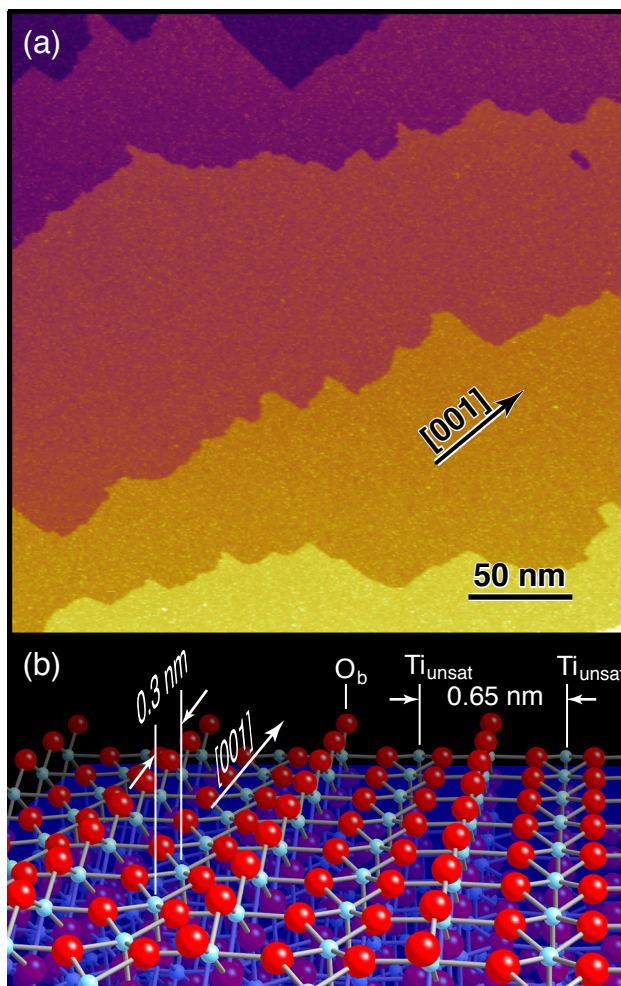


Figure 4.1 (a) STM image of aqueous etched rutile (110) surface, demonstrating the production of wide, smooth terraces. (b) Molecular model of the adsorbate-free rutile (110) surface with Ti atoms in light blue and O atoms in red. Rows of unsaturated Ti atoms and bridging O atoms are indicated by  $Ti_{\text{unsat}}$  and  $O_b$ , respectively.

Rutile (110) surfaces exposed to ambient air are covered with a nanoscale film of adsorbed H<sub>2</sub>O as shown by the infrared spectra in Fig. 4.2. In these spectra, the blue-shaded region corresponds to the O–H stretch of adsorbed H<sub>2</sub>O. The intensity of this transition decreased slowly with time in the dry-air-purged spectrometer, but never disappeared. As a result, this transition was always most intense in the first spectrum, taken here with *s*-polarized radiation, decreasing in the second spectrum, taken here with *p*-polarized radiation. O–H stretch vibrations specifically associated with HCO<sub>3</sub> and adsorbed H could not be resolved within this broad absorption band. The negative transitions near 3062 and at 3278 cm<sup>-1</sup> are due to C–H and O–H stretch vibrations, respectively, in the hydrophobic reference monolayer. Intense absorption in the rutile substrate prevented observation of modes below ~2160 cm<sup>-1</sup>, which precluded detection of C–O stretch vibrations.

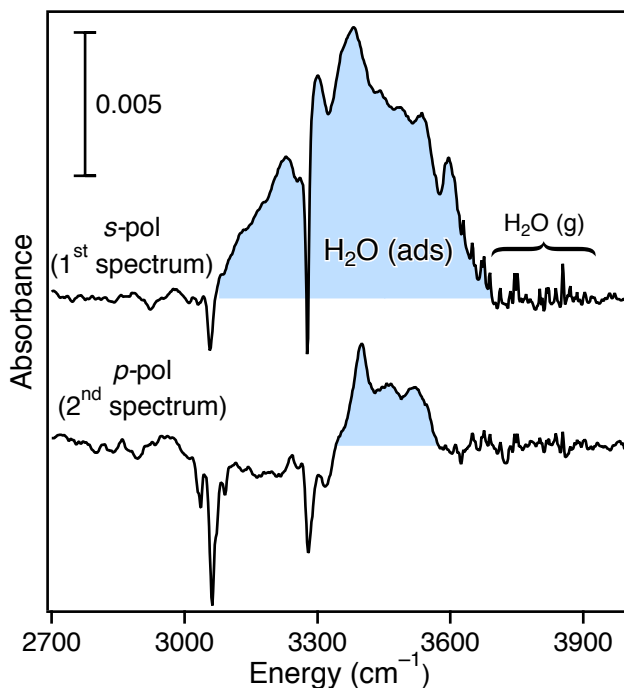


Figure 4.2 The O–H and C–H stretch region of infrared spectra of aqueous etched rutile (110) surfaces taken sequentially with *s*- then *p*-

polarized radiation and referenced to a surface terminated by a hydrophobic benzoate monolayer. The blue-shaded region corresponds to the O–H stretch of the nanoscale adsorbed H<sub>2</sub>O film, which partially evaporates in the dry-air-purged spectrometer.

Previous researchers quantified the thickness of the nanoscale H<sub>2</sub>O film on rutile (110) at room temperature using ambient pressure x-ray photoelectron spectroscopy (XPS).<sup>20,39</sup> At 100% relative humidity (RH), the rutile (110) surface is covered by a ~10-monolayer-thick film which decreases to a few-monolayer thickness at the 20-40% RH conditions typical of laboratory air. Consistent with our infrared data, XPS analysis shows the adsorbed water film persists to very low humidity conditions, disappearing only below 10<sup>-4</sup>% RH.

Previous researchers have also studied sub-monolayer to few monolayer films of crystalline H<sub>2</sub>O and D<sub>2</sub>O at cryogenic temperatures with high-resolution electron energy loss spectroscopy<sup>40</sup> and polarized infrared spectroscopy.<sup>41</sup> Thin crystalline films have ordered O–H bonds. Because of this, the spectra of cryogenic films are characterized by narrower vibrational linewidths that are sensitive to the electric field direction. In contrast, the room-temperature nanoscale H<sub>2</sub>O films observed in this study are disordered and have correspondingly broader transitions.

The formation of a bicarbonate monolayer on rutile (110) upon exposure to ambient air is evidenced by the development of periodic protrusions in STM images with a characteristic spacing of 0.60 nm, as shown in Fig. 4.3. The clean, adsorbate-free rutile (110) surface consists of rows of unsaturated Ti atoms separated by rows of bridging O atoms, as shown in Fig. 4.1(b). STM images of this surface are dominated by electronic effects, not surface morphology. As a result, the unsaturated Ti atoms image as rows of bright protrusions with a 0.30 nm spacing, separated by dark rows of bridging O atoms, as shown in Fig. 4.3(a). Upon exposure to air, the

bright rows are replaced by protrusions with a characteristic spacing of 0.60 nm — twice the Ti atom spacing — as seen in Fig. 4.3(b). This spacing reflects the bidentate bonding of  $\text{HCO}_3$  via two Ti–O bonds to the surface. These protrusions persist upon mild heating (here, 458 K), as shown in Fig. 4.3(c), but disappear at higher temperatures (here, 548 K), as shown in Fig. 4.3(d). Heating the surface above  $\sim 400$  K also leads to the development of few-nm-diameter white protrusions, most clearly seen in Fig. 4.3(d), which are attributed to the out diffusion of Ti interstitials in agreement with previous studies.<sup>42,43</sup>

The bicarbonate monolayer could not be rinsed off with liquid water. Fig. 4.4(a) shows a rutile (110) surface prepared by UHV sputtering and annealing. After this surface was removed from vacuum, rinsed in liquid water, and returned to vacuum, the periodic protrusions were still seen, as shown in Fig. 4.4(b).

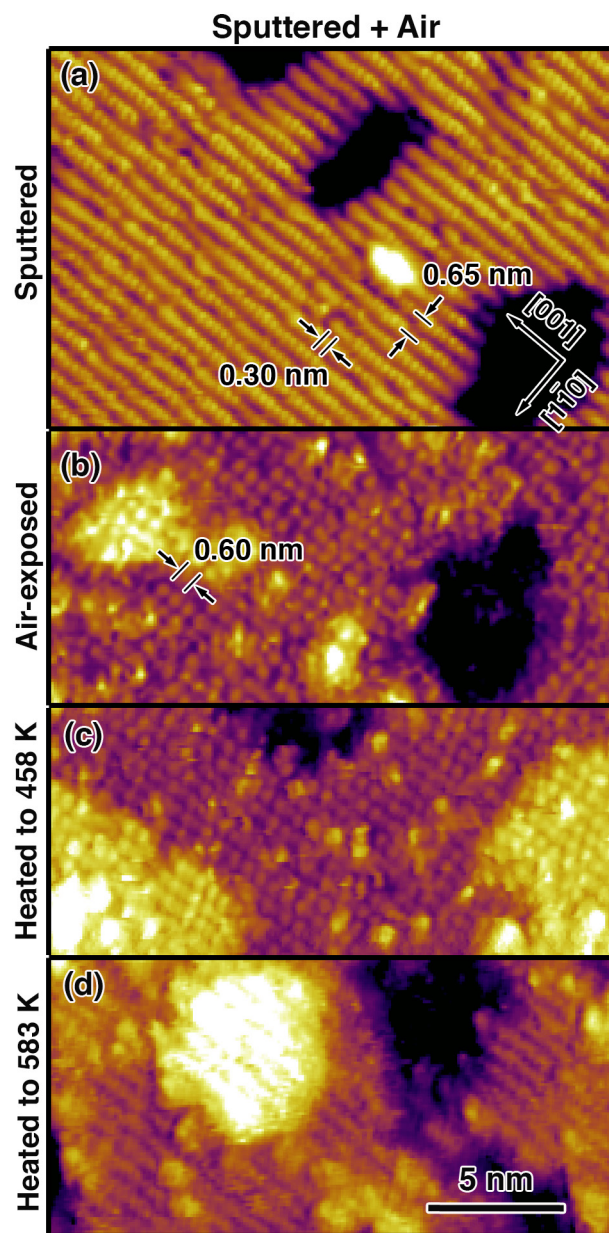


Figure 4.3 STM images of (a) a sputtered and annealed rutile (110) sample that was then (b) exposed to air. The bicarbonate monolayer leads to periodic protrusions with a characteristic 0.60 nm spacing. (c) A similar surface heated to 458K, and (d) 583 K.

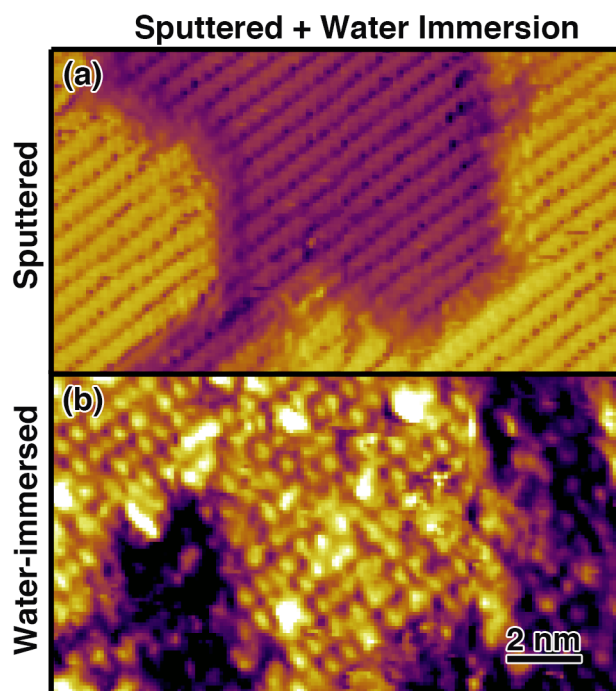


Figure 4.4 STM images of (a) a sputtered and annealed rutile (110) sample that was then (b) immersed in H<sub>2</sub>O for 3 min. The bicarbonate monolayer in (b) leads to periodic protrusions with a characteristic 0.60 nm spacing.

Bicarbonate formation is not correlated with the density of surface O vacancies and their concomitant Ti<sup>3+</sup> sites, as shown by the experiments on chemically cleaned rutile (110) surfaces in Fig. 4.5. This process produces a surface with no detectable O vacancies by STM or XPS analysis.<sup>23</sup> These surfaces, too, are covered with periodic protrusions, as shown in Fig. 4.5(a), which disappear after heating, as shown in Fig. 4.5(b).

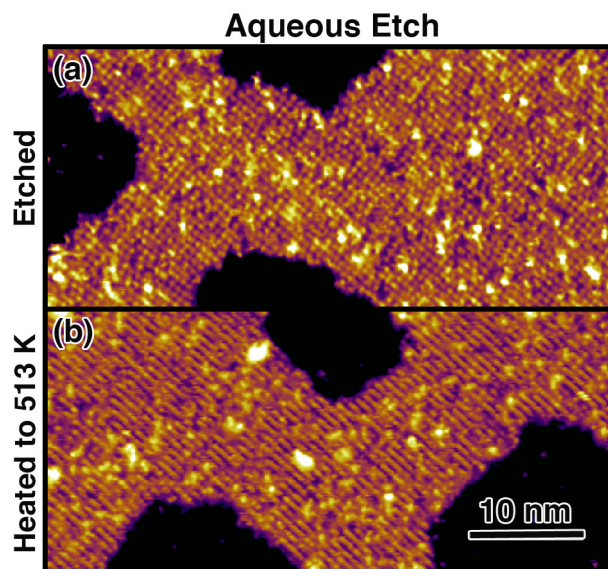


Figure 4.5 STM images of (a) an aqueous etched rutile (110) sample that was then (b) heated to 513 K. The bicarbonate monolayer observed in (a) is removed by the heat treatment.

The chemical identity of the bicarbonate monolayers was confirmed using XPS analysis. Rutile (110) surfaces exposed to air or aqueous solutions displayed transitions characteristic of carbonates in both the C 1s spectrum at 289.3 eV and the O 1s spectrum at 532.3 eV, as shown in Fig. 4.6(a) and (b). Consistent with the STM analysis, the intensity of these transitions decreased with heating, becoming undetectable above ~600 K. Small binding energy shifts in the C 1s spectrum with heating are attributed to small changes in band bending.<sup>18</sup> The absolute bicarbonate coverage, shown in Fig. 4.6(c), was determined from the integrated areas of the carbonate C 1s transition at 289.3 eV and the substrate Ti 2  $p_{3/2}$  transition. Together, these data show that the species observed in STM with a bidentate spacing had the same absolute density and thermal behavior as the carbonate-containing molecule observed in XPS, confirming the assignment of both to adsorbed bicarbonate.

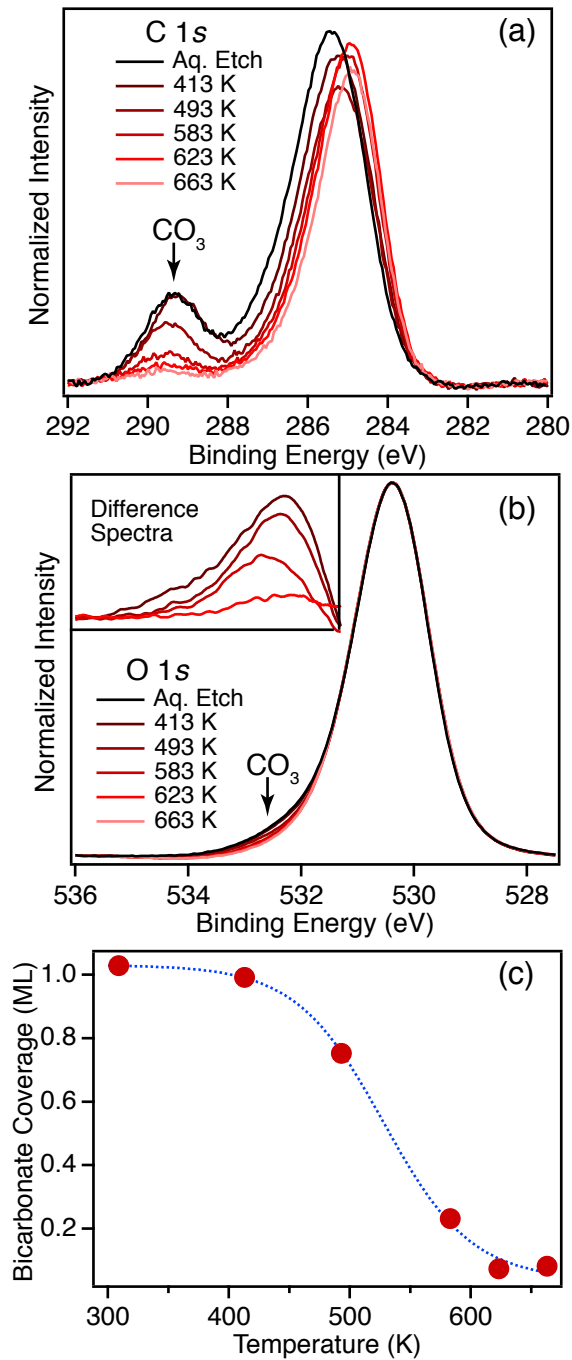


Figure 4.6 The (a) C 1s and (b) O 1s regions of XPS spectra obtained from a chemically etched rutile (110) sample as a function of temperature. The C 1s and O 1s spectra are normalized to the maximum amplitude of the Ti  $2p_{3/2}$  and O 1s transition, respectively. (c) The

absolute bicarbonate coverage measured by XPS. One monolayer corresponds to one bicarbonate for every two unsaturated Ti sites. The dotted line is the best fit sigmoid.

The XPS spectra also displayed a broad C 1s feature containing contributions from aliphatic (285 eV) and C–O-bonded (~286 eV) carbon, as also shown in Fig. 4.6(a). The intensity of this band and its thermal evolution varied somewhat between samples. This type of adventitious carbon has been observed on many different substrates by previous researchers and is ubiquitous on air-exposed samples.<sup>44</sup> These C-containing species are presumably adsorbed to the HCO<sub>3</sub> monolayer, as the absolute coverage measurements in Fig. 4.6(c) suggest that every unsaturated Ti atom is bound to HCO<sub>3</sub>.

The XPS spectra show little change upon heating to 413 K, even though STM images show the out diffusion of Ti interstitials. The low density of the out diffused Ti atoms would make the detection of any reaction products difficult, so we cannot determine whether these species react with surface adsorbates.

The reactions associated with bicarbonate formation on rutile (110) were investigated using DFT calculations as summarized in Table 1.

The most energetically stable product of the reaction of CO<sub>2</sub> and H<sub>2</sub>O is HCO<sub>3</sub> bound to two adjacent unsaturated Ti atoms and a H atom adsorbed to a bridging O atom, as shown in Fig. 4.7. This bidentate binding motif is characteristic of carboxylic acids on rutile (110) and leads to very strong adsorption. In comparison, H<sub>2</sub>O, which bonds to rutile (110) through a single Ti–O bond, has a binding energy only 60% of that of bicarbonate. The persistence of adsorbed HCO<sub>3</sub> after H<sub>2</sub>O evaporation in vacuum, as shown in Fig. 4.3, is consistent with the relative energetics of HCO<sub>3</sub> and H<sub>2</sub>O binding.

Table 4.1: Calculated energies of reaction on rutile (110) at full monolayer coverage. A  $2 \times 1$  rutile (110) supercell contains 2 unsaturated Ti atoms, so a full monolayer corresponds to 2  $\text{H}_2\text{O}$ , 2 H, or 1  $\text{HCO}_3$ .

Reaction	$\Delta E$ (kJ/mol)
1 $\text{H}_2\text{O} (\text{g}) + \text{CO}_2 (\text{g}) \rightarrow \text{HCO}_3 (\text{ads}) + \text{H} (\text{ads})$	-167.8
2 $2 \text{H}_2\text{O} (\text{ads}) + \text{CO}_2 (\text{g}) \rightarrow \text{HCO}_3 (\text{ads}) + \text{H} (\text{ads}) + \text{H}_2\text{O} (\text{g})$	44.7
3 $2 \text{H}_2\text{O} (\text{ads, aq}) + \text{CO}_2 (\text{g}) \rightarrow \text{HCO}_3 (\text{ads, aq}) + \text{H} (\text{ads, aq}) + \text{H}_2\text{O} (\text{ads, aq})$	-41.7
4 $\text{HCO}_3 (\text{ads, aq}) + \text{H} (\text{ads, aq}) \rightarrow \text{CO}_3 (\text{ads, aq}) + 2 \text{H} (\text{ads, aq})$	42.8

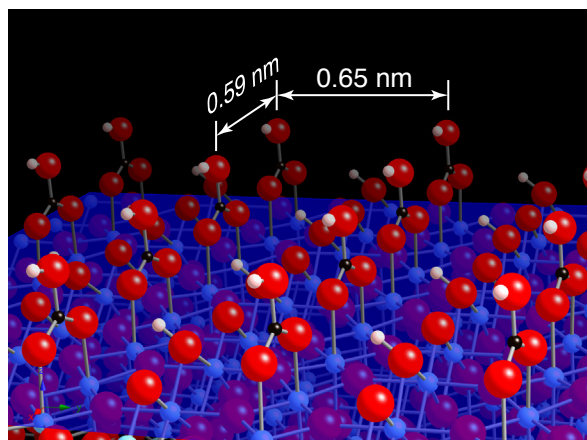


Figure 4.7 Structure of adsorbed  $\text{HCO}_3$  and H determined from DFT calculations with Ti, O, C, and H atoms in light blue, red, black, and pink, respectively.

The salient question is whether the binding of  $\text{HCO}_3$  is strong enough to displace adsorbed  $\text{H}_2\text{O}$  at the surface, as suggested by the experimental data. The direct reaction of gaseous  $\text{CO}_2$  with an adsorbed  $\text{H}_2\text{O}$  monolayer to form the adsorbed bicarbonate monolayer imaged in STM is

endoergic, as shown by Rxn. (2). In comparison, if this reaction occurs within the nanoscale H<sub>2</sub>O film, as shown by Rxn. (3), the reaction is exoergic, in agreement with previous calculations.<sup>45</sup>

Of course, the extent of a reaction is controlled by the free energy of the reaction, which has both energetic and entropic components. While the entropic contributions can be estimated from DFT calculations using statistical mechanics within the harmonic approximation, recent studies have shown that adsorbate entropies predicted in this fashion are much smaller than those measured experimentally.<sup>46,47</sup> The problem is partially due to the incorrect treatment of internal rotations, such as those associated with the O–H bonds on bicarbonate and adsorbed H; however, there are indications that surface diffusion also plays an important role.<sup>46</sup> While attempts to estimate the entropies of adsorbed species from gas-phase measurements are promising,<sup>46</sup> the extension of this approach to dissociative reactions awaits further investigation. In the absence of a reliable means of estimating entropic contributions, we focused solely on energetic contributions to reactivity.

The calculations also suggested that bicarbonate, not carbonate, is formed — a distinction that could not be made experimentally. Reaction (4) shows deprotonation of bicarbonate to form carbonate on rutile (110) is endoergic even in a solvated environment. This is similar to the behavior of carbonic acid, H<sub>2</sub>CO<sub>3</sub>, in aqueous solutions. Carbonic acid is a weak acid, with a  $pK_{a1}$  of 3.6. As a result, carbonic acid is essentially fully dissociated to HCO<sub>3</sub><sup>−</sup> in neutral pH solutions. Removal of the second proton to form CO<sub>3</sub><sup>2−</sup> requires more basic solutions, as the  $pK_{a2}$  of H<sub>2</sub>CO<sub>3</sub> is 10.3.

## 4.5 Discussion

The high concentration of bicarbonate on the rutile (110) surface is unexpected, particularly in light of the low concentration of CO<sub>2</sub> in air — a mere 400 ppm. This concentration is orders of

magnitude larger than that dissolved in the nanoscale film of H<sub>2</sub>O on TiO<sub>2</sub>. For comparison, the bicarbonate monolayer has the same number of CO<sub>2</sub> molecules,  $2.5 \times 10^{14} \text{ cm}^{-2}$ , as a film of H<sub>2</sub>O that is 0.3 mm thick! This high density and stable bonding should prompt a re-examination of the molecular mechanism of CO<sub>2</sub> photoreduction on TiO<sub>2</sub>. While the photoreduction of aqueous bicarbonate solutions on metal-promoted TiO<sub>2</sub> has been reported,<sup>48</sup> mechanistic insight from electronic structure calculations is lacking.

The spontaneous formation of bicarbonate monolayers on rutile (110) is also surprising in light of previous studies in UHV.<sup>13,17</sup> At the cryogenic temperatures necessary for co-condensation on rutile (110), CO<sub>2</sub> and H<sub>2</sub>O are unreactive. Heating the co-condensed species to room temperature results in complete desorption of both reactants, not reaction. Our studies suggest this is a kinetic effect. When the coadsorbed molecules are heated, they do not have sufficient time to react prior to desorption. The reaction may also be slowed by the tendency of the more strongly adsorbed H<sub>2</sub>O molecule to segregate at cryogenic temperatures to the rutile (110) surface,<sup>14</sup> blocking reaction by CO<sub>2</sub> at the Ti sites. We note that early experiments using secondary ion mass spectrometry (SIMS) suggested the production of a low density of HCO<sub>3</sub> at defect sites;<sup>17</sup> however, this species was not seen in later experiments<sup>13</sup> and desorbed at a much lower temperature than the HCO<sub>3</sub> reported here.

Spectroscopic indications of bicarbonate production on TiO<sub>2</sub> nanocrystals have been reported;<sup>49,50</sup> however, the infrared-active species appear to be more weakly bound than the adsorbed HCO<sub>3</sub> reported here. The infrared transition assigned to adsorbed bicarbonate on TiO<sub>2</sub> nanocrystals disappears in vacuum environments at room temperature. In contrast, HCO<sub>3</sub> bound to rutile (110) is stable indefinitely at room temperature in UHV, disappearing only with heating to ~500 K. The origins of this discrepancy are not understood, but could be related either to

different binding on different faces and/or polymorphs or uncertainties in spectral assignment. Studies of the “fingerprint” region of the infrared spectrum on well-characterized TiO<sub>2</sub> surfaces are needed for further clarification.

Finally, stoichiometry dictates that the production of a monolayer of bicarbonate must be accompanied by the production of a half-monolayer of H atoms. In addition to affecting the chemistry of TiO<sub>2</sub> surface reactions, these species likely alter the *pH* of the nanoscale H<sub>2</sub>O film in much the same way that carbonic acid produced by dissolved CO<sub>2</sub> affects the *pH* of ambient H<sub>2</sub>O. As a result, a rutile (110) surface terminated by a monolayer of stably bound bicarbonate is expected to have significantly different reactivity than a H<sub>2</sub>O-covered surface.

Our experiments provide no information on the reaction mechanism, and our calculations assumed a reaction between the two most abundant reactants: CO<sub>2</sub> and H<sub>2</sub>O. Recent *ab initio* simulations<sup>51</sup> explored an alternate possibility, namely the reaction of deprotonated H<sub>2</sub>O, OH, bound to an unsaturated Ti site with CO<sub>2</sub> bound to an adjacent unsaturated Ti site, to form adsorbed HCO<sub>3</sub>. This endothermic reaction has a relatively low activation barrier of 0.44 eV in solution. Similar to the reactions studied here, the activation barrier and reaction energy are both stabilized by hydration. This reaction may contribute to the observed HCO<sub>3</sub> production; however, molecular simulations<sup>52,53</sup> of H<sub>2</sub>O bound to unsaturated Ti sites on rutile (110) found a *pK<sub>a</sub>* ~ 9. If so, most of the H<sub>2</sub>O bound to the surface in our experiments was protonated.

The study also investigated a number of other possible reactions between CO<sub>2</sub>, H<sub>2</sub>O, and rutile (110), finding a number of possible reactions with relatively low activation barriers. In all cases, the activation energies and reaction energies were stabilized by hydration. We hope our experimental studies stimulate further computational studies of reaction mechanisms.

## 4.6 Conclusions

Under ambient conditions, rutile (110) is terminated by a near-complete monolayer of  $\text{HCO}_3$  that blocks essentially all of the unsaturated Ti atoms and a half-monolayer of H atoms bound to bridging O atoms. This monolayer forms from the spontaneous reaction of 400 ppm of atmospheric  $\text{CO}_2$  with the nanoscale film of  $\text{H}_2\text{O}$  adsorbed to the rutile (110) surface. This reaction occurs on near-ideal, stoichiometric rutile (110) and does not require surface defects, such as O vacancies, Ti interstitials, or steps. The strong bidentate bonding of the  $\text{HCO}_3$  produces a monolayer that is stable indefinitely in air and vacuum at temperatures below 400 K, but which desorbs at higher temperatures. In contrast, the nanoscale  $\text{H}_2\text{O}$  film that terminates rutile (110) under ambient conditions desorbs rapidly at room temperature.

The presence of a tightly bound monolayer of  $\text{HCO}_3$  that blocks unsaturated Ti sites under ambient conditions is expected to significantly affect chemical reactions on  $\text{TiO}_2$  surfaces. The strong, high density bonding of  $\text{HCO}_3$  and the very weak bonding of adsorbed  $\text{CO}_2$  suggest that  $\text{CO}_2$  photoreduction on  $\text{TiO}_2$  proceeds through the former. These results demonstrate the critical need for studies on well controlled photocatalyst surfaces in ambient and solution environments, where competition for reactive sites plays an important role.

## References

1. W. Chanmanee, M. F. Islam, B. H. Dennis, and F. M. MacDonnell, "Solar Photothermochemical Alkane Reverse Combustion," *Proc. Natl. Acad. Sci. U. S. A.* **113**, 2579 (2016).
2. T. Inoue, A. Fujishima, S. Konishi, and K. Honda, "Photoelectrocatalytic Reduction of Carbon Dioxide in Aqueous Suspensions of Semiconductor Powders," *Nature* **277**, 637 (1979).

3. J. L. White, M. F. Baruch, J. E. Pander III, Y. Hu, I. C. Fortmeyer, J. E. Park, T. Zhang, K. Liao, J. Gu, and Y. Yan, "Light-Driven Heterogeneous Reduction of Carbon Dioxide: Photocatalysts and Photoelectrodes," *Chem. Rev.* **115**, 12888 (2015).
4. G. Centi and S. Perathoner, "Opportunities and Prospects in the Chemical Recycling of Carbon Dioxide to Fuels," *Catal. Today* **148**, 191 (2009).
5. C.-T. Yang, B. C. Wood, V. R. Bhethanabotla, and B. Joseph, "CO<sub>2</sub> Adsorption on Anatase TiO<sub>2</sub> (101) Surfaces in the Presence of Subnanometer Ag/Pt Clusters: Implications for CO<sub>2</sub> Photoreduction," *J. Phys. Chem. C* **118**, 26236 (2014).
6. M. A. Henderson, "A Surface Science Perspective on Photocatalysis," *Surf. Sci. Rep.* **66**, 185 (2011).
7. H.-J. Freund and M. W. Roberts, "Surface Chemistry of Carbon Dioxide," *Surf. Sci. Rep.* **25**, 225 (1996).
8. S. Nakamura, M. Hatakeyama, Y. Wang, K. Ogata, and K. Fujii, "Advances in CO<sub>2</sub> Capture, Sequestration, and Conversion," F. Jin, L.-N. He, and Y. H. Hu, Eds; ACS Symposium Series: Washington, DC, 123 (2015).
9. N. M. Dimitrijevic, B. K. Vijayan, O. G. Poluektov, T. Rajh, K. A. Gray, H. He, and P. Zapol, "Role of Water and Carbonates in Photocatalytic Transformation of CO<sub>2</sub> to CH<sub>4</sub> on Titania," *J. Am. Chem. Soc.* **133**, 3964 (2011).
10. J. Lee, D. C. Sorescu, and X. Deng, "Electron-Induced Dissociation of CO<sub>2</sub> on TiO<sub>2</sub>(110)," *J. Am. Chem. Soc.* **133**, 10066 (2011).
11. D. Acharya, N. Camillone III, and P. Sutter, "CO<sub>2</sub> Adsorption, Diffusion, and Electron-Induced Chemistry on Rutile TiO<sub>2</sub> (110): A Low-Temperature Scanning Tunneling Microscopy Study," *J. Phys. Chem. C* **115**, 12095 (2011).

12. S. Tan, Y. Zhao, J. Zhao, Z. Wang, C. Ma, A. Zhao, B. Wang, Y. Luo, J. Yang, and J. Hou, "CO<sub>2</sub> Dissociation Activated through Electron Attachment on the Reduced Rutile TiO<sub>2</sub> (110)-1×1 Surface," *Phys. Rev. B* **84**, 155418 (2011).
13. X. Lin, Y. Yoon, N. G. Petrik, Z. Li, Z.-T. Wang, V.-A. Glezakou, B. D. Kay, I. Lyubinetzky, G. A. Kimmel, and R. Rousseau, "Structure and Dynamics of CO<sub>2</sub> on Rutile TiO<sub>2</sub> (110)-1×1," *J. Phys. Chem. C* **116**, 26322 (2012).
14. R. S. Smith, Z. Li, L. Chen, Z. Dohnálek, and B. D. Kay, "Adsorption, Desorption, and Displacement Kinetics of H<sub>2</sub>O and CO<sub>2</sub> on TiO<sub>2</sub> (110)," *J. Phys. Chem. B* **118**, 8054 (2014).
15. V. P. Indrakanti, H. H. Schobert, and J. D. Kubicki, "Quantum Mechanical Modeling of CO<sub>2</sub> Interactions with Irradiated Stoichiometric and Oxygen-Deficient Anatase TiO<sub>2</sub> Surfaces: Implications for the Photocatalytic Reduction of CO<sub>2</sub>," *Energy Fuels* **23**, 5247 (2009).
16. E. Lira, J. Ø. Hansen, P. Huo, R. Bechstein, P. Galliker, E. Lægsgaard, B. Hammer, S. Wendt, and F. Besenbacher, "Dissociative and Molecular Oxygen Chemisorption Channels on Reduced Rutile TiO<sub>2</sub> (110): An STM and TPD Study," *Surf. Sci.* **604**, 1945 (2010).
17. M. A. Henderson, "Evidence for Bicarbonate Formation on Vacuum Annealed TiO<sub>2</sub> (110) Resulting from a Precursor-Mediated Interaction between CO<sub>2</sub> and H<sub>2</sub>O," *Surf. Sci.* **400**, 203 (1998).
18. M. B. Hugenschmidt, L. Gamble, and C. T. Campbell, "The Interaction of H<sub>2</sub>O with a TiO<sub>2</sub> (110) Surface," *Surf. Sci.* **302**, 329 (1994).
19. S. Wendt, J. Matthiesen, R. Schaub, E. K. Vestergaard, E. Lægsgaard, F. Besenbacher, and B. Hammer, "Formation and Splitting of Paired Hydroxyl Groups on Reduced TiO<sub>2</sub> (110)," *Phys. Rev. Lett.* **96**, 066107 (2006).

20. G. Ketteler, S. Yamamoto, H. Bluhm, K. Andersson, D. E. Starr, D. F. Ogletree, H. Ogasawara, A. Nilsson, and M. Salmeron, "The Nature of Water Nucleation Sites on TiO<sub>2</sub> (110) Surfaces Revealed by Ambient Pressure X-Ray Photoelectron Spectroscopy," *J. Phys. Chem. C* **111**, 8278 (2007).
21. P. M. Kowalski, B. Meyer, and D. Marx, "Composition, Structure, and Stability of the Rutile TiO<sub>2</sub> (110) Surface: Oxygen Depletion, Hydroxylation, Hydrogen Migration, and Water Adsorption," *Phys. Rev. B* **79**, 115410 (2009).
22. L.-M. Liu, C. Zhang, G. Thornton, and A. Michaelides, "Structure and Dynamics of Liquid Water on Rutile TiO<sub>2</sub> (110)," *Phys. Rev. B* **82**, 161415 (2010).
23. A. Song, D. Jing, and M. A. Hines, "Rutile Surface Reactivity Provides Insight into the Structure-Directing Role of Peroxide in TiO<sub>2</sub> Polymorph Control," *J. Phys. Chem. C* **118**, 27343 (2014).
24. M. Greiner and P. Kruse, "Recrystallization of Tungsten Wire for Fabrication of Sharp and Stable Nanoprobe and Field-Emitter Tips," *Rev. Sci. Instrum.* **78**, 026104 (2007).
25. S. W. Schmucker, N. Kumar, J. R. Abelson, S. R. Daly, G. S. Girolami, M. R. Bischof, D. L. Jaeger, R. F. Reidy, B. P. Gorman, and J. Alexander, "Field-Directed Sputter Sharpening for Tailored Probe Materials and Atomic-Scale Lithography," *Nat. Commun.* **3**, 935 (2012).
26. U. Diebold and T. Madey, "TiO<sub>2</sub> by XPS," *Surf. Sci. Spectra* **4**, 227 (1996).
27. U. Diebold, "The Surface Science of Titanium Dioxide," *Surf. Sci. Rep.* **48**, 53 (2003).
28. W. Kohn and L. J. Sham, "Self-Consistent Equations Including Exchange and Correlation Effects," *Phys. Rev.* **140**, A1133 (1965).
29. J. P. Perdew, K. Burke, and M. Ernzerhof, "Generalized Gradient Approximation Made Simple," *Phys. Rev. Lett.* **77**, 3865 (1996).

30. G. Kresse and J. Hafner, “*Ab Initio* Molecular Dynamics for Liquid Metals,” *Phys. Rev. B* **47**, 558 (1993).
31. G. Kresse and J. Hafner, “*Ab Initio* Molecular-Dynamics Simulation of the Liquid-Metal–Amorphous-Semiconductor Transition in Germanium,” *Phys. Rev. B* **49**, 14251 (1994).
32. G. Kresse and J. Furthmüller, “Efficiency of *Ab-Initio* Total Energy Calculations for Metals and Semiconductors Using a Plane-Wave Basis Set,” *Comput. Mater. Sci.* **6**, 15 (1996).
33. G. Kresse and J. Furthmüller, “Efficient Iterative Schemes for *Ab Initio* Total-Energy Calculations Using a Plane-Wave Basis Set,” *Phys. Rev. B* **54**, 11169 (1996).
34. S. Grimme, J. Antony, S. Ehrlich, and H. Krieg, “A Consistent and Accurate *Ab Initio* Parametrization of Density Functional Dispersion Correction (DFT-D) for the 94 Elements H–Pu,” *J. Chem. Phys.* **132**, 154104 (2010).
35. P. E. Blöchl, “Projector Augmented-Wave Method,” *Phys. Rev. B* **50**, 17953 (1994).
36. G. Kresse and D. Joubert, “From Ultrasoft Pseudopotentials to the Projector Augmented-Wave Method,” *Phys. Rev. B* **59**, 1758 (1999).
37. K. Mathew, R. Sundararaman, K. Letchworth-Weaver, T. Arias, and R. G. Hennig, “Implicit Solvation Model for Density-Functional Study of Nanocrystal Surfaces and Reaction Pathways,” *J. Chem. Phys.* **140**, 084106 (2014).
38. J. Tersoff and D. Hamann, “Theory of the Scanning Tunneling Microscope,” *Phys. Rev. B: Condens. Matter Mater. Phys.* **31**, 805 (1985).
39. S. Yamamoto, H. Bluhm, K. Andersson, G. Ketteler, H. Ogasawara, M. Salmeron, and A. Nilsson, “In Situ X-Ray Photoelectron Spectroscopy Studies of Water on Metals and Oxides at Ambient Conditions,” *J. Phys.: Condens. Matter* **20**, 184025 (2008).

40. M. A. Henderson, "An HREELS and TPD Study of Water on TiO<sub>2</sub> (110): The Extent of Molecular Versus Dissociative Adsorption," *Surf. Sci.* **355**, 151 (1996).
41. G. A. Kimmel, M. Baer, N. G. Petrik, J. VandeVondele, R. Rousseau, and C. J. Mundy, "Polarization- and Azimuth-Resolved Infrared Spectroscopy of Water on TiO<sub>2</sub> (110): Anisotropy and the Hydrogen-Bonding Network," *J. Phys. Chem. Lett.* **3**, 778 (2012).
42. S. Wendt, P. T. Sprunger, E. Lira, G. K. Madsen, Z. Li, J. Ø. Hansen, J. Matthiesen, A. Blekinge-Rasmussen, E. Lægsgaard, and B. Hammer, "The Role of Interstitial Sites in the Ti<sub>3d</sub> Defect State in the Band Gap of Titania," *Science* **320**, 1755 (2008).
43. S. C. Jensen and C. M. Friend, "The Dynamic Roles of Interstitial and Surface Defects on Oxidation and Reduction Reactions on Titania," *Top. Catal.* **56**, 1377 (2013).
44. T. L. Barr and S. Seal, "Nature of the Use of Adventitious Carbon as a Binding Energy Standard," *J. Vac. Sci. Technol A* **13**, 1239 (1995).
45. D. C. Sorescu, J. Lee, W. A. Al-Saidi, and K. D. Jordan, "Coadsorption Properties of CO<sub>2</sub> and H<sub>2</sub>O on TiO<sub>2</sub> Rutile (110): A Dispersion-Corrected DFT Study," *J. Chem. Phys.* **137**, 074704 (2012).
46. C. T. Campbell and J. R. Sellers, "The Entropies of Adsorbed Molecules," *J. Am. Chem. Soc.* **134**, 18109 (2012).
47. C. T. Campbell and J. R. Sellers, "Enthalpies and Entropies of Adsorption on Well-Defined Oxide Surfaces: Experimental Measurements," *Chem. Rev.* **113**, 4106 (2013).
48. Z. Goren, I. Willner, A. Nelson, and A. Frank, "Selective Photoreduction of Carbon Dioxide/Bicarbonate to Formate by Aqueous Suspensions and Colloids of Palladium-Titania," *J. Phys. Chem.* **94**, 3784 (1990).

49. K. Tanaka and J. White, "Characterization of Species Adsorbed on Oxidized and Reduced Anatase," *J. Phys. Chem* **86**, 4708 (1982).
50. J. Baltrusaitis, J. Schuttlefield, E. Zeitler, and V. H. Grassian, "Carbon Dioxide Adsorption on Oxide Nanoparticle Surfaces," *Chem. Eng. J.* **170**, 471 (2011).
51. W.-J. Yin, M. Krack, B. Wen, S.-Y. Ma, and L.-M. Liu, "CO<sub>2</sub> Capture and Conversion on Rutile TiO<sub>2</sub> (110) in the Water Environment: Insight by First-Principles Calculations," *J. Phys. Chem. Lett.* **6**, 2538 (2015).
52. K. Bourikas, T. Hiemstra, and W. Van Riemsdijk, "Ion Pair Formation and Primary Charging Behavior of Titanium Oxide (Anatase and Rutile)," *Langmuir* **17**, 749 (2001).
53. J. Cheng and M. Sprik, "Acidity of the Aqueous Rutile TiO<sub>2</sub> (110) Surface from Density Functional Theory Based Molecular Dynamics," *J. Chem. Theory Comput.* **6**, 880 (2010).

## Chapter 5

### Solution-based Preparation of Benzoate Monolayers on Rutile (110)

#### 5.1 Introduction

The functionalization of surfaces by self-assembled monolayers is of significant importance. The monolayers can tailor the chemical or physical properties of substrate surfaces or block unwanted defects. As an example of the first, dye molecules adsorbed on  $\text{TiO}_2$  act as light collectors in dye-sensitized solar cells (DSSC).<sup>1-2</sup> As an example of the second, a monolayer of H atoms passivates the vast majority of electronically active defects on Si.<sup>3-4</sup> Therefore, investigations on monolayers could provide insights into understanding, controlling, and improving surface functionality.

One application of monolayers on  $\text{TiO}_2$  surfaces is DSSCs. Dyes can be made photoactive from the UV to the visible/near-infrared region,<sup>1-2,5</sup> whereas bare  $\text{TiO}_2$  only absorbs UV light.<sup>6</sup> If dyes are tethered to  $\text{TiO}_2$ , photoinduced electrons in the dye can be injected into the conduction band of  $\text{TiO}_2$ , while the corresponding holes are transferred to redox electrolytes.<sup>7</sup> This separation of charge carriers leads to a high carrier lifetime. In DSSCs dye molecules need to be tightly bound to the  $\text{TiO}_2$  surface to ensure efficient electron injection into the electrode. The stability of dye molecules is a key to the long-term stability of DSSCs,<sup>8-10</sup> which necessitates understanding the mechanisms and conditions of dye photodegradation reactions. The dye molecules used in the DSSCs are usually transition-metal-based complex compounds, such as the Ru-based dye N3<sup>7</sup> and the Zn-based dye Zn-1b.<sup>11</sup> These dye molecules are anchored to  $\text{TiO}_2$  surfaces through the carboxylates of isonicotinic acid or benzoic acid groups.<sup>11-13</sup> Therefore, the adsorption and reactivity of benzoic acid, as a small molecule analogue of the dyes, on  $\text{TiO}_2$  surfaces is important for understanding and improving DSSCs.

In this dissertation, a new solution-based technique to form well-ordered, high-quality benzoate monolayers on atomically flat rutile (110) surfaces was developed. The benzoic acid molecules adsorb to the surface dissociatively, producing protons and bidentate benzoates bound to the five-fold coordinated Ti sites, which will be referred to as  $Ti_{5c}$  sites. This method contrasts to previous studies in which benzoic acid was evaporated onto rutile crystals that had been sputtered and annealed in vacuum for many cycles.<sup>14-15</sup> This sputtering and annealing process produces many surface and subsurface defects, including  $Ti^{3+}$  interstitials and O vacancies.<sup>16</sup>

This self-assembled benzoate monolayer displayed pairing of benzoate molecules, consistent with some previous studies,<sup>15,17</sup> where this type of pairing was interpreted as “dimerization”. Williams *et al*<sup>15</sup> proposed a “T”-shaped dimer to explain the pairing of benzoate molecules in which alternating phenyl rings rotated by  $90^\circ$  from the [001] orientation. In contrast, some other studies<sup>14,18</sup> did not observe the pairing on the surface. Calculations done by Zhao and Bowler did not find a stable dimer configuration.<sup>19</sup> Therefore, the existence and structure of the paired monolayer remained controversial.

In this dissertation, Monte Carlo simulations and DFT calculations explain the apparent pairing of benzoate molecules. The phenyl rings adopt an edge-to-face tetrameric geometry with their four nearest neighbors, as a result of the  $\pi$ - $\pi$  intermolecular interactions which include quadrupole-quadrupole interactions and dispersion forces. Adjacent molecules tilt towards each other across Ti atom rows, leading to the formation of the apparent pairing in STM images and further stabilization of the monolayer. The energy gained from the pairing is comparable to thermal energy; therefore, both paired and unpaired regions exist in the monolayer. Similar configurations have been previously observed in other organic monolayers. For example,

pentacene displays a herringbone structure on amorphous silicon oxide surfaces.<sup>20</sup> The monolayer is stabilized by the herringbone structure and exhibits high charge-carrier mobilities.

## **5.2 Experimental and Computational**

### **5.2.1 Experimental methods**

Single-side polished rutile (110) samples (float zone or Verneuil) used for STM and XPS analyses were first annealed at 700°C for 10 min to introduce conductivity. Double-side polished rutile samples (Verneuil) used for multiple-internal-reflection (MIR) infrared analysis were beveled at 45°. Rutile crystals were etched by a 1:1:2 solution by volume of 28% NH<sub>4</sub>OH (aq, BDG, ACS grade): 30% H<sub>2</sub>O<sub>2</sub> (aq, J.T. Baker, CMOS grade): ultrapure H<sub>2</sub>O (Milli-Q) at 80°C for 10 min and then rinsed by ultrapure water. This process produced atomically clean and flat rutile (110) surfaces terminated by a bicarbonate monolayer.<sup>21-22</sup> This hydrophilic surface was used as the reference for all infrared spectra. After etching, rutile crystals were immersed in 0.16 M aqueous benzoic acid (Sigma, >99%) solutions for 10 min at either room temperature or boiling temperature. The sample was hydrophobic after removal from the benzoic acid solution; it became hydrophilic again after immersion in water for as little as 5 sec.

After removal from the benzoic acid solution, the sample was introduced into an ultrahigh vacuum (UHV) chamber with a base pressure of  $1 \times 10^{-10}$  mBar for STM and XPS analysis. The chamber was equipped with an Omicron STM (VT STM XA/QPlus), an unmonochromated x-ray source, and an Omicron Sphera II photoelectron analyzer. The rutile surface was imaged with an electrochemically prepared tungsten tip using a bias of 1.5-2.0 V and a tunneling current of 300-500 pA. Tip preparation was described in Chapter 2. Photoelectrons were generated by unmonochromated Mg K $\alpha$  x-rays and were collected at the takeoff angles of 0° and 45°. Either a Shirley or a Tougaard baseline was subtracted from all spectra. Small energy corrections

(~0.05 eV) were applied to all spectra using published reference energies<sup>23</sup> to offset mild band bending.<sup>24</sup> The Ti 2*p* and C 1*s* spectra were normalized to the maximum amplitude of the Ti 2*p*<sub>3/2</sub> transition, whereas the O 1*s* spectra were normalized to the maximum amplitude of the O 1*s* transition.

Double-side polished rutile (110) crystals were introduced into an infrared spectrometer (Nicolet 670) purged by dry air. Polarized infrared spectra were taken in the multiple-internal-reflection (MIR) geometry. An MCT-A detector and a ZnSe grid polarizer (Molelectron) were used in the spectrometer.

### 5.2.2 Quantification of monolayer coverage from XPS spectra

The fractional coverage of the benzoate monolayer,  $\phi$ , was calculated from the integrated areas of Ti 2*p*<sub>3/2</sub> and C 1*s* transitions using the benzoate monolayer geometry and the Beer-Lambert law. The benzoate monolayer was modeled as a uniform layer of C atoms with a density 20% of that in graphite. As a result, it was assumed that the photoelectron mean free path in the benzoate monolayer was 5 times larger than that in graphite. The effective thickness of the benzoate monolayer was 0.5 nm. The relative areas of the Ti 2*p*<sub>3/2</sub> and C 1*s* transitions were therefore given by

$$\frac{I_C}{I_{Ti}} = \frac{0.2\Gamma_C}{1/3\Gamma_{Ti}} \frac{\phi \int_0^a e^{-x/5\lambda_C \cos\theta} dx}{\int_0^\infty e^{-a/5\lambda_{Ti} \cos\theta} e^{-x/\lambda_{Ti} \cos\theta} dx}, \quad (1)$$

where  $a$  was 0.5 nm,  $\theta$  was the angle between the emitted photoelectrons and the surface normal,  $\Gamma_C$  and  $\Gamma_{Ti}$  were the photoemission cross-sections of C and Ti atoms, respectively, and  $\lambda_C$  and  $\lambda_{Ti}$  were the mean free paths of C and Ti photoelectrons, respectively. The factor of 1/3 in the denominator accounted for the stoichiometry of Ti in TiO<sub>2</sub>. Since the mean free path in the

monolayer was much larger than the thickness, the integrals could be expanded to first order yielding

$$\frac{I_C}{I_{Ti}} = 0.6 \frac{\Gamma_C}{\Gamma_{Ti}} \frac{\phi a}{e^{-a/5\lambda_{Ti}\cos\theta} \lambda_{Ti} \cos\theta}. \quad (2)$$

Similarly, the relative intensities of photoelectrons coming from bulk graphite and Ti samples were

$$\frac{I_C^\infty}{I_{Ti}^\infty} = \frac{\Gamma_C \int_0^\infty e^{-x/\lambda_C \cos\theta} dx}{\Gamma_{Ti} \int_0^\infty e^{-x/\lambda_{Ti} \cos\theta} dx} = \frac{\Gamma_C \lambda_C}{\Gamma_{Ti} \lambda_{Ti}} = \frac{RSF_C}{RSF_{Ti}}. \quad (3)$$

The  $RSF_C$  and  $RSF_{Ti}$  were the atomic sensitivity factors of C and Ti, respectively, measured by Wagner.<sup>25</sup> Therefore, the fractional coverage of the benzoate monolayer  $\phi$  could be estimated using

$$\phi = 1.7 \frac{RSF_{Ti}}{RSF_C} e^{-a/5\lambda_{Ti}\cos\theta} \lambda_C \cos\theta \frac{I_C}{I_{Ti}} = 13e^{-0.079/\cos\theta} \cos\theta \frac{I_C}{I_{Ti}}. \quad (4)$$

The mean free paths of Ti and C photoelectrons,  $\lambda_{Ti}=1.27$  nm and  $\lambda_C=1.54$  nm, were interpolated from Fuentes' work.<sup>26</sup> From equation (4), the benzoate monolayer coverage could be calculated using the integrated areas of Ti  $2p_{3/2}$  and C  $1s$  transitions and the takeoff angle.

### 5.2.3 Computational methods

Monte Carlo simulations were performed using the Metropolis algorithm<sup>27-28</sup> on a  $64 \times 64$  site lattice with periodic boundary conditions. The lattice contained 4096  $Ti_{5c}$  sites. Four reactions were included: adsorption from the solution onto the surface, desorption into the solution from the surface, diffusion along the Ti atom rows, rotation of the phenyl rings by  $90^\circ$  around the carboxylate groups, and tristate tilting (left, center, and right) of the molecules. The adsorption energy of site  $(i, j)$  was assumed to be

$$E_a(i, j) = E_0 + \sum_{i \pm 1, j \pm 1} E_{int}(i, j; i', j') ,$$

where  $E_0$  is a constant and  $E_{int}$  represents the intermolecular energies between the molecule at site  $(i, j)$  and its nearest neighbors. The intermolecular interactions were assumed to be dominated by the interactions between the phenyl rings. These distance- and orientation-dependent interactions were extracted from *ab initio* calculations of benzene dimers performed at the MP2/6-31G\* level.<sup>29</sup> The relative magnitudes of  $E_0$  and adsorption frequency were adjusted to generate a low density of benzoate vacancies at the simulated temperatures to be consistent with experiments.

Density functional theory (DFT) was used to model the structure of the benzoate monolayer on  $4 \times 2$  periodically repeating slabs consisting of 5 TiO<sub>2</sub> trilayers separated by a 12.5 Å vacuum spacing with autocompensated surfaces.<sup>16</sup> This supercell contained 8 Ti<sub>5c</sub> atoms capable of adsorbing 4 benzoate molecules at saturation. During optimization, the positions of the bottommost TiO<sub>2</sub> layer and its terminating bridging O rows were held fixed. Calculations were performed using DFT within the generalized gradient approximation (GGA)<sup>30</sup> with the Perdew, Burke, and Ernzerhof (PBE) exchange-correlation functional, as implemented in the Vienna *ab initio* simulation package (VASP).<sup>31-34</sup> The functional was corrected for long-range dispersion interactions using the zero damping DFT-D3 method.<sup>35</sup> Electron-ion interactions were described using the projector augmented wave (PAW) method.<sup>36-37</sup> Electronic states were expanded in plane waves with a kinetic energy cutoff of 400 eV and a  $2 \times 2 \times 1$  Monkhorst-Pack grid of  $k$  points. Brillouin-zone integration was performed using Gaussian smearing. Vibrational modes were calculated using density functional perturbation theory (DFPT) without dispersion interactions on a supercell containing two TiO<sub>2</sub> trilayers. For the DFPT calculations, a thinner slab was used, and the Ti and O atoms at the bottom of the slabs were terminated with

pseudohydrogen atoms with nuclear charges of  $+4/3$  and  $+2/3$  to simulate a bulklike environment.<sup>38-39</sup> The atoms were held at the equilibrium geometry obtained from the calculations on the 5-trilayer-thick slabs. Reported vibrational energies are adjusted by a constant scaling factor (0.983) to correct for systematic errors.

## 5.3 Results

### 5.3.1 STM

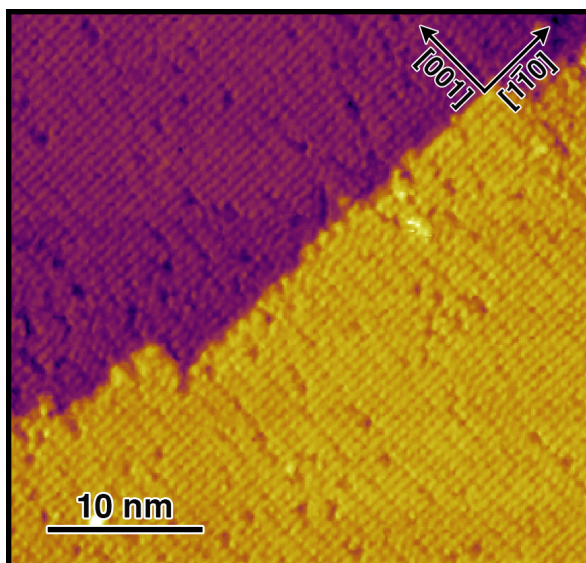


Figure 5.1 STM image of benzoate monolayer on the rutile (110) surface prepared from benzoic acid solution.

STM images, as shown in Fig. 5.1 and Fig. 5.2, revealed the formation of near-ideal benzoate monolayers after rutile (110) was immersed in benzoic acid solutions. The STM images showed regions of paired molecules, regions of unpaired molecules, and a few different types of defects. Fig. 5.2(a) displays a region covered by paired molecules. The distance between the bright protrusions along  $[001]$  is 0.60 nm, which is twice the Ti atom spacing. The distance between the paired molecules along  $[1\bar{1}0]$  is 0.42 nm, less than the 0.65 nm spacing between neighboring Ti rows. Fig. 5.2(b) shows paired regions and unpaired regions. The paired regions are identified by

the interstices between pairs. Some molecules are missing in this image. Time-dependent imaging showed little change of the paired and unpaired regions over a period of hours. Motion of molecules near defects was observed. Some regions of the monolayer showed different ordering, such as in Fig. 5.2 (c) where many staggered dimers were observed. While the monolayer was predominantly composed of paired molecules, triplets appeared in some regions of the surface as shown in Fig. 5.2(d).

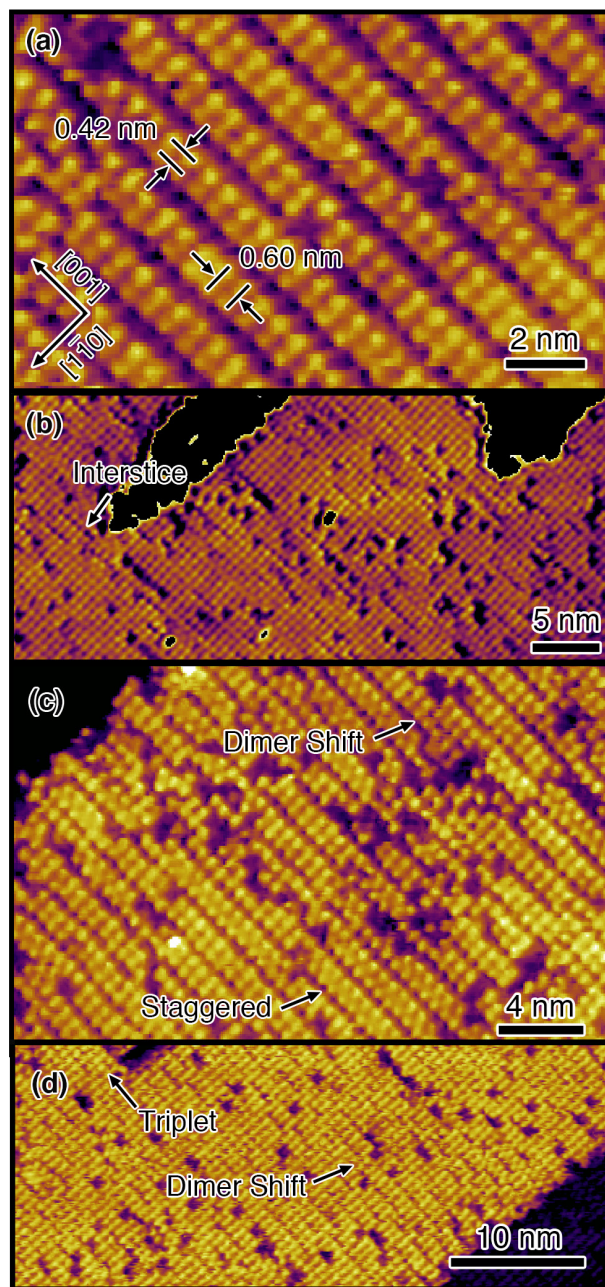


Figure 5.2 High-resolution STM images of benzoate monolayers on rutile (110) surfaces. (a) Region of near-perfect pairing. (b) Region in which both paired and unpaired molecules exist. Pairing leads to characteristic interstices between pairs. (c) Disordered region, displaying a number of

defects including dimer shifts and staggered dimers. (d) Region displaying triplets and dimer shifts.

### 5.3.2 Infrared spectroscopy

Polarized infrared spectroscopy provided information about the orientation of the adsorbates. Polarized spectra were obtained from the rutile samples in the MIR geometry with light propagating along and across the Ti rows (*i.e.*, along the [001] and  $[1\bar{1}0]$  directions, respectively). The C-H stretching region of the spectra is shown in Fig. 5.3. Only aromatic C-H stretching modes were observed. There was no absorption corresponding to the asymmetric methylene stretching mode ( $\sim 2920\text{ cm}^{-1}$ ), indicating the absence of carbonaceous contamination.

The polarized MIR spectra ruled out many previously proposed benzoate dimer structures. First, the C-H stretch modes appeared in both *s*-polarized spectra, which eliminated all face-to-face parallel configurations. If the phenyl rings were all parallel to the [001] or  $[1\bar{1}0]$  direction, there would not be any absorbance in the *s*-polarized spectra with light propagating along [001] or  $[1\bar{1}0]$ , respectively. Second, the configurations with equal numbers of phenyl rings parallel and perpendicular to the Ti rows were ruled out, as spectra taken in orthogonal propagation orientations were significantly different.

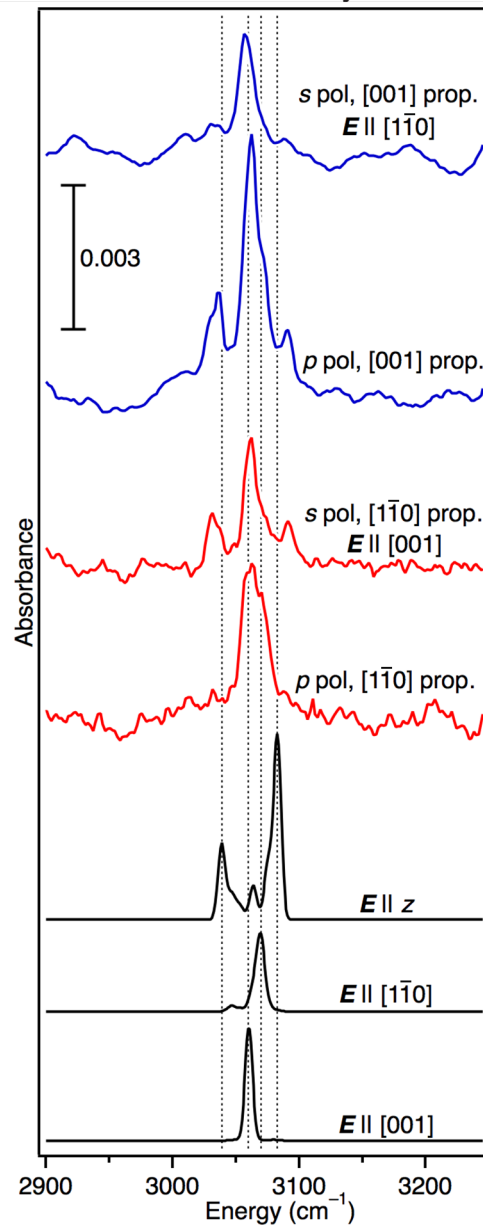
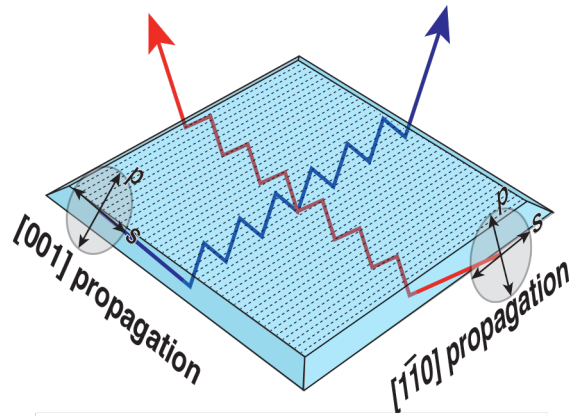


Figure 5.3 Experimental (blue and red) and calculated (black) infrared spectra of benzoate monolayer taken with different light propagation directions and polarizations as indicated. The dotted lines on the sketched crystal represent the Ti atom rows. Two crystals were used instead of the single crystal sketched. The calculated frequencies of C-H stretching modes are indicated by vertical lines. The Gaussian linewidth and absorbance scale factor for the calculated spectra were chosen to match the experiment.

### 5.3.3 XPS analysis

The chemical composition of the benzoate monolayer was analyzed with x-ray photoelectron spectroscopy. High-resolution spectra of the Ti  $2p$  region, shown in Fig. 5.4(a), consisted of two  $Ti^{4+}$  transitions. The transition at 459.3 eV corresponded to the Ti  $2p_{3/2}$  transition, and the transition at 460.5 eV corresponded to the Ti  $2p_{1/2}$  transition. The absence of corresponding transitions at  $\sim 2$  eV lower energy was significant, indicating a very low surface  $Ti^{3+}$  density. As expected, the  $Ti^{3+}$  density was still low even after desorption of the benzoate monolayer by heating, because surface  $Ti^{3+}$  defects on solution-prepared samples would be rapidly oxidized in solutions. In contrast, the density of surface  $Ti^{3+}$  defects increased after desorption of the benzoate monolayer when a sputtered and annealed rutile sample was used as shown in the inset of Fig. 5.4(a). The increase of surface  $Ti^{3+}$  defects could be explained by the reversible charge donation from the defects to the monolayer.

The C  $1s$  region, as shown in Fig. 5.4(b), showed two types of C atoms: C atoms in carboxylate groups at 289.2 eV and C atoms in phenyl rings at 285.5 eV. When heated to elevated temperatures, benzoate molecules desorbed from the rutile surface as evidenced by the

decrease of intensities at both transitions. In the heating process, some of the C became graphitic as evidenced by the shift to higher energy (284.8 eV).

High-resolution spectra of the O 1s region demonstrated a primary transition at 530.4 eV, which was assigned to the O in bulk rutile, and a secondary transition at 531.9 eV. The secondary transition corresponded to O in carboxylate groups. Similar to the C 1s transitions, the 531.9 eV transition decreased when the benzoate molecules desorbed with heating.

The monolayer coverage decreased when the sample was heated. The coverage calculated from the XPS data collected at two angles is plotted in the inset of Fig. 5.4(b). The sample was initially covered with almost a full monolayer of benzoate molecules. After annealing, about 75% of the monolayer desorbed. The rest became graphitic C and remained on the surface.

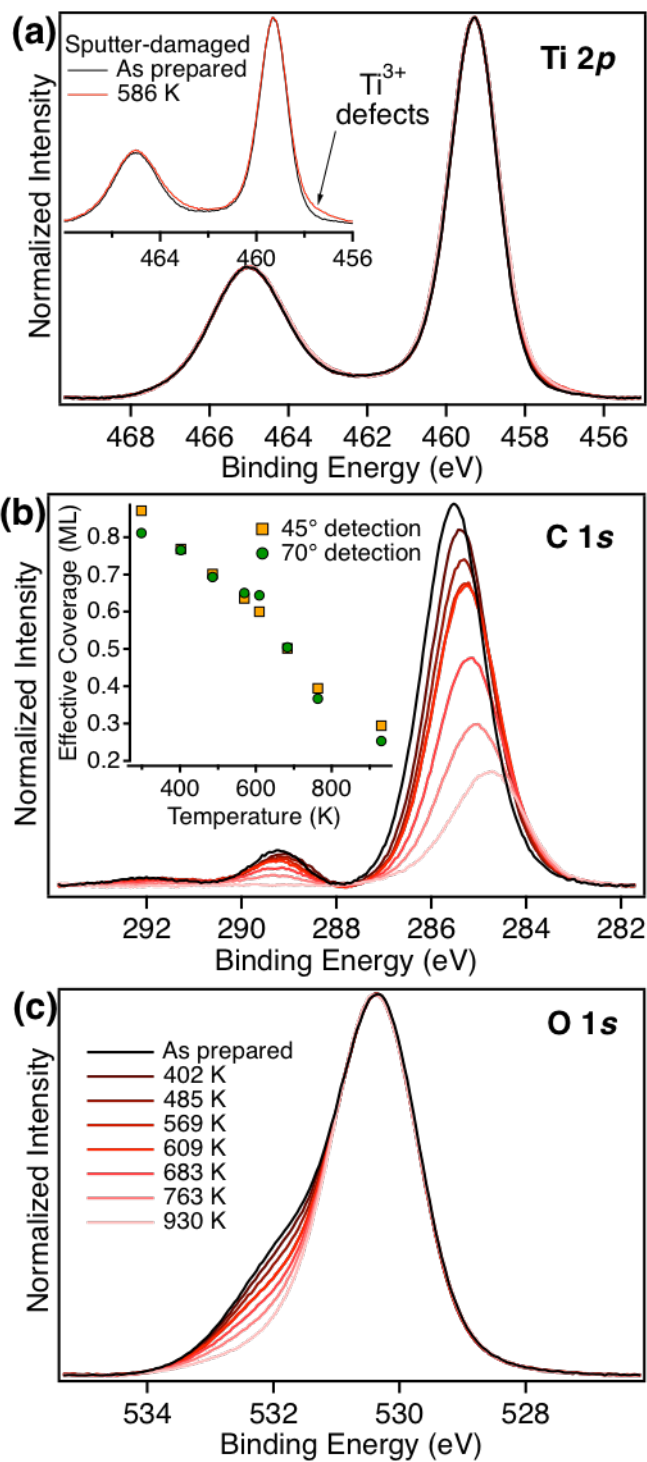


Figure 5.4 High-resolution XPS of the (a) Ti 2*p*, (b) C 1*s*, and (c) O 1*s* regions of benzoate monolayers on rutile (110) as a function of annealing temperature (20 min duration). Photoelectrons were collected at 70° from

the surface normal. The inset in (a) shows the XPS spectra of a benzoate monolayer prepared from a sputtered and annealed initial surface with the takeoff angle of 45°. The inset in (b) shows the calculated coverage of benzoate monolayers at different temperatures with the takeoff angles of 45° and 70°, respectively. One monolayer corresponded to 7 C atoms per 2 Ti<sub>5c</sub> sites.

### 5.3.4 Monte Carlo Simulations

The interactions between benzoates lead to a long-range order that strains the use of DFT calculations. Therefore, MC simulations were performed to explore possible geometries and guide DFT calculations.

In the MC simulations it was assumed that the intermolecular interactions within the benzoate monolayer are dominated by the  $\pi$ - $\pi$  interactions between the phenyl rings. The interaction energies between phenyl rings were approximated by the calculated intermolecular potentials between benzene dimers as shown in Fig. 5.5(a).<sup>29</sup> Benzene has a quadrupole moment due to the negative charge of  $\pi$  electrons above and below the phenyl plane and the positive charge surrounding the periphery. The  $\pi$ - $\pi$  interactions between phenyl rings were principally due to the quadrupole-quadrupole interactions, dispersion forces, and Pauli repulsion.<sup>40-41</sup> For simplicity, the benzoate molecules are represented by quadrupoles in Fig. 5.5(b).

At the center-to-center distances appropriate to the along-row and across-row orientations, the interactions between molecules in an edge-to-face or "T" geometry are much stronger than those in a face-to-face or "parallel" geometry as shown in Fig. 5.5(a).

If the phenyl rings are allowed to rotate by 90° in the MC simulations, the benzoate molecules predominantly adopt an edge-to-face configuration with its four nearest neighbors, leading to the

formation of tetramers as shown in Fig. 5.6(a). This structure is consistent with the conclusion obtained from the IR spectra that the phenyl rings cannot be all parallel along one orientation; however, the tetramer configuration does not explain the observed paired monolayer. The tetramer model is not adequate to describe the system. Something more needed to be included in the model.

The tetramer model did not include the freedom of tilting about the two Ti-O bonds. Due to the long transition arm of the phenyl rings, a small tilting would result in a significant decrease of the intermolecular distance across the Ti rows. For example, if the benzoates tilt towards each other by  $7^\circ$  (*vide infra*), the distance between the centers of phenyl rings would decrease by 1 Å.

If the phenyl rings were allowed to tilt across the Ti rows in the MC simulations, a temperature-dependent, paired tetramer configuration was found. At low temperatures benzoates tilted towards each other, leading to the formation of well-ordered, paired tetramers as shown in Fig. 5.6(b). “Dimer shifts”, similar to the defects in Fig. 5.2(c), were also observed in the simulations. The pairing in STM images is, thus, a result of this paired tetramer configuration instead of the previously proposed “dimer” configuration. In the case of benzoate monolayers at elevated temperature, as shown in Fig. 5.6 (c), some regions are paired, and others are not paired. In the unpaired regions, some molecules are paired, and some are not. The unpairing transition has long-range order due to the coupling of molecules along the Ti atom rows. When one pair of benzoate molecules in the paired region dissociates, the energy of the monolayer increases because the distance between the two unpaired molecules across the Ti rows and the distance of the unpaired molecules with their four nearest neighbors along the Ti rows are both increased. After the first pair dissociates, less energy is needed for the dissociation of the adjacent pairs since the energy gain and loss from nearest-neighbor interactions cancel out.

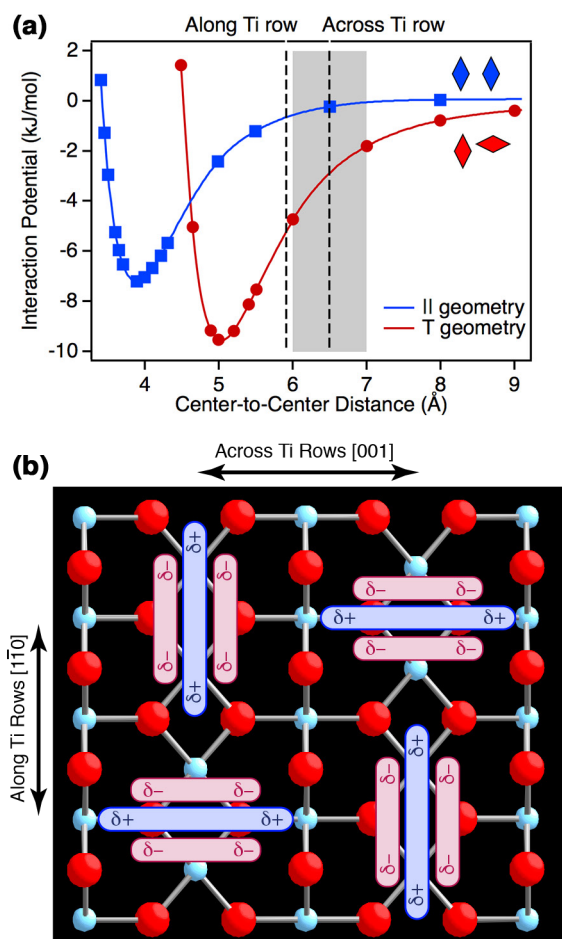


Figure 5.5 (a) Intermolecular potential of benzene dimers as a function of the center-to-center distance for the parallel configuration and T-shaped configuration, respectively.<sup>29</sup> The vertical lines represent center-to-center distances between vertical molecules along and across the Ti atom rows. The grey band represents the range of intermolecular distances when molecules tilt across the Ti rows over the range  $[-7^\circ, 7^\circ]$ . (b) Schematic illustration of four benzoate molecules, represented as quadrupoles with negative charge above and below phenyl rings and positive charge

surrounding the periphery, in a tetramer configuration. The Ti and O atoms are in blue and red, respectively.

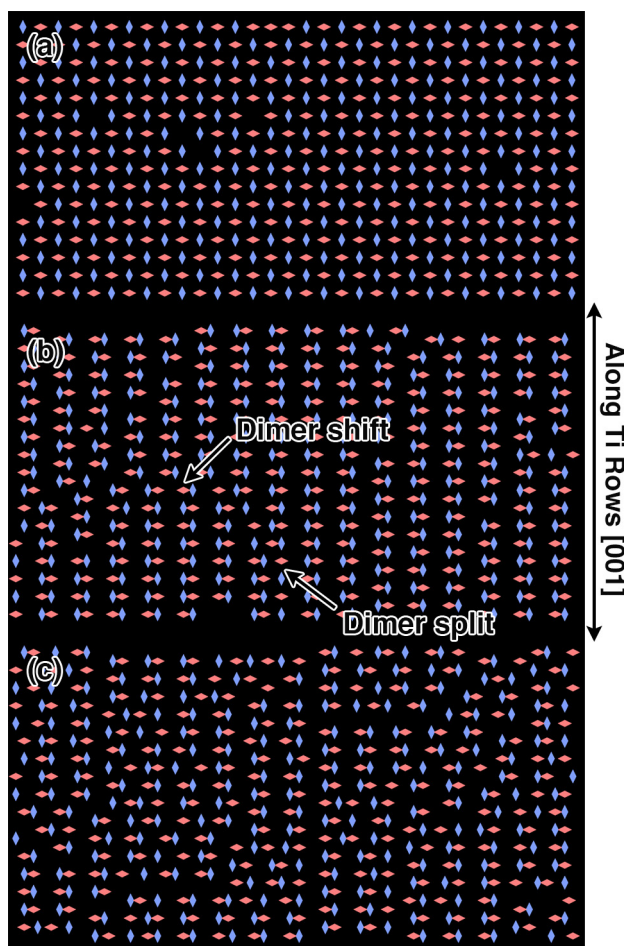


Figure 5.6 Simulated benzoate monolayers from Monte Carlo simulations. Each diamond represents one molecule with the phenyl ring along the longer axis. The different colors are used only to distinguish orientation. (a) Tetramers are formed by molecules with their nearest neighbors when tilting is not allowed. If tilting is allowed, molecules tilt across the Ti atom rows to form paired tetramers as in (b) and (c). The extent of pairing is higher at (b) low temperature than (c) higher temperature.

### 5.3.5 DFT calculations

To test the conclusions from the MC simulations, several different benzoate configurations were investigated by DFT calculations. The DFT calculations were applied to a  $4 \times 2$  supercell consisting of 5  $\text{TiO}_2$  trilayers. The surface of the supercell contained 8  $\text{Ti}_{5c}$  sites where 4 benzoate molecules could be adsorbed. The stability of these configurations was calculated and compared in Fig. 5.7. The paired tetramer configuration in which nearest benzoates tilt towards each other by  $7^\circ$  was the most stable configuration, which is in good agreement with the MC simulations. Other configurations, such as the parallel dimers, staggered parallel dimers, and T-shaped dimers, had higher energies than the paired tetramer configuration.

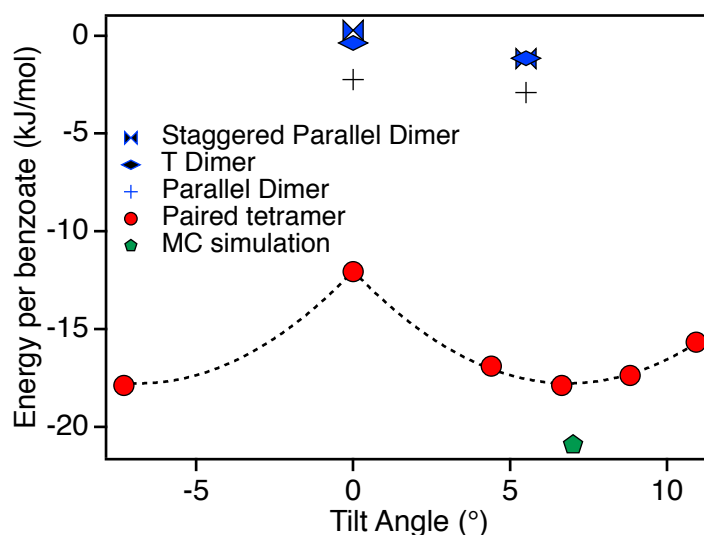


Figure 5.7 Energies of different configurations obtained from DFT calculations as a function of tilting angle. The blue symbols represent the energies of different dimer structures, and the red circles represent the energy of the paired tetramer configuration. The energy of the MC simulation is shown in green. The dotted line is a polynomial fit.

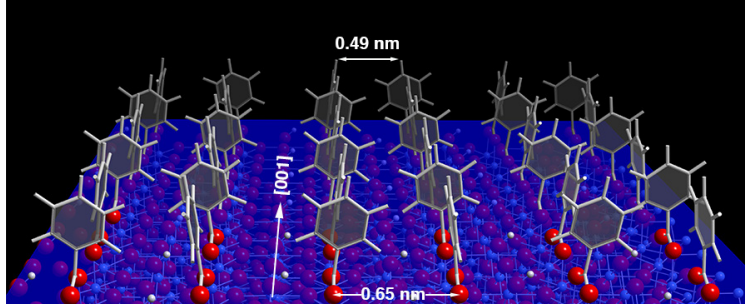


Figure 5.8 Model of the most stable configuration of benzoate monolayer on rutile (110) surface from DFT calculations. Benzoate molecules adopt an edge-to-face geometry with their four nearest neighbors to form tetramers. The benzoate molecules tilt toward each other across Ti atom rows by  $7^\circ$ . The distance between terminal H atoms is 0.49 nm, whereas the distance between Ti atoms across the rows is 0.65 nm.

The good agreement between the DFT calculations and MC simulations were surprising, considering the simplicity of the MC models and different levels of theory of the two calculations. The energy calculated by DFT for the paired tetramer configuration was -17.9 kJ/mol, whereas the energy estimated from MC simulations was -20.9 kJ/mol, a 15% difference. This small discrepancy suggested that the interactions between the adsorbed benzoates were dominated by the  $\pi$ - $\pi$  interactions between the phenyl rings.

The C-H vibrations of the benzoate monolayer were also calculated in the paired tetramer configuration using density functional perturbation theory. The transition dipole moment of the  $l$ th eigenmode,  $\vec{\mu}_l$ , was given by the Born effective charge tensor  $\vec{Z}_n^*$  and the normalized displacement of the  $n$  atoms  $\vec{d}_l$  by

$$\vec{\mu}_l = \sum_n \vec{Z}_n^* \vec{d}_{n,l}. \quad (5)$$

The total absorbance was

$$A_{total}(\omega) = \sum_l \int I(\omega - \omega_0) |\mu_l|^2 \delta(\omega_0 - \omega_l) d\omega_0 , \quad (6)$$

where  $\omega_l$  is the energy of the  $l$ th normal mode, and  $I$  is the spectral lineshape function (here, Gaussian). If incident light with an electric field  $\hat{j}$  interacts with the system, the absorbance along the direction of  $\hat{j}$  is

$$A_j(\omega) = \sum_l \int I(\omega - \omega_0) (\hat{j} \cdot \mu_l)^2 \delta(\omega_0 - \omega_l) d\omega_0 . \quad (7)$$

The calculated spectra cannot be compared directly to the experimental spectra obtained with  $p$ -polarized or unpolarized incident light,<sup>42</sup> because an unknown surface dielectric constant screens the electric field perpendicular to the surface. The  $p$ -polarized or unpolarized radiation has components in the  $z$  direction whereas  $s$ -polarized radiation is entirely in the  $x$ - $y$  plane. As a result, the  $p$ -polarized spectra cannot be estimated without the knowledge of the surface dielectric constant, whereas  $s$ -polarized spectra can be directly compared to the experimental data.

The calculated spectra of the C-H modes are compared to the experimental spectra under different polarization conditions in Fig. 5.3. The calculated vibrational frequencies are consistent with the experimental frequencies; however, there are significant differences in the polarization dependence.

#### 5.4 Discussion

High-quality benzoate monolayers could be prepared on rutile (110) surfaces from aqueous benzoic acid solutions. These self-assembled monolayers were hydrophobic. Sputtering and annealing the rutile surface, a process that produces many defects, was not necessary. The monolayers remained free of contamination during exposure to air for tens of min.

The desorption process was reversible. A brief immersion in pure water reversed the hydrophobicity, suggesting that formation of the monolayer is a dynamic process. The paired and unpaired regions did not change over hours in UHV, suggesting that monolayer annealing does not occur out of solution. The annealing of the monolayer primarily occurred through adsorption and desorption events in solutions not through benzoate diffusion on the surface.

The DFT calculations and infrared spectra suggested that the benzoate molecules in the monolayer formed tetramers with their four nearest neighbors in an edge-to-face geometry. The monolayer was stabilized by the strong Ti-O bonds and  $\pi$ - $\pi$  interactions. Benzoate molecules tilted toward one another across the Ti rows, a pairing that was interpreted as dimerization in previous research. The coexistence of both paired and unpaired regions indicated that the energy gain from tilting to form dimers was comparable to thermal energy.

Higher order multiplets, such as triplets, were sometimes observed, which is consistent with previous research. Triplets were also observed in MC simulations when a larger tilt angle was allowed. The preferred formation of pairs represents a balance between energy gain from  $\pi$ - $\pi$  interactions and energy loss from reduced Ti-O overlap.

The configuration of benzoate monolayer on rutile surfaces was similar to organic monolayers on amorphous substrates, such as SiO<sub>2</sub>. The principle difference is that the rutile lattice enforces a particular packing density of the benzoate monolayer. It is surprising that the geometry and energetics of the benzoate monolayer on rutile can be modeled using a simple MC simulation including only the surface geometry and the intermolecular interactions of small-molecule analogues of the adsorbate. This type of simple MC simulations might provide a method to predict properties of monolayers and design new monolayers on surfaces.

## 5.5 Conclusions

High-quality, self-assembled benzoate monolayers were prepared by immersion in benzoic acid solution. Sputtering and annealing of the surface was not needed. The benzoate monolayer was hydrophobic and remained free from contamination even after exposure to air for tens of min. The monolayer displayed paired regions, unpaired regions, and some defects. The benzoate molecules were stabilized by the strong Ti-O bonds and  $\pi$ - $\pi$  intermolecular interactions. The molecules adopted an edge-to-face geometry with their four nearest neighbors leading to the formation of tetramers. The monolayer was further stabilized by the tilting of molecules toward each other across the Ti atom rows, which resulted in the formation of paired tetramers interpreted as “dimers” in previous STM research. This paired tetramer configuration could be reproduced by simple Monte Carlo simulations that included the surface geometry and intermolecular interactions of small molecule analogues of the monolayer head group. This approach might provide a method to predict properties of monolayers and design new monolayers on surfaces.

## References

1. B. E. Hardin, H. J. Snaith, and M. D. McGehee, “The Renaissance of Dye-Sensitized Solar Cells,” *Nature Photonics* **6**, 162-169 (2012).
2. B. O'Regan and M. Grätzel, “A Low-Cost, High-Efficiency Solar Cell Based on Dye-Sensitized Colloidal TiO<sub>2</sub> Films,” *Nature* **353**, 737-740 (1991).
3. W. Peng, W. J. DeBenedetti, S. Kim, M. A. Hines, and Y. J. Chabal, “Lowering the Density of Electronic Defects on Organic-Functionalized Si (100) Surfaces,” *Appl. Phys. Lett.* **104**, 241601 (2014).

4. W. Peng, O. Seitz, R. Chapman, E. Vogel, and Y. Chabal, "Probing the Intrinsic Electrical Properties of Thin Organic Layers/Semiconductor Interfaces Using an Atomic-Layer-Deposited Al<sub>2</sub>O<sub>3</sub> Protective Layer," *Appl. Phys. Lett.* **101**, 051605 (2012).
5. H. J. Snaith, "Estimating the Maximum Attainable Efficiency in Dye-Sensitized Solar Cells," *Adv. Funct. Mater.* **20**, 13-19 (2010).
6. D. O. Scanlon, C. W. Dunnill, J. Buckeridge, S. A. Shevlin, A. J. Logsdail, S. M. Woodley, C. R. A. Catlow, M. J. Powell, R. G. Palgrave, and I. P. Parkin, "Band Alignment of Rutile and Anatase TiO<sub>2</sub>," *Nature Materials* **12**, 798-801 (2013).
7. F. De Angelis, S. Fantacci, E. Mosconi, M. K. Nazeeruddin, and M. Grätzel, "Absorption Spectra and Excited State Energy Levels of the N719 Dye on TiO<sub>2</sub> in Dye-Sensitized Solar Cell Models," *J. Phys. Chem. C* **115**, 8825-8831 (2011).
8. H. G. Agrell, J. Lindgren, and A. Hagfeldt, "Degradation Mechanisms in a Dye-Sensitized Solar Cell Studied by UV-Vis and IR Spectroscopy," *Solar Energy* **75**, 169-180 (2003).
9. F. Nour-Mohhamadi, S. D. Nguyen, G. Boschloo, A. Hagfeldt, and T. Lund, "Determination of the Light-Induced Degradation Rate of the Solar Cell Sensitizer N719 on TiO<sub>2</sub> Nanocrystalline Particles," *J. Phys. Chem. B* **109**, 22413-22419 (2005).
10. A. Quan, "Degradation of the Solar Cell Dye Sensitizer N719 Preliminary Building of Dye-Sensitized Solar Cell," Thesis, Denmark: Roskilde University, 2006.
11. W. M. Campbell, A. K. Burrell, D. L. Officer, and K. W. Jolley, "Porphyrins as Light Harvesters in the Dye-Sensitised TiO<sub>2</sub> Solar Cell," *Coord. Chem. Rev.* **248**, 1363-1379 (2004).
12. S. Ardo and G. J. Meyer, "Photodriven Heterogeneous Charge Transfer with Transition-Metal Compounds Anchored to TiO<sub>2</sub> Semiconductor Surfaces," *Chem. Soc. Rev.* **38**, 115-164 (2009).

13. P. Qu and G. J. Meyer, "Proton-Controlled Electron Injection from Molecular Excited States to the Empty States in Nanocrystalline TiO<sub>2</sub>," *Langmuir* **17**, 6720-6728 (2001).
14. D. C. Grinter, P. Nickels, T. Woolcot, S. N. Basahel, A. Y. Obaid, A. A. Al-Ghamdi, E.-S. H. El-Mossalamy, A. O. Alyoubi, and G. Thornton, "Binding of a Benzoate Dye-Molecule Analogue to Rutile Titanium Dioxide Surfaces," *J. Phys. Chem. C* **116**, 1020-1026 (2011).
15. Q. Guo, I. Cocks, and E. Williams, "The Adsorption of Benzoic Acid on a TiO<sub>2</sub> (110) Surface Studied Using STM, ESDIAD and LEED," *Surf. Sci.* **393**, 1-11 (1997).
16. U. Diebold, "The Surface Science of Titanium Dioxide," *Surf. Sci. Rep.* **48**, 53-229 (2003).
17. D. C. Grinter, T. Woolcot, C.-L. Pang, and G. Thornton, "Ordered Carboxylates on TiO<sub>2</sub>(110) Formed at Aqueous Interfaces," *J. Phys. Chem. Lett.* **5**, 4265-4269 (2014).
18. E. C. Landis, S. C. Jensen, K. R. Phillips, and C. M. Friend, "Photostability and Thermal Decomposition of Benzoic Acid on TiO<sub>2</sub>," *J. Phys. Chem. C* **116**, 21508-21513 (2012).
19. X. Zhao and D. R. Bowler, "DFT Studies of Adsorption of Benzoic Acid on the Rutile (110) Surface: Modes and Patterns," *arXiv preprint arXiv:1407.1659* (2014).
20. S. C. Mannsfeld, A. Virkar, C. Reese, M. F. Toney, and Z. Bao, "Precise Structure of Pentacene Monolayers on Amorphous Silicon Oxide and Relation to Charge Transport," *Adv. Mater.* **21**, 2294-2298 (2009).
21. A. Song, D. Jing, and M. A. Hines, "Rutile Surface Reactivity Provides Insight into the Structure-Directing Role of Peroxide in TiO<sub>2</sub> Polymorph Control," *J. Phys. Chem. C* **118**, 27343-27352 (2014).
22. A. Song, E. S. Skibinski, W. J. DeBenedetti, A. G. Ortoll-Bloch, and M. A. Hines, "Nanoscale Solvation Leads to Spontaneous Formation of a Bicarbonate Monolayer on Rutile

- (110) under Ambient Conditions: Implications for CO<sub>2</sub> Photoreduction,” *J. Phys. Chem. C* **120**, 9326 (2016).
23. U. Diebold and T. Madey, “TiO<sub>2</sub> by XPS,” *Surf. Sci. Spectra* **4**, 227-231 (1996).
24. M. B. Hugenschmidt, L. Gamble, and C. T. Campbell, “The Interaction of H<sub>2</sub>O with a TiO<sub>2</sub> (110) Surface,” *Surf. Sci.* **302**, 329-340 (1994).
25. C. Wagner, L. Davis, M. Zeller, J. Taylor, R. Raymond, and L. Gale, “Empirical Atomic Sensitivity Factors for Quantitative Analysis by Electron Spectroscopy for Chemical Analysis,” *Surf. Interface Anal.* **3**, 211-225 (1981).
26. G. Fuentes, E. Elizalde, F. Yubero, and J. Sanz, “Electron Inelastic Mean Free Path for Ti, TiC, TiN and TiO<sub>2</sub> as Determined by Quantitative Reflection Electron Energy-Loss Spectroscopy,” *Surf. Interface Anal.* **33**, 230-237 (2002).
27. N. Metropolis, A. W. Rosenbluth, M. N. Rosenbluth, A. H. Teller, and E. Teller, “Equation of State Calculations by Fast Computing Machines,” *J. Chem. Phys.* **21**, 1087-1092 (1953).
28. W. L. Jorgensen, Perspective on “Equation of State Calculations by Fast Computing Machines”. In *Theor. Chem. Acc.*, Springer: 2000; pp 225-227.
29. I. Cacelli, G. Cinacchi, G. Prampolini, and A. Tani, “Modeling Benzene with Single-Site Potentials from *Ab Initio* Calculations: A Step toward Hybrid Models of Complex Molecules,” *J. Chem. Phys.* **120**, 3648-3656 (2004).
30. W. Kohn and L. J. Sham, “Self-Consistent Equations Including Exchange and Correlation Effects,” *Phys. Rev.* **140**, A1133 (1965).
31. G. Kresse and J. Hafner, “*Ab Initio* Molecular Dynamics for Liquid Metals,” *Phys. Rev. B* **47**, 558 (1993).

32. G. Kresse and J. Hafner, “*Ab Initio* Molecular-Dynamics Simulation of the Liquid-Metal–Amorphous-Semiconductor Transition in Germanium,” *Phys. Rev. B* **49**, 14251 (1994).
33. G. Kresse and J. Furthmüller, “Efficiency of *Ab-Initio* Total Energy Calculations for Metals and Semiconductors Using a Plane-Wave Basis Set,” *Comput. Mat. Sci.* **6**, 15-50 (1996).
34. G. Kresse and J. Furthmüller, “Efficient Iterative Schemes for *Ab Initio* Total-Energy Calculations Using a Plane-Wave Basis Set,” *Phys. Rev. B* **54**, 11169 (1996).
35. S. Grimme J. Antony, S. Ehrlich, and H. Krieg, “A Consistent and Accurate *Ab Initio* Parametrization of Density Functional Dispersion Correction (DFT-D) for the 94 Elements H–Pu,” *J. Chem. Phys.* **132**, 154104 (2010).
36. P. E. Blöchl, “Projector Augmented-Wave Method,” *Phys. Rev. B* **50**, 17953 (1994).
37. G. Kresse and D. Joubert, “From Ultrasoft Pseudopotentials to the Projector Augmented-Wave Method,” *Phys. Rev. B* **59**, 1758 (1999).
38. P. M. Kowalski, B. Meyer, and D. Marx, “Composition, Structure, and Stability of the Rutile TiO<sub>2</sub> (110) Surface: Oxygen Depletion, Hydroxylation, Hydrogen Migration, and Water Adsorption,” *Phys. Rev. B* **79**, 115410 (2009).
39. M. F. Camellone, P. M. Kowalski, and D. Marx, “Ideal, Defective, and Gold-Promoted Rutile TiO<sub>2</sub> (110) Surfaces Interacting with CO, H<sub>2</sub>, and H<sub>2</sub>O: Structures, Energies, Thermodynamics, and Dynamics from PBE+*U*,” *Phys. Rev. B* **84**, 035413 (2011).
40. C. R. Martinez and B. L. Iverson, “Rethinking the Term “Pi-Stacking”,” *Chem. Sci.* **3**, 2191-2201 (2012).
41. S. Grimme, “Do Special Noncovalent  $\pi$ - $\pi$  Stacking Interactions Really Exist?,” *Angew. Chem. Int. Ed.* **47**, 3430-3434 (2008).

42. J. Flidr, Y.-C. Huang, T. A. Newton, and M. A. Hines, "Extracting Site-Specific Reaction Rates from Steady State Surface Morphologies: Kinetic Monte Carlo Simulations of Aqueous Si (111) Etching," *J. Chem. Phys.* **108**, 5542-5553 (1998).